United Technologies Research Center
Report No. 87-41

NASA-CR-182286

LASER VELOCIMETER AND TOTAL PRESSURE MEASUREMENTS IN CIRCULAR-TO-RECTANGULAR TRANSITION DUCTS

William P. Patrick and Duane C. McCormick

June 1988

Final Report
Contract NAS3-24616

Prepared for
NASA Lewis Research Center
2100 Brookpark Road
Cleveland, OH 44135

(NASA-CR-182286) LASER VELOCIMETER AND TOTAL PRESSURE MEASUREMENTS IN CIRCULAR-TO-RECTANGULAR TRANSITION DUCTS Final Report (United Technologies Research Center) 121 p CSCL 20D G3/34

N90-14494

Unclas
0234607

UNITED TECHNOLOGIES RESEARCH CENTER
East Hartford, Connecticut 06108

UTRC87-41

Laser Velocimeter and Total Pressure Measurements in Circular-to-Rectangular Transition Ducts

REPORTED BY William P. Patrick
William P. Patrick

Duane C. McCormick
Duane C. McCormick

APPROVED BY Robert W. Paterson
Robert W. Paterson

DATE June 1988

NO. OF PAGES 130

COPY NO. ____________

Laser Velocimeter and Total Pressure Measurements in Circular-to-Rectangular Transition Ducts

TABLE OF CONTENTS

TABLE OF CONTENTS (Cont'd)

LIST OF FIGURES

LIST OF FIGURES (Cont'd)

LIST OF FIGURES (Cont'd)

LIST OF TABLES

NOMENCLATURE

AR	Aspect ratio
C_f	Skin friction coefficient
D	Inlet diameter
H	Half height of exit plane or boundary layer shape factor, δ^*/θ
L	Axial length
P	Total pressure
p	Static pressure
Q	Dynamic head
q	Turbulent kinetic energy
R	Inlet radius
Re_θ	Reynolds number based on momentum thickness
rady	Superellipse coefficient
radz	Superellipse coefficient
S	Half-span of exit plane
T	Static temperature
U	Axial mean velocity component
U^+	Non-dimensional axial velocity component, U/U_τ
U_τ	Friction velocity
u	Axial fluctuating component
V	Spanwise mean velocity component
v	Spanwise fluctuating velocity component
W	Transverse mean velocity component
w	Transverse fluctuating velocity component
x	Axial coordinate
y	Spanwise coordinate
y_{bl}	Boundary layer wall distance
y+	Non-dimensional boundary layer wall distance, $y_{bl}U_\tau/\nu$
z	Transverse coordinate
δ_{995}	Boundary layer thickness at 0.995 U_{ref}
δ^*	Boundary layer displacement thickness
η_y	Superellipse exponent
η_z	Superellipse exponent
θ	Boundary layer momentum thickness
ν	Kinematic viscosity
Ω_x	Axial vorticity component

Subscript

ref	Quantity measured at reference location
i	Inviscid velocity
iw	Inviscid velocity at the wall

PRECEDING PAGE BLANK NOT FILMED

ORIGINAL PAGE IS
OF POOR QUALITY

SUMMARY

Laser Velocimeter and Total Pressure Measurements in Circular-to-Rectangular Transition Ducts

William P. Patrick and Duane C. McCormick

A comprehensive set of total pressure and three-component laser velocimetry (LV) data has been obtained within two circular-to-rectangular transition ducts at low subsonic speeds. This set of reference data was acquired for use in identifying secondary flow mechanisms and for assessing the accuracy of computational procedures for calculating such flows. Data were obtained at the inlet and exit planes of an aspect ratio three duct having a length-to-diameter ratio of one (AR310) and an aspect ratio six duct having a length-to-diameter ratio of three (AR630). Each duct was unseparated throughout its transition section. Total pressure distributions showed the flows to be symmetric in each duct. Axial velocity distributions in the exit plane were much flatter in the AR630 duct than the AR310 duct indicating that the flow had not completely expanded to fill the exit duct uniformly in the shorter AR310 duct prior to reaching the exit plane. The continuing expansion of the flow into the exit duct caused small outward cross flows in the exit plane of each duct. Maximum cross-flow velocities were 0.12 U_{ref} for the AR310 duct and 0.11 U_{ref} for the AR630 duct.

The flow distributions differed significantly near the sidewalls of each duct. The sidewall boundary layers in the AR310 duct were relatively thin whereas the AR630 duct sidewall boundary layers were thickened by an axial vortex pair which transported low momentum fluid from the sidewalls into the core flow along the duct semi-major axis. The fluid dynamics which created the sidewall vortex pair in the high aspect ratio AR630 duct can be understood by first considering the flow in a circular S-duct. The secondary flow pattern that exists in an S-duct is initiated in the first bend where the higher velocity flow in the core flow moves away from the inner wall due to centrifugal force. The resulting pressure field creates a recirculation pattern composed of two counterrotating vortices. In the second bend of the S-duct, the pressure forces are reversed and the strength of the vortex pair is diminished. In the AR630 transition duct the stream tube near the sidewall of the transition duct approximates the shape of an S-duct. However, the transition duct shape becomes nearly rectangular between the first and second bends in the sidewall causing the vortex pair to be concentrated and strengthened. Further assisting the strengthening of the vortex pair is the natural tendency of a flow in a straight rectangular duct to form corner vortices. Flow in the lower aspect ratio AR310 duct does not have the same contribution from vortex concentration and rectangular duct corner vortex development, and, therefore, has weak corner vortices in the exit plane.

It is therefore concluded that secondary flows can play an important part in the fluid dynamics of transition ducts and needs to be addressed in computational analysis. The strength of the secondary flows depends on both the aspect ratio and relative axial duct length.

CHAPTER 1

INTRODUCTION

Advanced jet engine exhaust systems for military aircraft employ nonaxisymmetric nozzles for supermanueverability and/or thermal plume reduction. These nonaxisymmetric nozzles are usually rectangular in cross section to achieve mission requirements such as thrust vectoring and nozzle area ratio variability within fabrication, material, and cost constraints. For certain applications rectangular nozzles having aspect ratios greater than five have been proposed.

The transition duct which connects the axisymmetric jet engine to the rectangular convergent-divergent nozzle should be designed to deliver uniform subsonic flow with minimal losses to the nozzle. The practical need to minimize the weight of the propulsion system requires that the transition to high aspect ratio occur in the shortest possible distance. This constraint, however, increases the probability of flow separation within the transition duct with the associated penalties of high viscous losses and severe cooling problems (Ref. 1).

Computer codes for calculating three-dimensional viscous flows have been developed which offer the possibility of designing short, high aspect ratio transition ducts having low loss. Critical to the implementation of such codes in engine design systems, however, is the availability of data for assessing code accuracy. Total pressure and three-component velocity measurements in the inlet and exit planes of high aspect ratio transition ducts have not been previously reported. The objective of the current program is to provide such reference data of benchmark quality for two transition duct geometries to provide needed data for code assessment and an understanding of the flow physics.

The two ducts tested were of the most basic design having no net diffusion, turning, or inlet swirl. The first duct, supplied by NASA, had an aspect ratio of three (3) and a length-to-inlet diameter ratio of unity (1.0) and was designated AR310. The second duct, supplied by UTC, had an aspect ratio of six (6) and a length-to-inlet diameter ratio of three (3.0) and was designated AR630. Each transition duct was constructed from superelliptic cross-sections positioned perpendicular to the duct centerline to match the geometric input requirements of PEPSIG, the three-dimensional subsonic viscous marching code which has been developed under NASA-Lewis Research Center sponsorship (Ref. 2). In Figure 1-1, prepared by the Lewis-Research Center's Computational Methods Branch (Ref. 3), the stall boundaries for constant area and accelerating transition ducts have been calculated as a function of L/D and aspect ratio using PEPSIG. The calculations were performed for ducts having extremely thin inlet boundary layers. The ducts in the current study were chosen because of their proximity to the stall boundary.

PRECEDING PAGE BLANK NOT FILMED

The study of the AR310 transition duct was sponsored by NASA Lewis Research Center. Data for the AR630 transition duct were acquired under the UTRC independent research program in gas dynamics. The authors wish to acknowledge helpful discussions with the NASA Lewis technical monitor Mr. A. R. Bishop as well as Mr. Bernard Anderson (NASA Lewis), Dr. Robert Paterson (UTRC), and Dr. Michael Werle (UTRC). Appreciation is also expressed to Mr. Charles Coffin (UTRC) for his high quality work both in performing the LV and total pressure measurements and in fabricating the constant area duct extension sections.

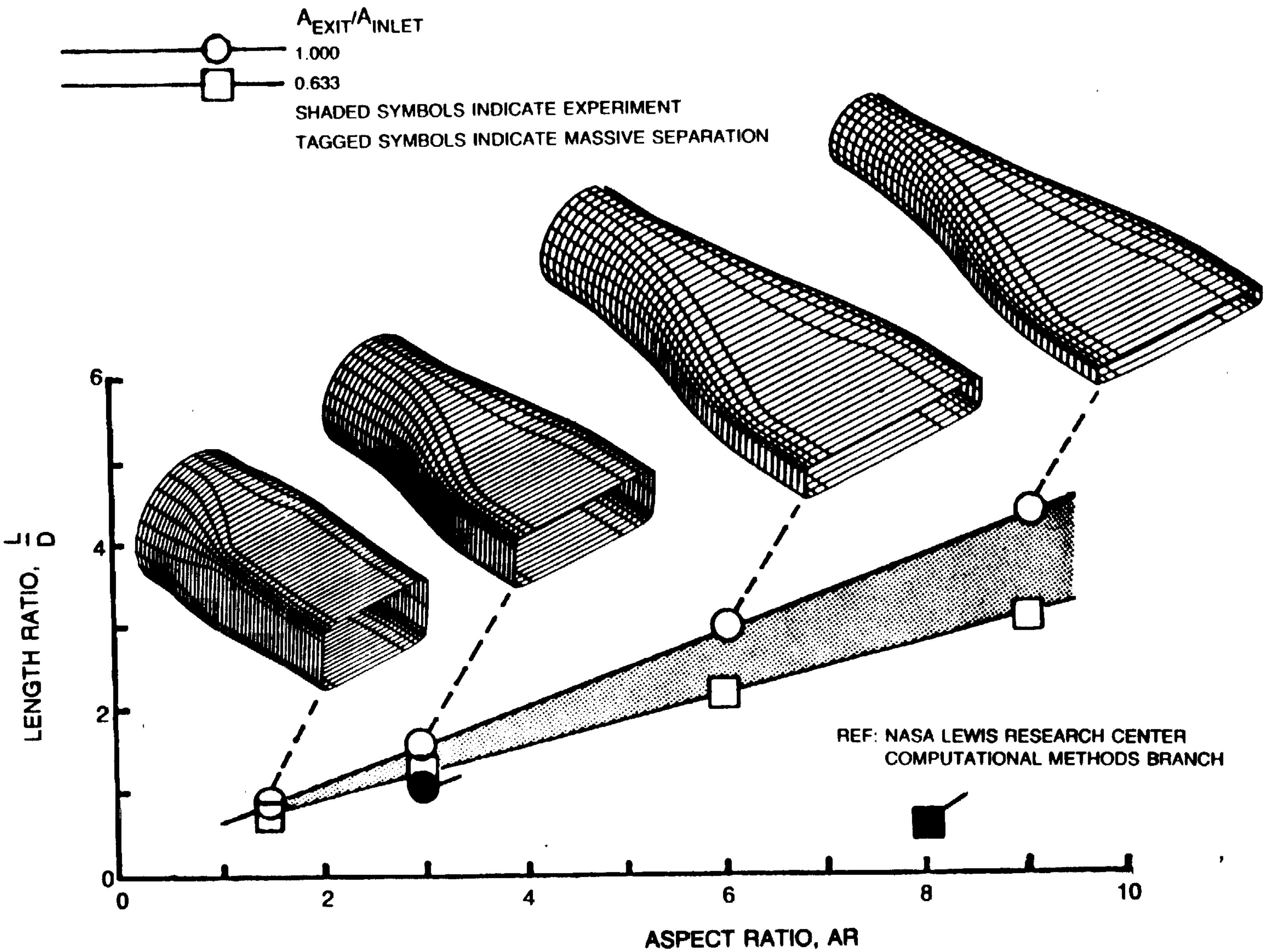

Figure 1.1. — Calculated Stall Margin for Benchmark Transition Duct Configurations

87-9-19-1

CHAPTER 2

REVIEW OF PREVIOUS INVESTIGATIONS

Although benchmark quality flowfield data for high-aspect-ratio transition ducts has not been reported previously, several related studies have been performed since the initial transition duct flowfield documentation by Mayer (Ref. 4) fifty years ago. The current program is the latest in a series of programs sponsored by the NASA Lewis Research Center to obtain benchmark quality experimental data sets for generic aircraft inlet and exhaust duct configurations for the purpose of verifying three-dimensional viscous codes. The overall program, which was reviewed in 1984 by Anderson (Ref. 2), included a series of studies having increasing flow complexity which were performed at Imperial College of Science and Technology in London. These tests which included flows in 90-degree bends having square (Ref. 5) and circular (Ref. 6) cross sections, circular (Ref. 7) and square (Ref. 8) S-ducts, and a square-to-round transition duct (Ref. 9) were documented using total pressure traverses, sidewall static pressures, and three-component LV measurements. Recent additional programs in the NASA Lewis sponsored series have been conducted at the University of Tennessee Space Institute by Vakili et al (Ref. 10) to study the structure of compressible secondary flows in an S-duct and by Crawford et al. (Ref. 11) to obtain benchmark quality LV measurements in a 90-degree turning duct having a square cross section with thin turbulent inlet boundary layers. In addition to the NASA-Lewis sponsored programs, studies by Melling and Whitelaw (Ref. 12), Rowe (Ref. 13), and Bansod and Bradshaw (Ref. 14) provide insight into the generation of secondary flows in straight rectangular ducts, curved ducts, and S-shaped ducts, respectively.

Few transition duct studies have been performed either analytically or experimentally. Mayer (Ref. 4) performed detailed measurements with a four-hole-probe, a pitot probe, and wall static pressure taps to obtain total pressure contours and the three-dimensional velocity field in two constant area ducts which transitioned from circular (D = 190 mm) to rectangular with an aspect ratio of 2.0 (238 mm x 119 mm) in 0.58 and 2.32 inlet diameters. The cast aluminum alloy transition sections had no surface discontinuities in the mean flow direction although the cross-sectional shapes were discontinuous in the circumferential direction throughout the transition (as shown in Fig. 2-1).

Both circular-to-rectangular and rectangular-to-circular transition flows were tested at a Reynolds number based on inlet hydraulic diameter of 192,000. The flow throughout the test section was unseparated in each test. For each case the inlet velocity profile was fully developed and turbulent. The cross-stream velocities for the circular-to-rectangular tests showed maxima of 22 percent and 10 percent of the maximum streamwise velocity for the short and long transition

PRECEDING PAGE BLANK NOT FILMED

section, respectively. Secondary flows at the exit of the rectangular-to-circular transitions were much less. Mayer noted that for the rectangular-to-circular test cases the inlet flowfield contained significant secondary flows, shown qualitatively in Fig. 2-2. These secondary flows typically develop in the corners of rectangular ducts due to Reynolds stress gradients in the inlet boundary layers (Ref. 9). This flow feature of non-circular, straight ducts has been observed as long ago as 1926 by Prandtl (Ref. 15) from which Fig. 2-2 was taken. For Mayer's rectangular-to-circular case, the inlet secondary flows were attenuated in the transition section.

Taylor et al. (Ref. 9) measured the flow through a duct which transitioned from a 40 mm square cross section to a 40 mm diameter circular cross section in 80 mm with a resultant decrease in cross-sectional area of 21.5 percent. Each cross section in the transition was formed by the intersection of a square and a circle, and approximated a superellipse with a shape factor of unity to within 1.5 percent of the radius. Tests were conducted with water at a Reynolds number based on inlet hydraulic diameter of 35,350. The inlet boundary layer thickness, defined at 95 percent of the maximum velocity, was 13 percent of the inlet hydraulic diameter. Secondary flows in the square inlet section were estimated to be less than 1.5 percent of the bulk velocity because of the thin inlet boundary layers.

LV measurements of mean velocity components, turbulence levels, and shear stress were obtained. Maximum cross-stream velocities of 7 percent of the bulk velocity were measured at the exit plane. Taylor et al. attributed the development of the secondary flows to lateral pressure gradients which originated due to differences in streamwise wall curvature in the corner fillets compared to the symmetry planes oriented 45 degrees to the bisector of the corner fillets. Higher pressures in the fillets relative to the region of the symmetry plane induced the cross-stream flows.

Recently tests were performed at the NASA Langley Research Center by Burley, Bangert, and Carlson (Ref. 1) to determine the overall performance of a high-aspect-ratio nonaxisymmetric nozzle and circular-to-rectangular transition ducts. Five transition ducts were used to study the effects of duct length, wall shape, and cross-sectional area distribution on performance. Ducts having transition lengths equal to 0.5, 0.75, and 1.0 times the 200 mm inlet diameter were tested. Each duct had an exit plane aspect ratio of 6.33. The duct cross sections were developed from superelliptic shapes to provide smooth transition from the circular inlet to the rectangular exhaust. Nevertheless, for the duct lengths of 0.75 inlet diameters or less, large regions of separated flow were observed in the transition sections for ducts having constant cross-sectional areas. Decreasing the cross-sectional area through the transition reduced the extent of flow separation.

Fluid dynamic measurements were limited to wall static pressure measurements, total-pressure profiles in the inlet and exit planes, and surface flow visualization. Inlet and exit total-pressure profiles were integrated to determine total pressure loss through the ducts. Overall performance of the slot nozzle determined from the discharge coefficient and thrust ratio decreased when the transition duct length was reduced from 1.0 to 0.5 inlet diameters.

Gutmark and Schadow (Refs. 16 and 17) have studied the effect of secondary flows generated in the conical contraction to a slot jet fuel nozzle on the enhacement of fuel-air mixing in the combustor. Air tests were conducted on three nozzles constructed from 15 deg half-angle cones tapering to elliptical slot exits with aspect ratios of 2, 3, and 5. In addition, two nozzles having 7.5 deg and 30 deg contractions to an aspect ratio 3 exit were tested to study the effect of nozzle length on performance. Hot-wire measurements were taken to determine mean velocity contours and the distribution of turbulence intensity in the flow exiting the nozzles. Tests were conducted at a Reynolds number of 1.6×10^6 based on exit equivalent diameter and jet exit velocity. Jet spreading measurements indicated that increasing the slot aspect ratio and/or reducing the nozzle length (i.e. steepen the contraction in the conical transition) increased the axial vorticity in the jet exhaust.

Analytical studies of transition duct flows have been performed by Roberts and Forester (Ref. 18), Anderson, Muramoto, and Levy (Ref. 19), Towne and Schum (Ref. 20), and Burley, Bangert, and Carlson (Ref. 1). Roberts and Forester used a transformed set of parabolized Navier-Stokes equations to solve three-dimensional compressible viscous flows in ducts with arbitrary cross sections. One set of results pertinent to transition duct studies was presented. Turbulent flow through a duct which transitioned in two inlet diameters from a semi-circular inlet to a semi-elliptical exit with an aspect ratio of 4 was presented. Maximum cross-stream velocities equal to 20 percent of the streamwise velocity in the duct exit plane were predicted.

Burley et al. used the potential flow code MCAERO to predict the sidewall static pressure distributions measured in the transition duct tests described previously. Agreement with experimental data was poor because of the highly viscous nature of the flow in the ducts.

Towne and Schum used PEPSIG to compute flowfields in curved aircraft inlet configurations which included rectangular-to-circular cross sections. Calculations were performed for turbulent flow at a Reynolds number based on diameter of 48,000 and an inlet Mach number of 0.5. Their study included variations in inlet boundary layer thickness and Mach number. Calculations for flows having inlet boundary layer thickness of 0.048 and 0.24 of the inlet duct half width indicated the basic flow phenomena to be the same for each case but the thicker boundary layer persisted through the transition section causing lower total pressure recovery at the engine face. Calculations for Mach numbers of 0.5 and 0.01 showed minor differences in the flowfields. In addition, calculations of the flowfield in a straight section which transitioned from a rectangular inlet with an aspect of ratio of 2 to a circular duct over a distance of 4 exit duct diameters showed no significant distortion in the flowfield in the elongated transition section.

Anderson, Muramoto, and Levy used PEPSIG to calculate flowfields in circular-to-rectangular transition ducts having short duct lengths and high aspect ratios. Duct cross sections were defined by constant area superellipses. Computations were performed for flows at high Reynolds number (7.3×10^5/m), with very thin inlet boundary layers, at an inlet Mach number of 0.3. Results presented for an aspect ratio 3 duct having a length of 1.5 inlet diameters (i.e. AR315) revealed a three-dimensional separation midway through the transition section followed by the generation of a strong pair of axial vorticies. Following subsequent reattachment of the flow, the vortex pair persisted to the duct exit inducing cross-stream velocities in excess of 10 percent of the exit freestream velocity.

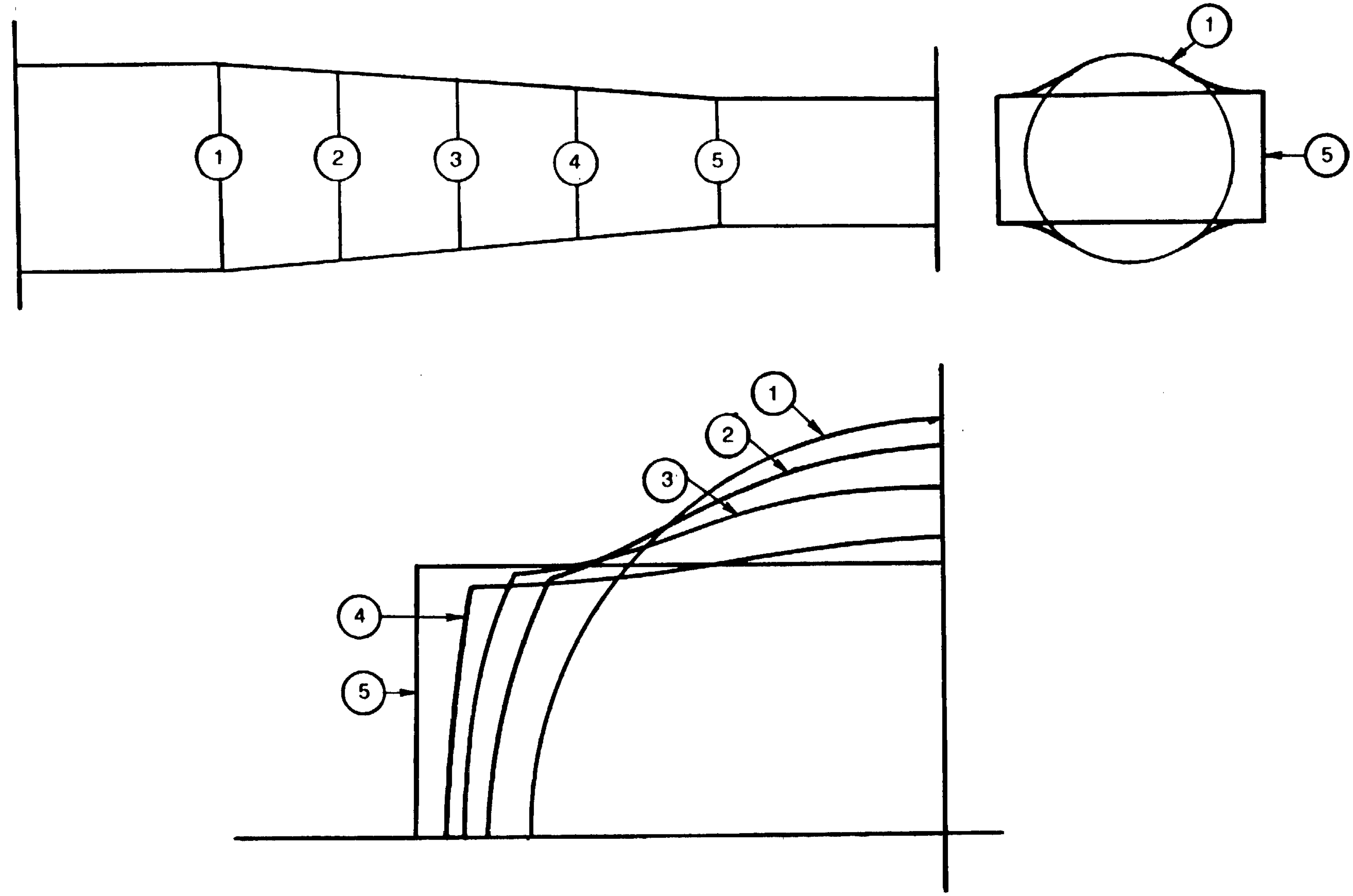

87—9—19—74

Figure 2-1. — Schematic of Transition Duct (L/D = 2.3) Investigated by Mayer (Ref. 4)

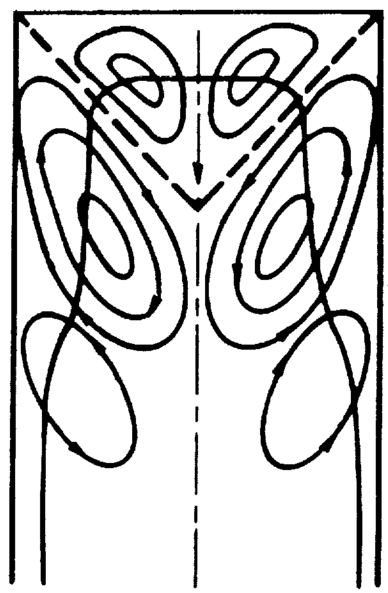

Figure 2-2. — Secondary Flows In a Rectangular Duct (From Reference 15)

CHAPTER 3

DESCRIPTION OF THE EXPERIMENT

3.1 Experimental Arrangement

3.1.1 Transition Duct Definition

The two circular-to-rectangular transition ducts tested are shown in Fig. 3-1. The coordinate system origin is located at the circular inlet with the x axis in the axial direction, the y axis in the spanwise direction, and the z axis in the transverse direction. The characteristic duct dimensions (L, D, S, and H) are also shown in the figure. The aspect ratio, defined as AR = S/H, characterizes the narrowness of the rectangular exit. The axial duct length is characterized by the axial-length-to-inlet-diameter ratio, L/D. The value of these two parameters are combined to form the duct designation. For example, in part a) of the figure the transition duct is designated AR310 which illustrates an aspect ratio 3 exit with an overall length of L/D = 1.0. The second duct, show in part b) of the figure, is designated AR630 and thus has a aspect ratio 6 exit plane and an L/D of 3.0.

The cross sections of the transition ducts are composed of a series of superelliptical shapes perpendicular to the duct centerline. The superelliptical shapes are defined by the equation

$$\left(\frac{y}{rady}\right)^{\eta_y} + \left(\frac{z}{radz}\right)^{\eta_z} = 1 \qquad (1\text{-}1)$$

where the coefficients rady, radz, η_y, and η_z are a function the axial position. The coefficients versus axial distance for the two ducts are listed in Table I at each 4 percent of the transition duct length. Note, the axial distance (x), rady, and radz have been normalized by the inlet radius. Since the cross sections of the ducts are super ellipses, the exit is shaped like a rectangle with rounded corners rather than a true rectangle.

The calculation of the superellipse coefficients is determined by prescribing the inlet and exit duct walls to be tangent to the axial direction and prescribing the cross-sectional area variation. For the AR310 transition duct, the cross-sectional area is a constant value, equal to the inlet area. For the AR630 transition duct, the area increases from the inlet value to a value 10 percent larger before contracting back down to the initial value (see Table I). This area variation corresponds to that of a transition duct constructed of flat planes and conical sections. Construction by flat planes and conical sections is typical of manufacturing techniques and thus this duct simulates the corresponding area distribution. However, the cross-sectional shapes are super-ellipses (like the AR310) in order to match the geometric input requirements of PEPSIG.

The dimensional values of the half-height, H, and half-span, S, for the AR630 transition duct were 2.778 cm and 16.665 cm, respectively. These values were calculated from Eq. (1-1) applied at the exit plane and were found to agree within 1.5 percent of the actual measured values. For the AR310 transition duct H and S were 5.776 cm and 16.768 cm, respectively. These values are from actual measurements since the half-span was found to differ significantly from the calculated value (17.184).

Because of the above noted discrepancy, a detailed inspection of the AR310 transition duct was conducted at several axial cross planes. The results showed significant differences between the actual cross-sectional shapes and those calculated by Eq. (1-1). These results are presented in Appendix A. The AR630 transition was also inspected at two axial cross planes. The results showed good agreement with Eq. (1-1). In conclusion, Eq. (1-1) should be used to describe the AR630 transition duct and Appendix A tabular data should be used to describe the AR310 duct.

3.1.2 Description of the Test Facility

A schematic of the test centerline illustrating the flow conditioning for the transition ducts is shown in Fig. 3-2. Regulated, dry air is introduced through a 15 cm diameter pipe with a perforated plate exit into the 30 cm diameter centerline/plenum. The resulting jet flow dump is allowed to spread naturally for 3.5 diameters before encountering a series of perforated plates, honeycomb, and screens used to provide a uniform, low turbulence, non-swirling flow. The flow is then accelerated with a conical contraction (for AR630, two conical contractions, see figure) to the inlet transition duct inlet diameter. The boundary layer is tripped in this contraction in order to avoid three-dimensional transition.

A constant diameter section is located between the contraction exit and the transition duct inlet. This section allows boundary layer growth under near-zero pressure gradient conditions, thus providing a near-equilibrium turbulent boundary layer for the transition duct inlet. This section also yields appropriate reference conditions for normalizing the velocity and pressure data.

Downstream of the transition duct the flow enters a constant area extension duct having the same cross-sectional shape as the transition duct exit. For the AR310 transition duct, the superelliptical exit plane has small corner radii and is very nearly rectangular shaped. For this reason it was unnecessary to match the exact exit plane cross section with the extension duct. Instead, the extension duct has a rectangular cross section. For the AR630, the deviation of the exit plane cross section from a rectangular shape is significant and had to be matched by the extension duct cross section. Downstream from the extension duct the flow is dumped into the test cell.

The purpose to the constant area extension duct is to provide a "test section" where the transition duct exit flow characteristics can be measured. It would be inappropriate to allow the transition duct flow to dump directly into the test cell and to attempt to document the exit flow characteristics since the resulting constant static pressure boundary condition would influence the flow even upstream of the exit plane. As show in Fig. 3-2, the exit measurement plane is 0.34 exit duct heights (4.0 cm) downstream from the exit plane for the AR310 transition duct and 0.90 exit duct heights (5.0 cm) downstream for the AR630 transition duct. It was impossible to document the flowfield at the exit plane due to optical access requirements of the LV (laser velocimetry) system.

A schematic illustrating the inlet condition definition is shown in Fig. 3-3 for the two transition ducts. To document the inlet flow conditions (flow uniformity, turbulence, zero swirl, and inlet boundary layers) the transition ducts were removed and the flow was allowed to dump into the test cell downstream of the constant diameter inlet duct (as shown in the figure). This approach was selected since PEPSIG flow calculations showed transition ducts induce flow swirl upstream of the inlet and because the desire here was to certify that the inlet flow was uniform, low turbulence, and swirl free.

For the AR310 transition duct inlet, the flow uniformity was checked with a keilhead total pressure probe just downstream of the flow dump (see Fig. 3-3a). Surveys were taken along the radial direction, r, at four angular orientations, θ. Corresponding LV surveys were taken somewhat further downstream from the exit. Mean and fluctuating velocity components in the axial, x, and transverse, z, direction were measured to check the flow swirl, turbulence level, and flow uniformity. Upstream of the flow dump the inlet boundary layer was measured with a total pressure boundary layer probe. The probe is a flattened hypodermic tube which hooks in the upstream direction to minimize the flow disturbance. The probe dimensions are 0.305 mm height and 1 mm width (height is roughly 2 percent of the measured boundary layer).

The inlet definition schematic for the AR630 transition duct is shown in Fig. 3-3b. LV surveys downstream from the flow dump were taken in the same manner as AR310. No corresponding keilhead total pressure probe surveys were taken due to the confidence gained from the AR310 surveys and the redundancy of the axial LV data. The boundary layer was measured with a total pressure boundary layer probe in the same manner as AR310. An additional angular location was taken and the surveys were taken across the entire duct diameter in order to provide total pressure uniformity documentation (since keilhead surveys were not done).

Figure 3-3 illustrates the details of the flow contraction and boundary layer trip. Note that the interfaces between the straight and conical sections were smoothed (not reflected in figure) to avoid inlet separations. The location of the boundary layer trip was chosen to be upstream of the onset of natural three-dimensional transition. A trip location was selected based on a value of $Re_x = 9 \times 10^4$ since this Reynolds number defines the approximate location where flat plate laminar boundary layer instabilities begin to amplify. The trip is of the Hama type (Ref. 21) which is a line of triangular shapes in order to provide an efficient, rapid trip. The trip thickness is .51 mm, roughly 60 percent of the estimated boundary layer displacement thickness.

Also show in Fig. 3-3 is the location of the measured reference pressures used to set the operating condition and to normalize the data. As shown, the reference (inlet) static pressure is measured upstream of the constant diameter section exit (transition duct inlet) with a wall tap. The reference total pressure is measured further upstream in the conical section with a keilhead probe where the dynamic head and thus probe wake is smaller. Together these pressures were combined to calculate the reference (inlet) dynamic head and velocity (total temperature probe upstream of the centerline flow conditioning was also measured in order to calculated velocity).

Photographs of the two transition ducts with their extension ducts installed are shown in Figs. 3-4 and 3-5. The AR310 transition duct (Fig. 3-4) was constructed in two symmetric halves (cut along the xy plane), each half being molded Plexiglas. The assembled transition duct is flange mounted. The extension duct is constructed with optical-quality glass for LV access. The AR630 transition duct (Fig. 3-5) was fabricated in a different manner than the AR310. The duct was constructed in one section using a molded fiberglass. The extension duct was fabricated in the same manner with a glass window for LV access.

3.2 Instrumentation

3.2.1 Laser Velocimeter System

The LV (Laser Velocimetry) is the primary measurement technique used in this study. This method was desirable since it measures in a nonintrusive manner the three components of velocity. The LV system used was essentially a TSI (Thermal Systems Inc.) System 9100-6 and is shown schematically in Fig. 3-6. It is a single component system which consists of a 2W argon-ion laser, backscatter optical system, counter-type signal processor, and computer for on-line data reduction, and a hard disk storage device for subsequent off-line data reduction. A photograph of the LV system (transmitting optics) measuring the spanwise velocity in the AR310 extension duct is shown in Fig. 3-7.

The LV was operated in a dual beam or "fringe" mode in which light from the intersection of two incident beams having a wavelength of 0.5145 μm is heterodyned to detect the Doppler shift from an injected seed particle, at the local, instantaneous fluid velocity. In this mode, the LV measures the velocity component in the plane of the incident beams that is perpendicular to the bisector of the beams. The effective shape of the resultant measurement volume is an ellipsoid with major axis in the direction of the bisector of the beams.

The optical system used a 3.75X beam expander with a 762 mm focal length, 152 mm diameter (f/stop 5) transmitting lens. The beam expander was used to provide a smaller measurement volume, thus obtaining better resolution and high signal-to-noise ratio. The beam spacing into the beam expander was 35 mm for most of the measurements. This results in a measurement volume size of 1.6 by .13 mm (major and minor axis length). In order to obtain data in the corner of the AR630 duct, a beam spacing of 13 mm was used. The resulting measurement volume dimensions were 4.2 by .13 mm. Bragg shifting was employed to obtain 360 degree polar response of the measurement volume. The counter-type processor, TSI 1990B, was used to interpret the Doppler signal. A counter-processor measures the time for a particle to cross a desired number of fringes, converts the time into digital format, and transfers this data to the computer. This measurement represents one realization of velocity. For the current experiment 16 fringe crossing were required for each realization and 2048 realizations were taken for each velocity measurement. The processor was operated in the continuous mode (i.e. multiple measurements of one particle possible) in order to offset individual realization bias, as discussed in Ref. 22.

The computer was an IBM AT microcomputer. The acquisition software/hardware system was a modified version of the TSI 6230 two-channel system software (operated in one-channel mode). This system includes a TSI 6260 parallel interface card which resides in the computer and connects directly to the timer module of the processor. The modifications to the software include the addition of traverse table control and statistical editing procedures.

The time mean velocity components were estimated by the numerical average of all the realizations, that is

$$U = \frac{1}{N} \sum_{i=1}^{N} U_i \qquad (3\text{-}1)$$

where N is the sample size of the data point. The uncertainty in the velocity due to this estimate and the uncertainty due to bias errors are discussed in Appendix B. The turbulence (standard deviation) of the measured velocity was estimated as

$$\sigma = \sqrt{\frac{1}{(N-1)} \sum_{i=1}^{N} (U_i - U)^2} \qquad (3\text{-}2)$$

Each velocity sample (i.e. a set of realizations) was statistically edited by AEDC criteria (described by Patrick in Ref. 22) to remove bad data points due to noise. For the sample size of 2048, the AEDC criteria is to reject any data points outside the acceptance band of $\pm 3\sigma$ (calculated from the entire data sample). In addition, some individual data samples made in the corners had to be manually edited due to excessive noise.

The traversing of the measurement volume was accomplished with a TSI 9500 traversing table. This is a computer controlled, 3-axis traversing table. The entire optics package and laser were mounted on the table bed. An encoder readback system permitted highly accurate positioning. The overall uncertainty was ±0.013 mm. The table also has a manual tilt feature for measurements close to surfaces.

The seed material was one micron diameter titanium dioxide. It was injected using a fluidized bed seeder upstream of the flow conditioning on the tunnel centerline. The fluidized bed seeder had a centrifugal separator to eliminate large, agglomorated particles before injection. The measured seed size distribution indicated a sharp peak at one micron, confirming the successful operation of the centrifugal separator. The seed injection location was selected upstream of the flow conditioning in order to avoid flow disturbances in the inlet flow to the transition duct. Flow conditioning screens and perforated plates were periodically inspected for blockage due to seed material.

3.2.2 Pressure Measurement Instrumentation

Two different types of total pressure probes were used in this investigation. For documenting the overall total pressure distribution in the exit plane, a straight kielhead probe was employed. The probe was fabricated from a 0.159 cm diameter aspirated kielhead tube. The kielhead probe, which has a ±30 degree acceptance angle, was selected in order to accurately measure the total pressure in a secondary flowfield. The probe was inserted upstream from the exit of the extension duct to the exit measurement plane.

The other type of total pressure probe used was a boundary layer impact probe. It is shown schematically in Fig. 3-8. This probe was used to measure the inlet and exit boundary layers of the transition ducts. The probe was fabricated from 0.89 mm diameter hypodermic tube that was flattened at the tip, forming 0.30 mm x 1 mm sensing area (note the long side of the probe tip was parallel to the wall). For the inlet measurements, the probe shaft extended in the radial direction (of the circular inlet) and the probe end hooked in the upstream direction to minimize probe interference. For the exit boundary layers, the probe shaft extended upstream from the extension duct exit to the measurement plane. The probe end was offset from the probe shaft to minimize probe interference.

Both types of total pressure probes were traversed within the x,y plane with a Daedal/Compumotor positioning table system. This system is computer controlled and has encoder feedback capability to permit high positioning accuracy (±0.013 mm).

3.2.3 Measurement Locations

The locations of the exit plane LV and total pressure measurements are shown in Fig. 3-9 for the AR310 transition duct. The LV data consists of the three components of the velocity vector (along the reference axes shown in Fig. 3-1) at the 168 measurement locations shown. The coarse grid spacing over the entire exit plane was chosen to verify the flow symmetry about the y and z axes. After flow symmetry was verified, additional measurements were made in the lower quadrant in order to investigate the flow features in more detail.

The locations of the exit plane, total-pressure boundary-layer surveys are shown in Fig. 3-10. Each survey is identified by a number and a symbol which will be used for ease of data presentation. As seen in the figure, surveys are along the spanwise and transverse directions. In addition, corner surveys along the radial direction were taken.

The corresponding measurement locations for AR630 transition duct are shown in Figs. 3-11 and 3-12. In Fig. 3-11, the 154 measurement locations of LV and total pressure measurements are shown. Similar to the AR310 data matrix, a coarse grid spacing was employed to verify flow symmetry and more a detailed spacing was then performed over a symmetric region. Due to obstructed optical access, it was impossible to obtain LV data at some of the corner points of the AR630 transition duct. In Fig. 3-12 the total-pressure boundary-layer survey locations are shown. Note that no radial surveys were taken.

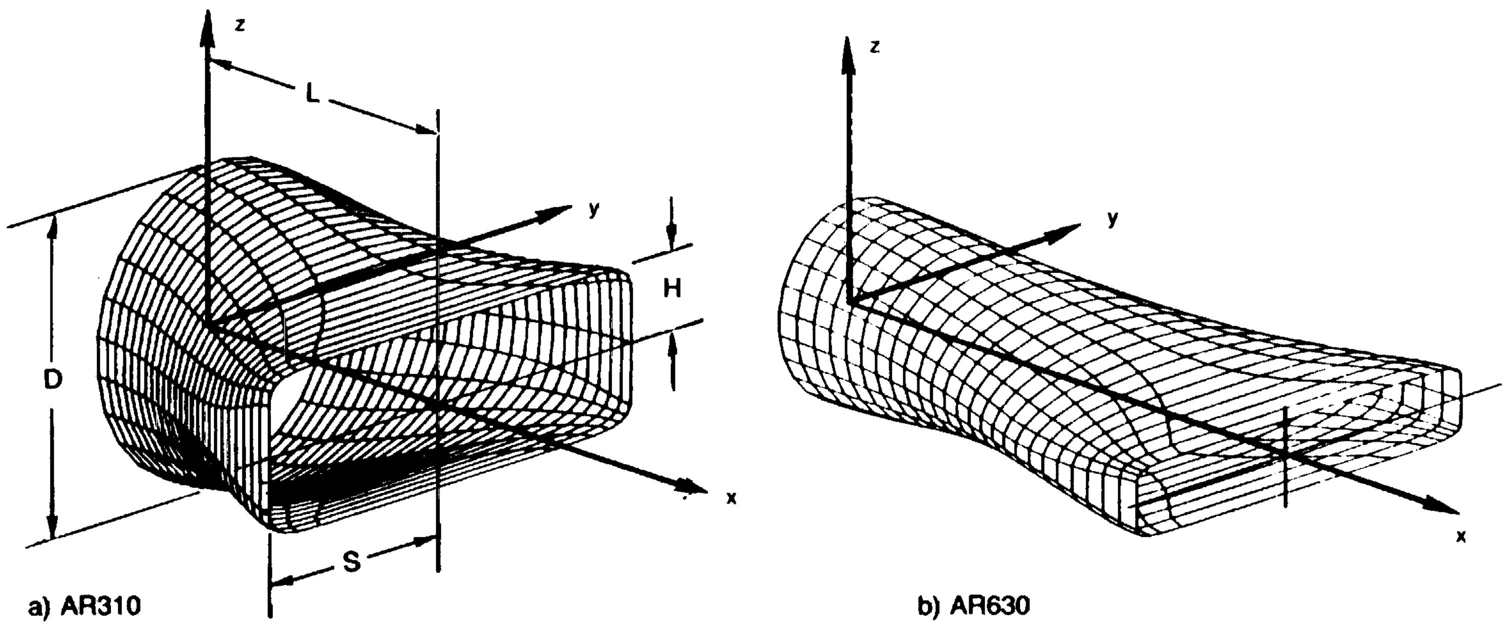

Figure 3-1. — Schematic of Transition Ducts Illustrating Coordinates and Nomenclature

87-9-19-47

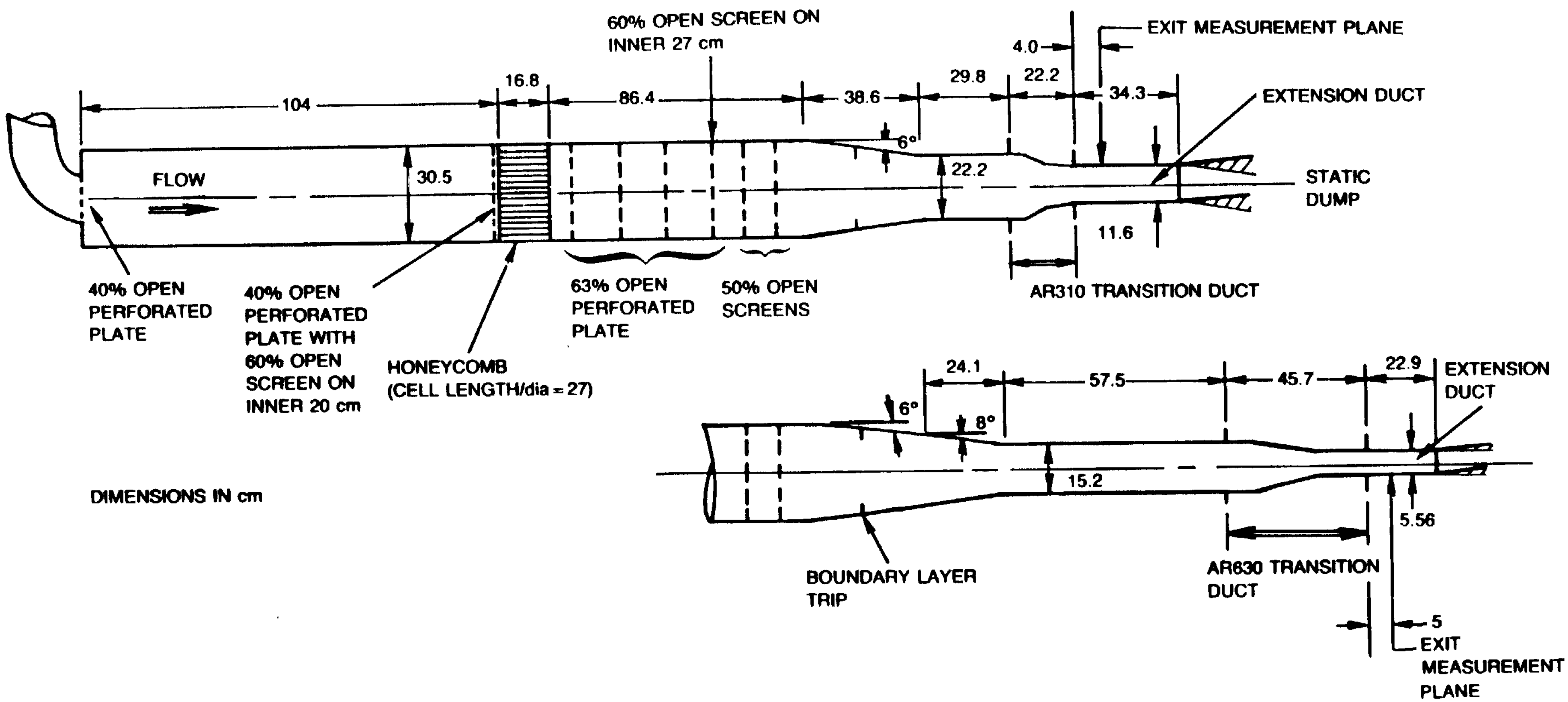

Figure 3-2. — Schematic of Test Centerline Illustrating Flow Conditioning

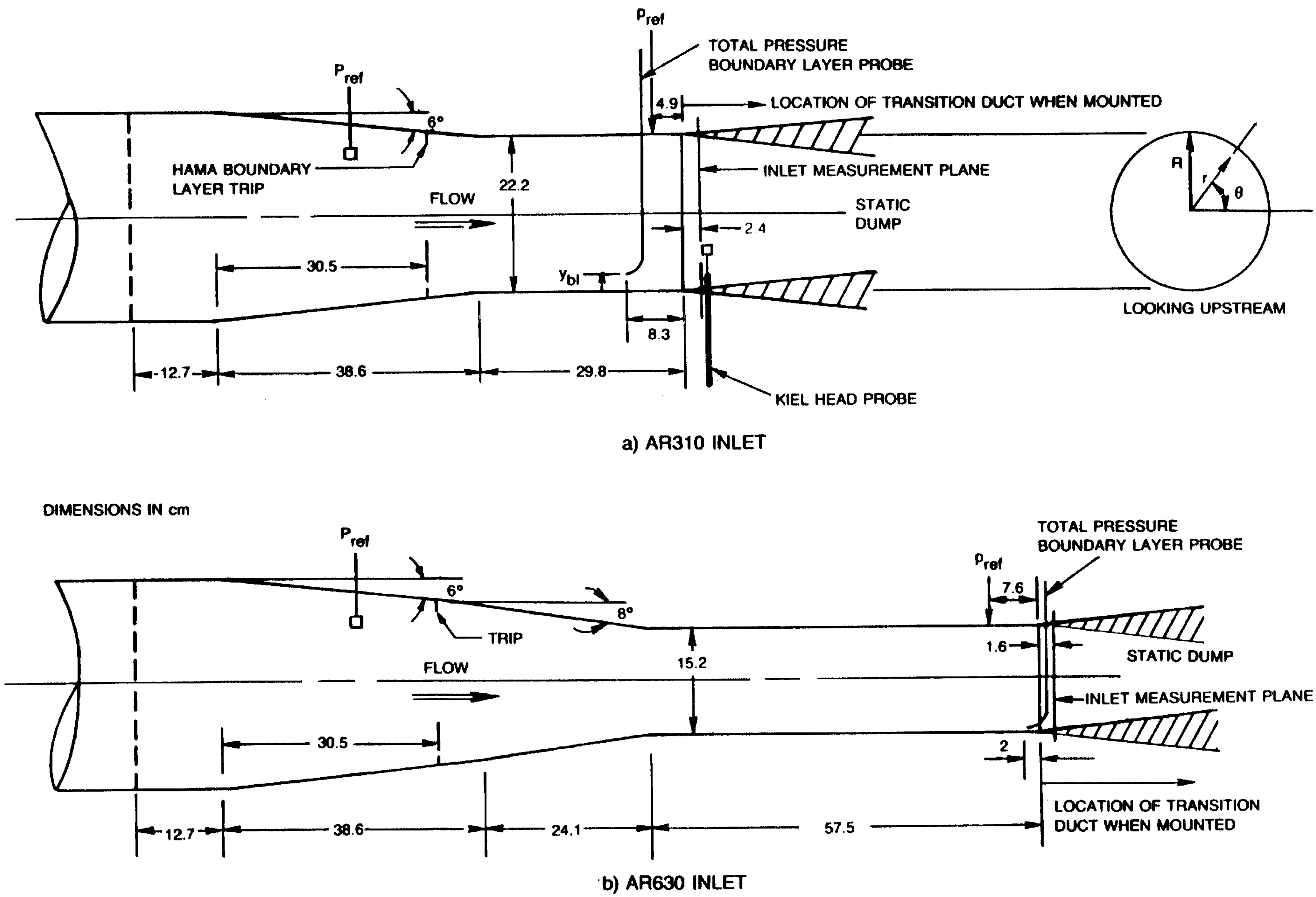

Figure 3-3. — Transition Duct Inlet Definition

87-9-19-49

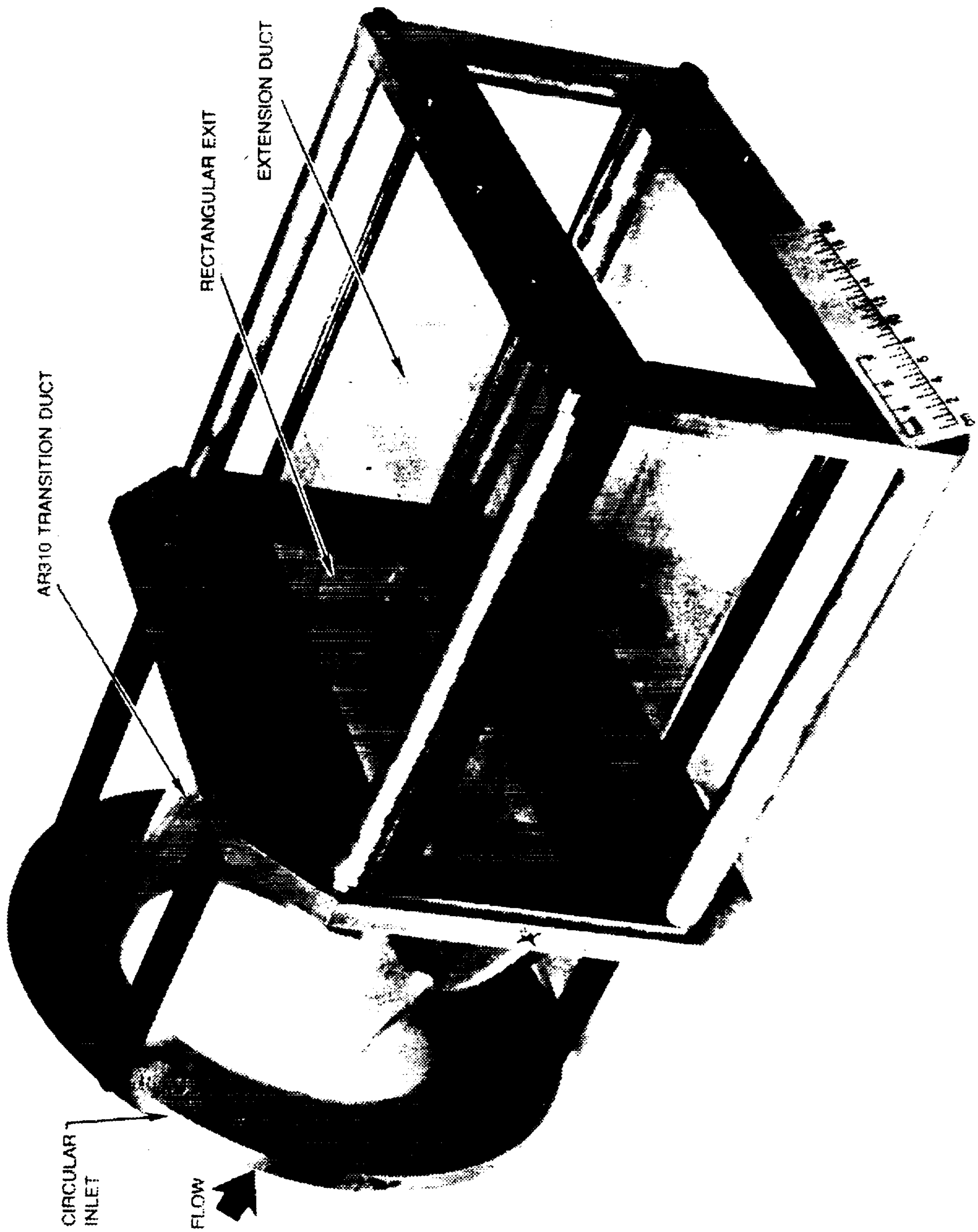

Figure 3-4. — AR310 Transition Duct With Constant Area Extension

87 - 9 - 19 - 52
87 - 366 - A

ORIGINAL PAGE
BLACK AND WHITE PHOTOGRAPH

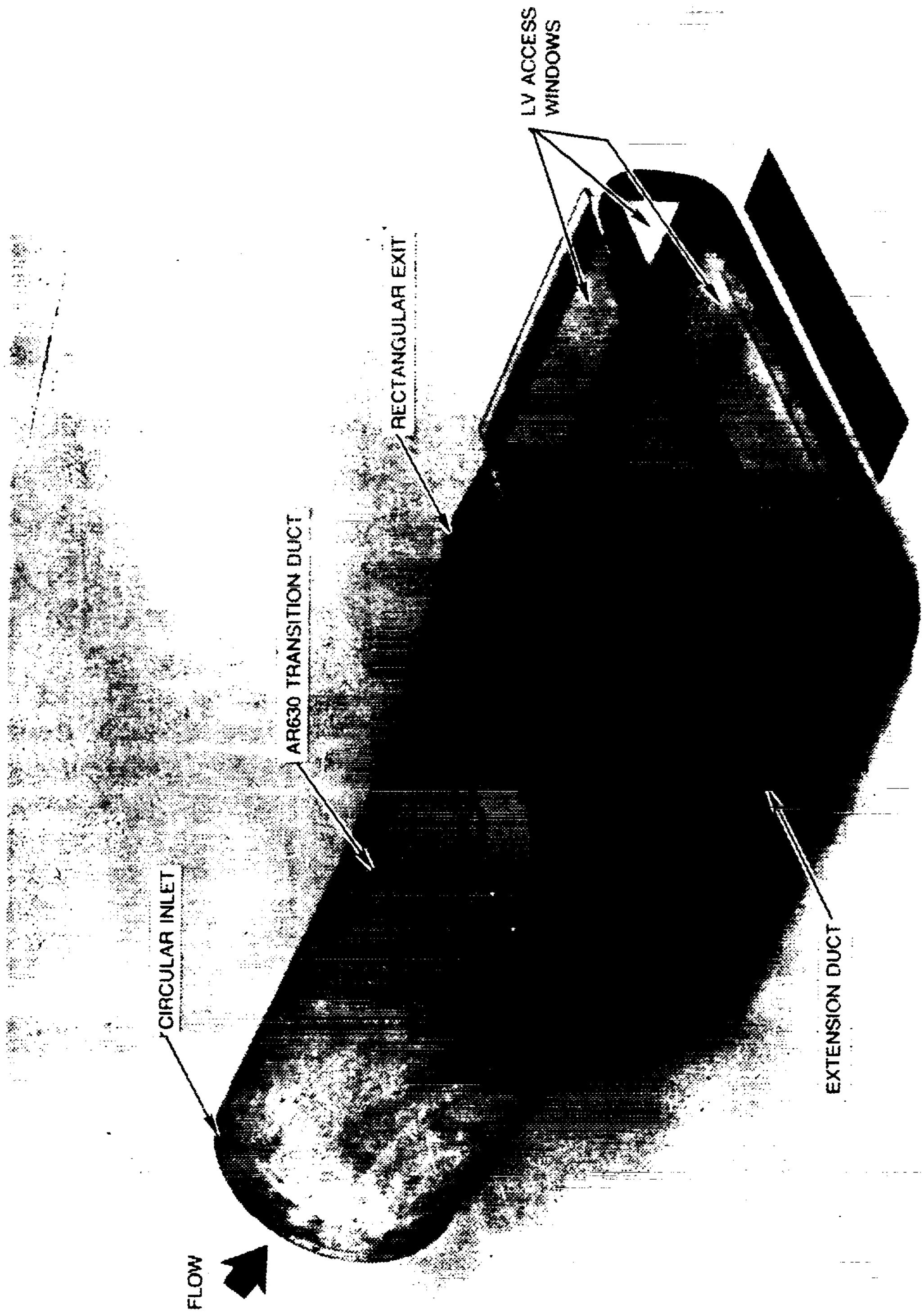

Figure 3-5. — AR630 Transition Duct With Constant Area Extension

ORIGINAL PAGE
BLACK AND WHITE PHOTOGRAPH

87-9-19-51

87-368-B

87-9-19-2

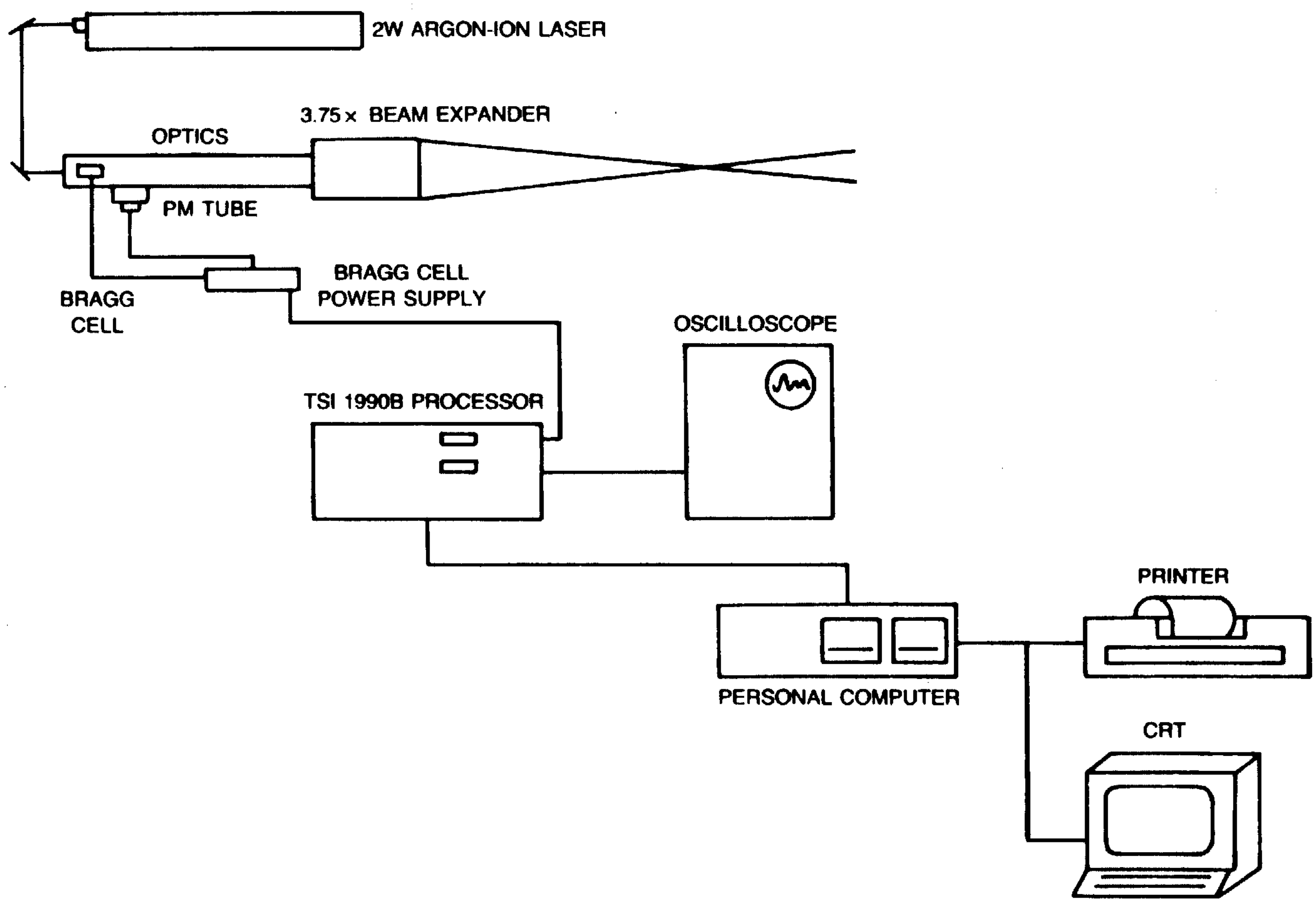

Figure 3-6. — Laser Velocimeter Data Acquisition System

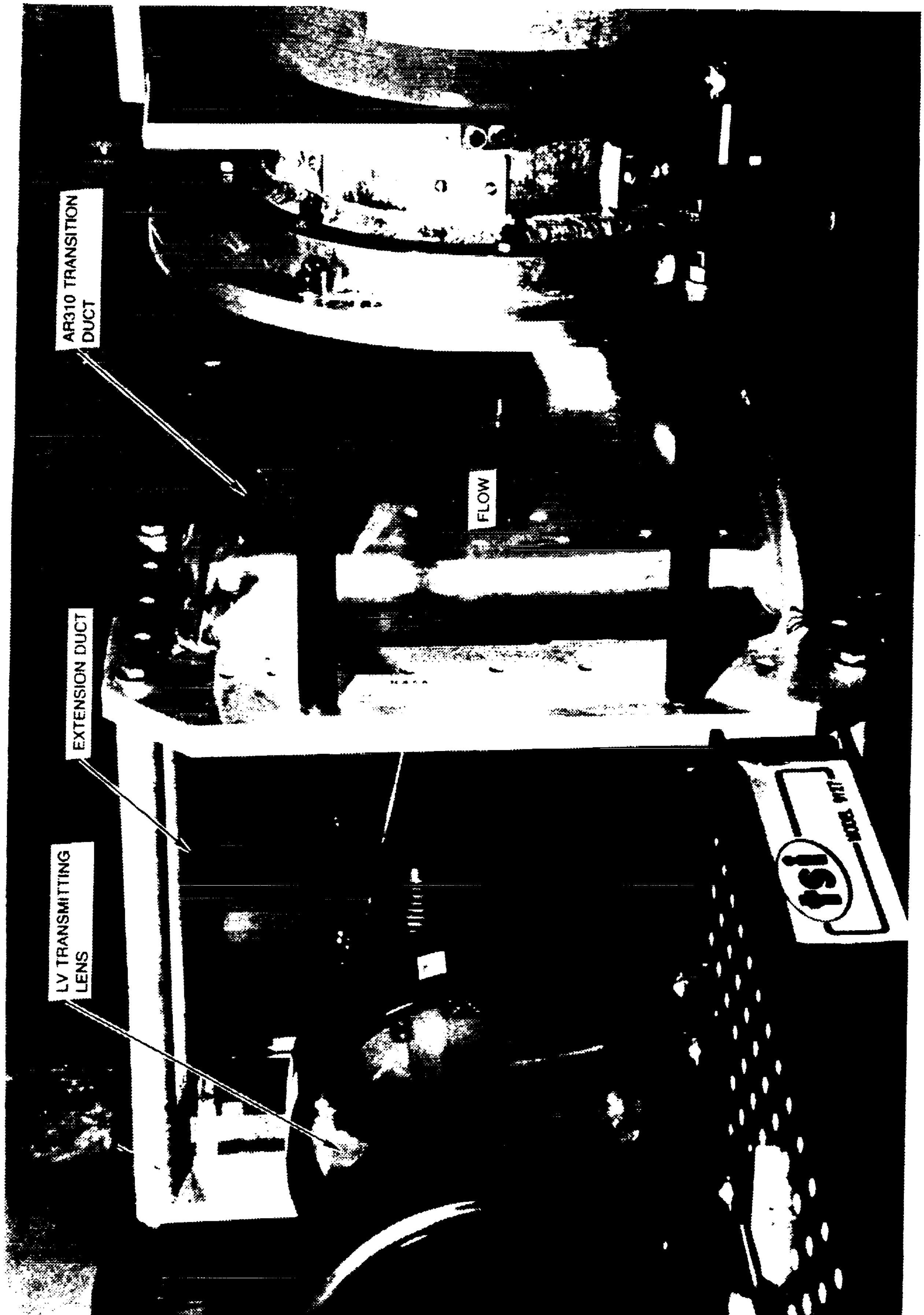

Figure 3-7. — AR310 Transition Duct With LV System

87-9-19-50
87-20-5

ORIGINAL PAGE
BLACK AND WHITE PHOTOGRAPH

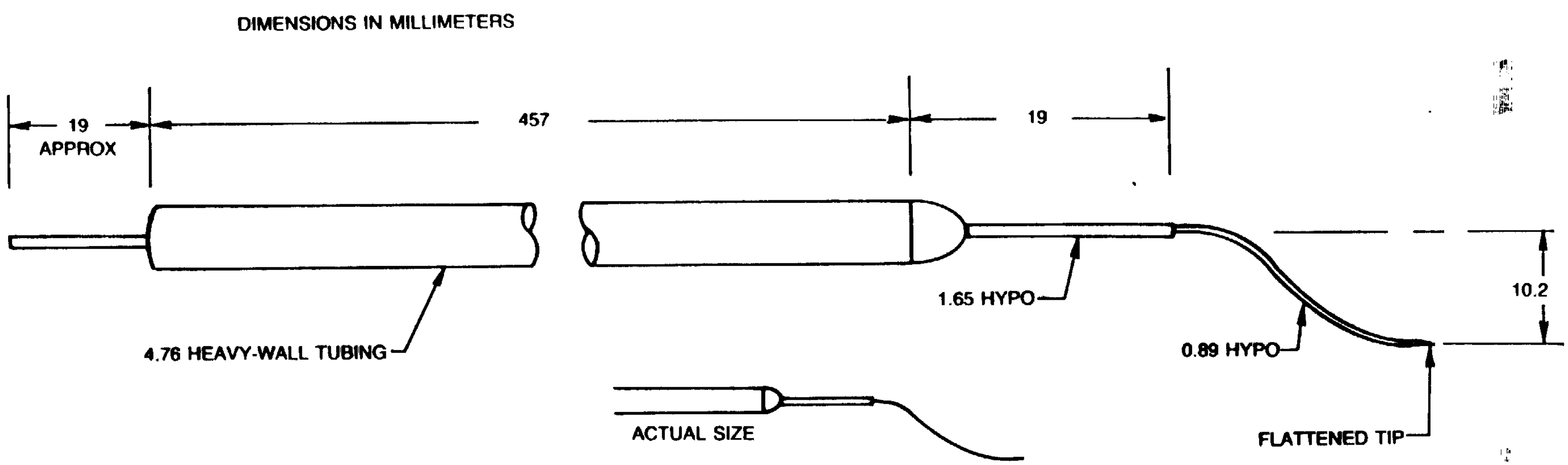

Figure 3-8. — Boundary Layer Probe for Transition Duct Exit Plane Measurements

87-9-19-3

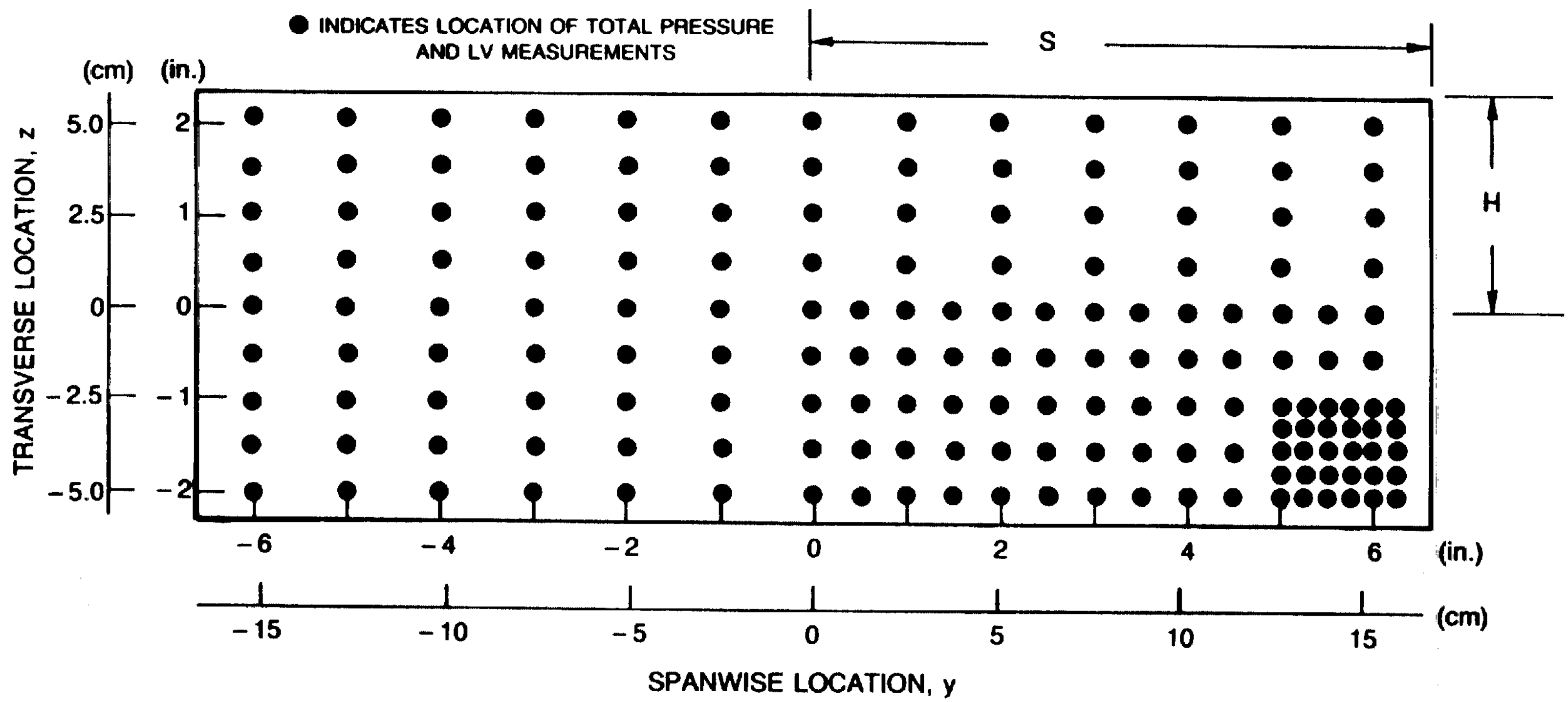

Figure 3-9. — Coordinate System Definition and Measurement Locations at Exit of AR310 Transition Duct

87-9-19-4

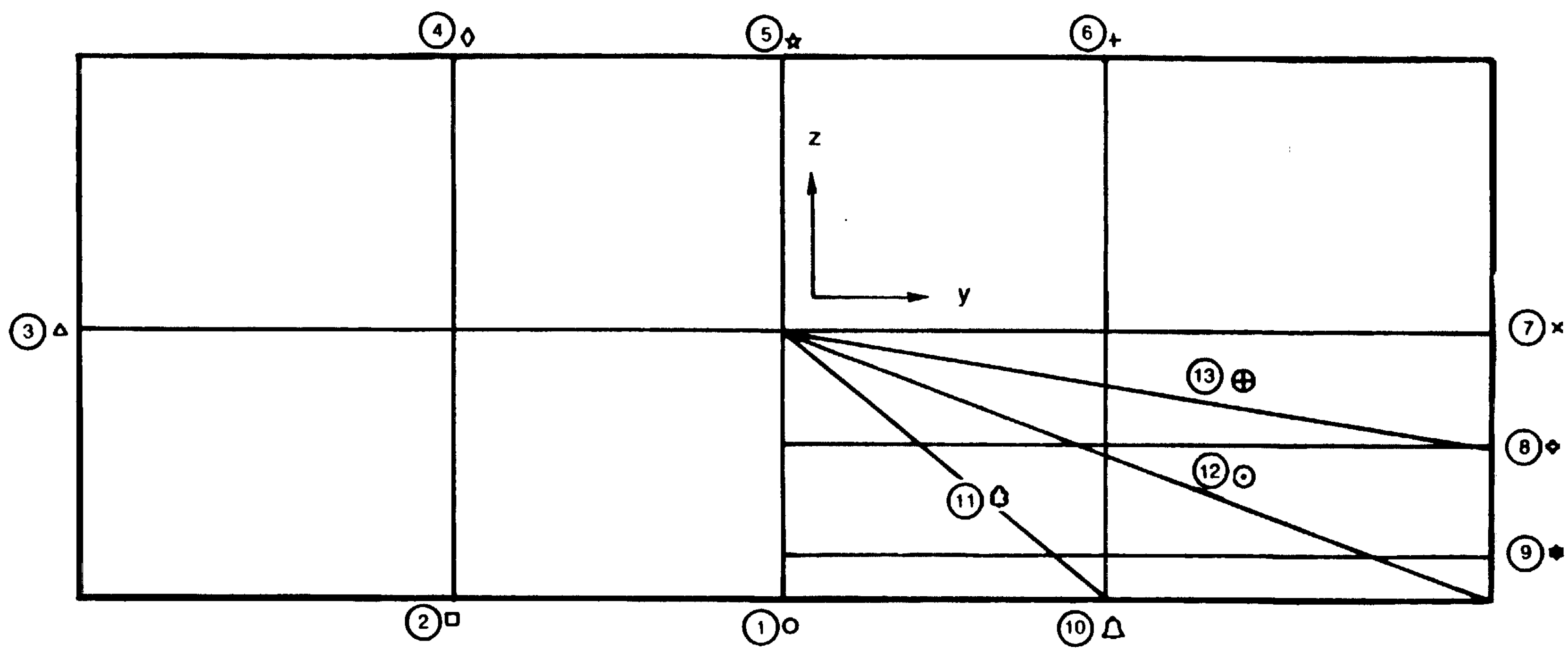

Figure 3-10. — Locations of Boundary Layer Traverses in AR310 Exit Plane

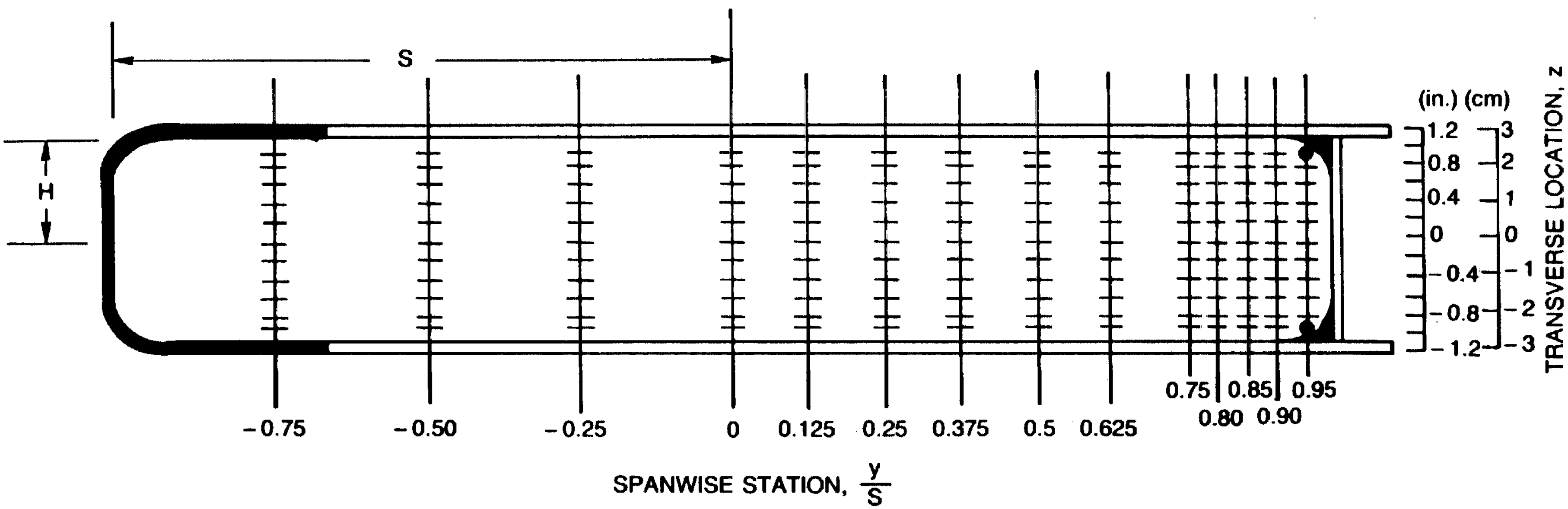

+ INDICATES LOCATION OF TOTAL PRESSURE AND LV MEASUREMENTS

● INDICATES LOCATION OF TOTAL PRESSURE MEASUREMENTS ONLY

Figure 3-11. — Coordinate System Definition and Measurement Locations for AR630 Transition Duct

87-9-19-6

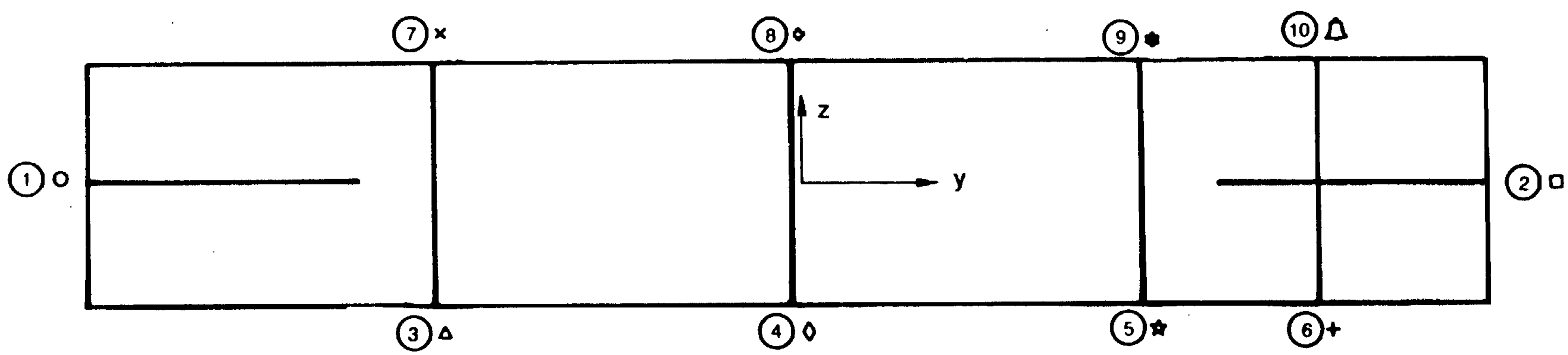

Figure 3-12. — Locations of Boundary Layer Traverses in AR630 Exit Plane

87-9-19-7

CHAPTER 4

RESULTS

Velocity and pressure data obtained in this study are presented in both tabular and graphical format. Velocity data have been normalized by the freestream velocity, U_{ref}, at the tunnel reference location in the constant area approach duct upstream of the test section inlet. U_{ref} was calculated from Q_{ref}, the freestream dynamic pressure, which was determined from the freestream total pressure, P_{ref}, measured with the inlet kielhead probe and the reference static pressure, p_{ref} (see Fig. 3-3). U_{ref} equaled 30.48 m/sec (100 ft/sec) at nominal tunnel operating conditions (T_{ref} = 15°C, 59° F and p_{ref} = 760 mmHg, 14.7 psia). U_{ref} was adjusted to maintain constant unit Reynolds number equal to 1.94 x 10^5/m at the reference location when the tunnel conditions deviated from nominal. Static pressures are presented relative to the tunnel static pressure at the reference location. All pressures, static and total, were normalized by Q_{ref}. The coordinates used for the presentation of results are x, distance downstream from the start of the test section (see Fig. 3-1), y, spanwise position relative to the test section centerline, and z, transverse position relative to the test section centerline. Results for the AR310 and AR630 ducts are presented sequentially in the following sections. For each duct, flow conditions in the inlet plane are defined by total pressure and mean velocity profiles across the duct to determine flow uniformity, transverse velocity profiles to certify the inlet flow to be free of swirl, law-of-the-wall velocity plots determined from pitot measurements to characterize the turbulent inlet boundary layer, and axial and transverse turbulence levels to provide input for computational codes. Similar data measured in the exit plane is presented in the form of 2-D and 3-D contour plots and vector plots of the cross-stream velocity fields. Quantities such as kinetic energy, flowfield static pressures, and axial vorticity distributions in the exit plane, which have been derived from these directly measured quantities, will be presented also.

4.1 Measurements in AR310 Transition Duct

4.1.1 Inlet Plane Total Pressure Measurements

4.1.1.1 Mean Flowfield Measurements

Kielhead total pressure traverses were made across the inlet duct at 45 degree azimuthal spacings. Measurements were conducted 2.4 cm downstream from the exit plane of the AR310 inlet duct in a static dump test as shown schematically in Fig. 3-3. The measured profiles, shown in Fig. 4-1, are flat to within ±1.5 percent of Q_{ref} except for the outer 20 percent of the flow influenced by the duct wall boundary layers. The inlet boundary layer thickness,

δ_{995}, determined from the point at which the dielhead total pressure in the boundary layer equaled 99 percent of the freestream total pressure (i.e. the same point at which the velocity calculated from the total pressure reached 99.5 percent of the freestream velocity) was 10 percent of the inlet diameter.

4.1.1.2 Boundary Layer Measurements

Forty-point pitot traverses were made within the boundary layer at x = -8.3 cm in a static dump test as shown schematically in Fig. 3-3. The boundary layer thickness, δ_{995}, determined from the pitot measurements was 2.2 cm (0.87 in) which equaled 9.9 percent of the inlet diameter which was in agreement with the boundary layer thickness indicated by the kielhead measurements. Integral properties calculated for the boundary layer at the AR310 inlet are tabulated below:

Displacement thickness, $\delta^* = .179$ cm
Momentum thickness, $\theta = .135$ cm
Shape factor, H = 1.33
Momentum thickness Reynolds no. = 3244
Reynolds no. based on inlet diameter = 5.25×10^5

The velocity profile of the inlet boundary layer is plotted in "law-of-the-wall" (U^+ vs. y^+) coordinates in Fig. 4-2. To calculate the data points in Fig. 4-2 the friction velocity, U_τ, was chosen to minimize the least-squares fit to the equation

$$U^+ = \frac{U}{U_\tau} = \frac{1}{0.41} \ln y^+ + 5.0 \qquad (4\text{-}1)$$

where $y^+ = yU_\tau/\nu$ as recommended by Coles (Ref. 23) over the log-linear region of the profile ($50 < y^+ < 500$). Then the skin friction could be calculated from the equation

$$C_f = 2\,\frac{U_\tau^{\,2}}{U_{ref}^{\,2}} \qquad (4\text{-}2)$$

Using this equation, the value of skin friction has been calculated to be 0.00384. The strength of the boundary layer wake component, determined as the maximum deviation, ΔU^+, of the data from Eq. (4-1) was 1.5. This value is in agreement with the value quoted by Coles for an equilibruim turbulent boundary layer having the same momentum thickness Reynolds number and freestream turbulence level.

A tabular listing of the data points in physical and "law-of-the-wall" coordinates is given in Table IIa.

4.1.2 Inlet Plane Laser Velocimeter Measurements

Laser velocimeter measurements were obtained in a plane located 2.4 cm downstream from the end of the inlet duct. The four twenty-three point radial traverses were spaced 45 degrees apart around the azimuth.

4.1.2.1 Mean Velocity Measurements

Axial velocity profiles, U/U_{ref} vs. r/R, are plotted in Fig. 4-3. The profiles are flat to within ±.01 U_{ref} over the central 80 percent of the flowfield which was uninfluenced by the sidewall boundary layer and/or free jet shear layer except for three data points near r/R = 0.8 on the θ = 90 degree traverse.

The transverse velocity, W, was measured at the same locations as the axial velocity component to quantify the intensity of swirl in the inlet flow. The measured transverse velocity component, plotted as W/U_{ref} vs r/R in Fig. 4-4, exceeded .01 U_{ref} at only six points within the central 95 percent of the flow and at those six points W/U_{ref} did not exceed 0.015. These values are sufficiently low to certify the inlet flow to the AR310 duct to be swirl free.

4.1.2.2 Turbulence Measurements

Profiles of axial turbulence intensity, $\sqrt{u^2}/U_{ref}$ vs. r/R, are plotted in Fig. 4-5 for each of the four LV traverses in the inlet plane of the AR310 duct plane. The axial turbulence had a uniform 1.8 percent turbulence intensity throughout the freestream flow. Near the periphery of the duct the axial turbulence intensity approached 0.10 U_{ref}. These values are normal for near-wall turbulence intensities within a turbulent boundary layer. Boundary layer measurements made on a flat plate by Klebanoff (Ref. 24) indicated a maximum turbulence intensity in the near wall region equal to 9 percent of the local freestream velocity.

Profiles of transverse turbulence intensity, $\sqrt{w^2}/U_{ref}$ vs. r/R, are plotted in Fig. 4-6. The transverse turbulence profiles have more data scatter than the axial turbulence profiles but the average value of the transverse turbulence is .018 U_{ref}, which is equal to the axial turbulence intensity.

4.1.3 Exit Plane Total Pressure Measurements

As noted above in Fig. 3-9, total pressure measurements were obtained at 168 locations in the exit plane of the AR310 duct. The exit plane measurement station was located 4.0 cm downstream from the end of the transition section within the constant area extension section. A tabular listing of the data is given in Table IIIa in terms of $(P - P_{ref})/Q_{ref}$.

4.1.3.1 Mean Flowfield Measurements

The measured total pressure distribution throughout the exit measurement plane of the AR310 duct is plotted in Fig. 4-7a as contour lines of constant $(P-p_{ref})/Q_{ref}$. Three aspects of the data presentation should be noted. First, the frame formed by the y/S and z/H axes is drawn to scale and has the shape of the cross section at the exit measurement plane. Second, the contours are plotted only to the extent of the cross section over which data was taken. The contours were not extrapolated to the wall. Third, the contour plot is presented in an exploded format to permit an examination of the differences in the details of the contours calculated from data obtained on the coarse, medium, and fine grid spacings depicted in Fig. 3-9.

The largest contour plot, obtained from data taken on the coarse measurement grid, shows that the flow is symmetric in the exit plane. A large region of essentially inviscid flow existed in the duct core where the total pressure exceeded 95 percent of Q_{ref} over 70 percent of the duct cross-sectional area. Total pressure losses in excess of 0.10 Q_{ref} were confined to the duct corners.

The contours calculated from data taken on the medium and fine measurement grids differed only slightly from the coarse grid contours. They did not delineate any features of the fluid physics which were not seen in the coarse grid measurements.

A three-dimensional plot of the exit plane total pressure distribution generated from data taken on the coarse measurement grid is shown in Fig. 4-7b. The flat total pressure profile within the core flow and the concentration of the losses in the duct corners are readily apparent in the 3-D graphic.

4.1.3.2 Boundary Layer Measurements

As noted above in Fig. 3-10, boundary layer traverses were made at thirteen locations in the exit plane of the AR310 duct at the same axial location as the kielhead total pressure measurements. The thirteen traverses consisted of six in the transverse direction, four in the spanwise direction, and three radial traverses near the duct corner.

The transverse total pressure profiles are plotted in Fig. 4-8a. The transverse boundary layers were thin and had well-behaved turbulent profiles at all six traverse locations. The thinnest boundary layers occurred at traverse locations 1 and 5 at the midspan location along the exit plane semi-minor axis where δ_{995} equaled .12H, i.e. 12 percent of the duct half-heighth. At traverse locations 2, 4, 6, and 10 located at $y/S = \pm.5$ the boundary layer thickness was approximately .2H.

The spanwise total pressure profiles are plotted in Fig. 4-8b. The spanwise boundary layers were much thicker than the transverse boundary layers. The thinnest spanwise boundary layers were measured at traverse locations 3 and 7 along the exit plane semi-major axis, where the boundary layer thickness was approximately 0.75 H. At traverse location 8 at $z/H = -0.44$, the boundary layer was thicker, $\delta_{995} = 1.0$ H, but the turbulent profiles remained well behaved. However, at traverse location 9 an inflection point was measured in the total pressure profile.

The location of the inflection point corresponded with the inflection point in traverse 12 shown in Fig. 4-8c. The S-shaped profile along traverse 12 could indicate the presence of a vortex core at $y_{bl}/H = 0.25$ ($y/S = 0.92$, $z/H = -0.92$). Profiles 11 and 13 are sufficiently removed from the duct corner to be uninfluenced by the axial vortex.

Eleven of the boundary layer profiles were integrated to determine the displacement and momentum thicknesses. Profiles at locations 8 and 9 were not integrated since these profiles do not extend outside the boundary layer. As will be discussed in Section 4.1.4.2 there are significant normal pressure gradients at the exit plane that must be accounted for in the calculation, of the displacement and momentum thicknesses. The method of Kooi (Ref. 25) which accounts for normal pressure gradients in the calculated displacement and momentum thicknesses was used such that

$$\delta^* = \int_0^\delta \left(1 - \frac{U}{U_{iw}}\right) dy - \int_0^\delta \left(1 - \frac{U_i}{U_{iw}}\right) dy \qquad (4\text{-}3)$$

and

$$\theta = \int_0^\delta \frac{U}{U_{iw}} \left(1 - \frac{U}{U_{iw}}\right) dy - \int_0^\delta \frac{U_i}{U_{iw}} \left(1 - \frac{U_i}{U_{iw}}\right) dy \qquad (4\text{-}4)$$

respectively. Here U_{iw} is the inviscid axial velocity at the wall calculated from the local wall static pressure and inlet total pressure. The local inviscid axial velocity, U_i, is given by

$$U_i = \sqrt{\frac{2}{\rho}(P - p) - {V_i}^2 - {W_i}^2} \qquad (4\text{-}5)$$

where V_i and W_i are unknown but estimated by the measured LV values. Since these terms are small, the approximation is reasonable. Eq. (4-5) assumes the boundary layer probe is sensitive to all three components of velocity. For boundary layer survey points between LV data points, linear interpolation was applied. Between the LV data point closest to the wall and the wall, the tangential component of velocity was assumed constant and the normal component was linearly interpolated to zero. For the local static pressure, p, the values calculated in Section

4.1.4.2 were used. The local wall static pressure was assumed equal to the value closest to the wall (that is, a negligible normal pressure gradient was assumed for the inner portion of the boundary layers). Note that the first terms in Eqs. (4-3) and (4-4) are the classic definitions of the integral parameters and the second terms are corrections to account for the normal pressure gradients.

The results of the calculated integral parameters are shown in Fig. 4-8d in terms of the displacement and momentum thicknesses normalized by the duct half-height (H), and the shape factor. For the transverse surveys the displacement thicknesses is about 2 percent of the half-height whereas the spanwise surveys are much thicker at 6-7 percent. The shape factors all tend to be reasonable for turbulent boundary layers with values between 1.28-1.43 (neglecting surveys 11, 12, and 13 which are not normal to the surface).

The boundary layer profiles obtained at locations 1, 3, 5, and 7 along the duct semi-major and semi-minor axes are plotted in law-of-the-wall coordinates in Fig. 4-9. The spanwise profiles, 3 and 7, are nearly identical, and the transverse profiles, 1 and 5, also differ only slightly indicating minor asymmetry existed in the duct exit flow. However, the profiles, which appeared well behaved when plotted in linear coordinates in Fig. 4-8, do not have the extended log-linear regions and wake profiles characteristic of equilibrium turbulent boundary layers.

4.1.4 Exit Plane Laser Velocimeter Measurements

As noted above in Fig. 3-9, laser velocimeter measurements were obtained at each of the 168 total pressure measurement locations in the exit plane of the AR310 duct. Three mean velocity components, U, V, and W, and three components of turbulence $\sqrt{u^2}$, $\sqrt{v^2}$, and $\sqrt{w^2}$ were determined from three 168-point traverses with a single component LV system. These velocity measurements are given in Table IIIa (normalized by U_{ref}).

4.1.4.1 Mean Velocity Measurements

LV measurements of the axial velocity distribution in the exit plane of the AR310 duct are shown in a 3-D plot in Fig. 4-10a. The measured flowfield appears to have a nearly inviscid velocity distribution relatively uninfluenced by viscous wall boundary layers. Gradients in the mean flow exist in both the transverse and spanwise directions. In the transverse direction, the profile is slightly concave due to an overspeed of approximately .05 U_{ref} at the edges of the top and bottom wall boundary layers. In the spanwise direction, the profile is slightly convex with higher axial velocities in the center of the duct. A two-dimensional representation of the axial velocity data is shown in Fig. 4-10b where contours of U/U_{ref} have been plotted. The data corroborates the total pressure data described above which indicated that the flow field was nearly potential with the effects of viscosity limited to thin wall boundary layers and corner flows.

The cross-flow velocity vectors measured in the AR310 exit plane are plotted in Fig. 4-11. Four aspects of the data shown in Fig. 4-11 should be noted. First, the magnitude of the cross-flow does not exceed 15 percent of U_{ref} at any measurement location and is typically on the order of .05 U_{ref}. Second, the pattern of the cross-flow vectors shows excellent flow symmetry in the exit measurement plane. Third, the direction of the cross-flow is predominantly outward, indicating that the mean flow is continuing to adjust toward a more uniform profile in the constant area extension duct. Fourth, in the lower right corner of the figure where measurements were taken on a fine grid spacing the cross-flow vectors indicate the presence of a weak axial vortex in the corner.

The cross-flow velocity components were combined with the axial velocity components to determine the kinetic energy distribution in the AR310 exit plane. Contours of constant kinetic energy are plotted in Fig. 4-12. The gradients in the kinetic energy distribution are primarily in the spanwise direction.

4.1.4.2 Calculated Exit Plane Static Pressure Distribution

With the assumption of constant density across the AR310 exit plane, the Bernoulli equation was used to calculate the local static pressure from the measured total pressure and the kinetic energy at each of the 168 measurement locations in the exit plane. The calculated static pressure field plotted in three dimensions in Fig. 4-13a is non-uniform and predominantly concave in shape. The non-uniformity in static pressure across the exit plane was approximately equal to .25 Q_{ref} except at local spikes near the periphery of the measurement field. The higher static pressure along the duct sidewalls is due to the side-wall influence in setting up the potential flow pressure pattern necessary to turn the flow toward the axial direction in the exit duct. Contours of constant static pressure plotted in Fig. 4-13b show that the calculated static pressure over the central 75 percent of the exit duct is lower than the reference pressure indicating that the core flow has been over accelerated in the transition section.

4.1.4.3 Turbulence Measurements

Due to optical access limitations some of the LV cross-flow velocity measurements near the duct walls were made at various known small inclination angles. The slight misalignment of the fringe pattern in the measurement volume relative to purely spanwise or transverse directions required the mean cross-flow velocities to be determined trigonometrically from pairs of inclined spanwise and transverse measurements. Spanwise and transverse turbulence components cannot be so reconstructed from measurement pairs without knowledge of the cross stress component.

Therefore, in this section, only axial turbulence components, which were measured directly at all measurement locations in the exit plane, are presented graphically. Values of transverse and spanwise turbulence components at all measurement locations are listed in Table IIIa. Values which are considered contaminated due to beam tilt are denoted parenthetically with the beam tilt to the right of the measurement.

The distribution of the axial component of turbulence in the AR310 exit plane is shown in Fig. 4-14 in which lines of constant axial turbulence level are plotted. The turbulence level throughout the core flow is less than .02 U_{ref}, the same level of turbulence measured in the inlet flow (see Fig. 4-5). Regions of higher turbulence intensity are confined to the duct corners. Overall, the axial turbulence level distribution in the AR310 exit plane is quite symmetric.

4.2 Measurements in AR630 Transition Duct

4.2.1 Inlet Plane Total Pressure Measurements

Total pressure traverses were made across the inlet duct at 0 deg and 90 deg azimuthal locations. Measurements were obtained 2 cm upstream from the exit plane of the AR630 inlet duct in a static dump test as shown schematically in Fig. 3.3.

4.2.1.1 Mean Flowfield Measurement

The measured total pressure profiles from the 0 deg and 90 deg azimuthal locations have been plotted together in Fig. 4-15. The profiles are flat to within ±1 percent of Q_{ref} except for the outer 20 percent of the flow influenced by the duct wall boundary layers.

4.2.1.2 Boundary Layer Measurements

The boundary layer thicknesses, δ_{995}, determined from the pitot tube traverses were 1.524 cm (0.600 in) and 1.534 cm (0.604 in) at the 0 deg and 90 deg azimuth positions, respectively. These values equaled 10 percent of the inlet diameter. Integral properties calculated for the boundary layers at the AR630 inlet are tabulated below:

	θ = 0 deg	θ = 90 deg	average
Displacement thickness, δ^* (cm)	0.179	0.175	0.177
Momentum thickness, θ (cm)	0.132	0.129	0.131
Shape factor, H	1.36	1.36	1.36
Momentum thickness Reynolds no., Re_θ	2702	2727	2715

The inlet boundary layer velocity profiles are plotted in "law-of-the-wall" (U^+ vs. y^+) coordinates in Fig. 4-16. The profiles have a well-behaved log-linear region and a wake strength, ΔU^+, of 1.5, which equaled the value calculated for the inlet boundary layer to the AR310 transition duct. Using Eq. (4.2) a skin friction, C_f, value of 0.00363 has been calculated for the boundary layers.

A tabular listing of the data points in physical and "law-of-the-wall" coordinates is given in Table IIb.

4.2.2 Inlet Plane Laser Velocimeter Measurements

Laser velocimeter measurements were taken 1.6 cm downstream from the end of the inlet duct. Four twenty-five point radial traverses were spaced 45 degrees apart around the azimuth.

4.2.2.1 Mean Velocity Measurements

Axial velocity profiles, U/U_{ref} vs. r/R, are plotted in Fig. 4-17. The profiles are flat to within ±.01 U_{ref} over the central 80 percent of the flowfield which was uninfluenced by the sidewall boundary layer and/or free jet shear layer.

The transverse velocity component, W, which was measured at the same locations as the axial velocity component is plotted as W/U_{ref} vs. r/R in Fig. 4-18. The average transverse velocity measured in the freestream was -.003 U_{ref}. This transverse velocity is equivelent to the apparent transverse velocity component which would be measured in a purely axial flow due to an 0.17 degree misorientation of the LV fringe pattern relative to the axial direction. Measured transverse velocities were within 0.01 U_{ref} of the mean transverse velocity throughout the core flow. As for the AR310 inlet flow, these values are sufficiently low to certify the inlet flow to the AR630 duct to be swirl free.

4.2.2.2 Turbulence Measurements

Profiles of axial turbulence intensity, $\sqrt{\overline{u^2}}/U_{ref}$ vs. r/R, are plotted in Fig. 4-19 for each of the four LV traverses in the inlet plane of the AR630 duct. The axial turbulence had a uniform 2.4 percent level throughout the freestream flow. Near the periphery of the duct axial turbulence levels rose to 0.15 U_{ref}.

Profiles of transverse turbulence intensity, $\sqrt{\overline{w^2}}/U_{ref}$ vs. r/R, are plotted in Fig. 4-20. The transverse turbulence had a uniform 1.0 percent turbulence intensity throughout the freestream flow. Near the periphery of the duct transverse turbulence levels exceeded 0.10 U_{ref}.

4.2.3 Exit Plane Total Pressure Measurements

As noted above in Fig. 3-11, total pressure measurements were obtained at 154 locations in the exit plane of the AR630 duct. The exit plane measurement station was located 5 cm downstream from the end of the transition section within the constant area extension section. A tabular listing of the data is given in Table IIIb in terms of $(P - p_{ref})/Q_{ref}$.

4.2.3.1 Mean Flowfield Measurements

The measured total pressure distribution throughout the exit measurement plane of the AR630 duct is presented in Fig. 4-21a as a three-dimensional plot. The spacing of the vertical lines in the plot indicates the density of the grid used to interpolate the data between measured data points. For $y/S > 0$, where the measurement density was low, the grid density was correspondingly low.

Three features of the flow can be deduced from Fig. 4-21a. First, the total pressure distribution in the exit plane is symmetric within the limits of the measurement grid. Second, most of the flow in the exit duct has an inviscid flat total pressure profile uninfluenced by the sidewall boundary layers except near $y/S = 0.9$ where the third feature, a local minimum in the total pressure occurs along the duct semi-major axis.

Quantitative details of the total pressure distribution in the AR630 exit plane can be seen more clearly in Fig. 4-21b where contour lines of constant $(P-p_{ref})/Q_{ref}$ have been plotted for the half of the exit plane, $y/S > 0$, containing the detailed measurement grid. Note that the superelliptic shape of the exit duct has been drawn to scale on the figure and the contours are only plotted over the portion of the cross section over which data had been taken. The total pressure at $y/S = 0.9$, $z/H = 0$, the location of the local minimum, was less than 35 percent of Q_{ref} indicating an accumulation of high loss fluid in that area. In contrast, along the top and bottom walls of the duct low loss fluid was confined to thin viscous boundary layers.

4.2.3.2 Boundary Layer Measurements

As noted above in Fig. 3-12, boundary layer traverses were made at ten locations around the periphery in the exit plane of the AR630 duct. Two traverses were made in the spanwise direction along the semi-major axes ($z/H = 0$) and eight traverses were made in the transverse direction ($y/S = -.50, 0, .50, .75$). The eight transverse total pressure traverses are plotted in Fig. 4-22a. The boundary layers along the upper and lower walls of the duct in the exit plane were thinnest near the semi-minor axes ($\delta_{995}/H \approx 0.35$ at $y/S = 0$) and increased in thickness at locations nearer the sidewalls ($\delta_{995}/H \approx 0.45$ at $y/S = \pm 0.5$ and $\delta_{995}/H \approx 0.55$ at $y/S = \pm 0.75$).

Spanwise pitot pressure profiles measured along the semi-major axis at traverse locations 1 and 2 are plotted in Fig. 4-22b. The profiles are essentially identical which indicates excellent flow symmetry in the duct. The S-shaped profile at location 2 resulted from traversing through the local total pressure minimum at $y/S = 0.9$, $z/H = 0$ which was delineated above in Fig. 4-21b by the kielhead total pressure survey. The S-shaped profile at location 1 suggests that an identical flow pattern exists along the opposite sidewall of the exit duct.

The surveys were integrated to determine the boundary layer integral parameters in the same manner as the AR310 surveys to account for normal pressure gradients (see Section 4.1.3.2). The results in terms of the displacement and momentum thicknesses normalized by the half-height and the shape factors are given in Fig. 4-22c. For the transverse surveys the displacement thicknesses are considerably thicker than the AR310 profiles ranging from 4 to 6 percent of the half-height. The corresponding shape factors range from 1.27-1.35 which are reasonable values for turbulent boundary layers. For the spanwise surveys the displacement thicknesses are very large, over 40 percent of the half-height, and the shape factors are unusually large at 1.6-1.7. This is not unexpected due to the unconventional profile shapes shown in Fig. 4-22b.

The boundary layer profiles obtained at locations 1, 2, 4, and 8 along the duct semi-major and semi-minor axes are plotted in law-of-the-wall coordinates in Fig. 4-23. The transverse profiles at location 4 and 8 had similar near equilibrum boundary layer shapes. Each has an extended log-linear region and a well defined wake region. The main discriminator between the two profiles is the wall skin friction which was calculated from U , the friction velocity chosen to fit the data to the log-linear region. Using Eq. (4.2) C_f was calculated to be 0.00461 and 0.00405 at locations 4 and 8, respectively. Profiles at locations 1 and 2 contained a small log-linear region to permit the determination of C_f but the shapes were definitely non-equilibrium.

4.2.4 Exit Plane Laser Velocimeter Measurements

As shown in Fig. 3-11, three-component laser velocimeter measurements were made a 150 of the 154 total pressure measurement locations in the exit plane of the AR630 duct. At the remaining four total pressure measurement locations optical access restrictions permitted only axial velocity components to be measured at two locations, as indicated in the figure. The velocity measurements normalized by U_{ref} are given in Table IIIb.

4.2.4.1 Mean Velocity Measurements

LV measurements of the axial velocity distribution in the exit plane of the AR630 duct are shown in Fig. 4-24a. The 3-D plot was constructed from LV data obtained at 110 measurement locations ($0 \leq y/S \leq 0.90$) in the exit half-plane containing the denser measurement grid. Three features of the flow apparent in Fig. 4-24a are the flat velocity profile in the core flow, the thin top and bottom wall boundary layers, and the accumulation of low velocity fluid along the duct semi-major axis near the side walls.

A two-dimensional representation of the axial velocity data shown in Fig. 4-24a supplemented with additional data points obtained at $y/S = 0.95$ is shown in Fig. 4-24b containing contours of constant U/U_{ref}. The axial velocity contours are similar to the total pressure contours in the AR630 exit plane plotted in Fig. 4-21b. Each set of data shows that the flow in the exit duct is uniform and nearly inviscid except for an accumulation of low momentum fluid along the semi-major axis near the sidewall where $Y < 0.6\ U_{ref}$.

The cross-flow velocity vectors measured in the AR630 exit plane are plotted in Fig. 4-25. The four features of the cross-flow velocity distribution in the exit plane of the AR310 duct noted above are also apparent, although to differing degrees, in the cross-flow patterns in the AR630 exit plane. First, the cross-flow velocities are small. They are less than 10 percent of U_{ref} at all locations and are typically on the order of $0.03\ U_{ref}$. Second, the cross flows show a symmetrical flow pattern in the exit duct. Third, the predominant direction of the cross flows is outward but they are much smaller than the outward flows measured in the AR310 exit plane. This low outward flow velocity indicates that the adjustment in the core flow toward a uniform velocity profile has been essentially completed within the AR630 transition section. As shown in Figs. 4-24a and 4-10a the axial velocity has a much flatter distribution in the AR630 exit plane than in the AR310 exit plane.

A major difference between the cross flows in the AR310 and AR630 exit planes occurs near the duct sidewalls. In the AR630 duct a well defined axial vortex pair in the duct corner induces fluid from the sidewall boundary layer to flow inward along the major axis resulting in the accumulation of low momentum fluid in the vicinity of $y/S = 0.9$, $z/H = 0$ which was apparent in the measured total pressure and axial velocity distributions. The cross-flow pattern near the sidewalls of the AR630 duct is similar to the pattern of secondary flows generated in the corners of straight rectangular ducts (Fig. 2-2).

The cross-flow velocity components are combined with the axial velocity components to determine the kinetic energy distribution in the AR630 exit plane. Contours of constant values of kinetic energy are plotted in Fig. 4-26. Because of the low magnitude of the cross-flow velocities, the kinetic energy contours are quite similar to the axial velocity contours in Fig. 4-24b.

4.2.4.2 <u>Calculated Exit Plane Static Pressure Distributions</u>

With the assumption of constant density across the AR630 exit plane, the Bernoulli equation was used to calculate the local static pressure at each of the

150 measurement locations at which total pressure and three-component LV data had been obtained. A three-dimensional plot (Fig. 4-27a) of the calculated static pressure field for the half-plane containing the denser measurement grid shows the static pressure to be uniform across the exit duct except for a region of higher static pressure near the outer 20 percent of the span near the sidewalls. The limited region of higher static pressure along the sidewalls indicates that the potential pressure field created by the transition duct to turn the flow toward the axial direction successfully created a uniform axial flow pattern in the core flow across the exit duct and minimal additional flow turning is required downstream of the exit plane.

Contours of constant static pressure plotted in Fig. 4-27b show that the variation in static pressure across the core flow in the AR630 exit plane is limited to 0.10 Q_{ref}. The static pressure at midspan was 0.15 Q_{ref} lower than the upstream reference static pressure due to core flow acceleration in the transition duct. The flow acceleration was caused by a reduction in the effective cross-sectional area between the inlet and exit planes because of displacement thickness growth through the transition section.

4.2.4.3 Turbulence Measurements

Optical access limitations were more severe in the AR630 exit plane than the AR310 exit plane resulting in a more limited set of non-contaminated cross-flow turbulence measurements (see related disussion in Sec. 4.1.4.3). The cross-flow turbulence data for the AR630 exit plane are listed in Table IIIb. Values which are considered contaminated due to beam tilt are denoted parenthetically with the beam tilt to the right of the measurement.

Axial turbulence measurements, however, were made at each of the 150 LV measurement locations. The distribution of the axial component of turbulence in the AR630 exit plane is shown in Fig. 4-28 in which lines of constant axial turbulence level are plotted. The turbulence level throughout the core flow is on the order of 3 to 4 percent of U_{ref} which is somewhat higher than the 2.4 percent turbulence level measured in the inlet plane. The highest level of axial turbulence, .11U_{ref} occurred at the center of the low momentum region near the sidewall.

4.3 Calculated Axial Vorticity Distribution

The axial vorticity distribution in the exit measurement plane was determined from the transverse velocity data using the equation

$$\Omega_x = \frac{\partial W}{\partial y} - \frac{\partial V}{\partial z} \qquad (4-6)$$

In order to apply Eq. (4-6), linear interpolation was performed on the measurement grid (Figs. 3.9 and 3.11) to obtain a uniform grid distribution across the exit plane (such that the grid spacing in the y and z direction was equal to the smallest actual spacing in the respective direction). For the AR630 duct this was only done on half of the exit plane. Also, along the periphery of the measurement grid, an additional line of grid points was determined by interpolating data between the measured points and the duct boundary where the no-slip condition required $V = W = 0$ (this was done in order to evaluate Ω_x at the periphery). Standard central difference approximations were then applied to the two terms on the right-hand side of Eq. (4-6).

The resulting axial vorticity distributions are presented in Figs. 4-29a and 4-29b where contours of constant axial vorticity are plotted using intervals of 100/sec. In the AR310 duct (Fig. 4-29a) no vortex pattern can be discerned with the 100/sec contour spacing. Except near the edges of the measurement grid the magnitude of the vorticity was less than 100/sec. In the AR630 exit plane the magnitude of the vorticity is also less than 100/sec over the central 80 percent of the duct (Fig. 4-29b). However, a sharply defined vortex pair is delineated near the duct sidewall at $y/S = 0.9$, $z/H = 0.35$ where $\Omega_{xmin} < -400$/sec (clockwise rotation) and at $y/S = 0.9$, $z/H = -0.30$ where $\Omega_{xmax} > 500$/sec (counterclockwise rotation).

As shown above the effect of the vortex pair is to transport low momentum fluid from the duct sidewall boudary layer and deposit it along the duct semi-major axis in the exit plane. The penetration distance of the low momentum fluid from the sidewalls into the core flow along the semi-major axis is directly proportional to the strength of the vortex pair and the residence time of the fluid within the vortex. Thus, the stronger vortex pattern and estimated longer residence time in the longer AR630 duct appears to be responsible for the observed differences in flow distribution near the sidewalls of the two ducts tested.

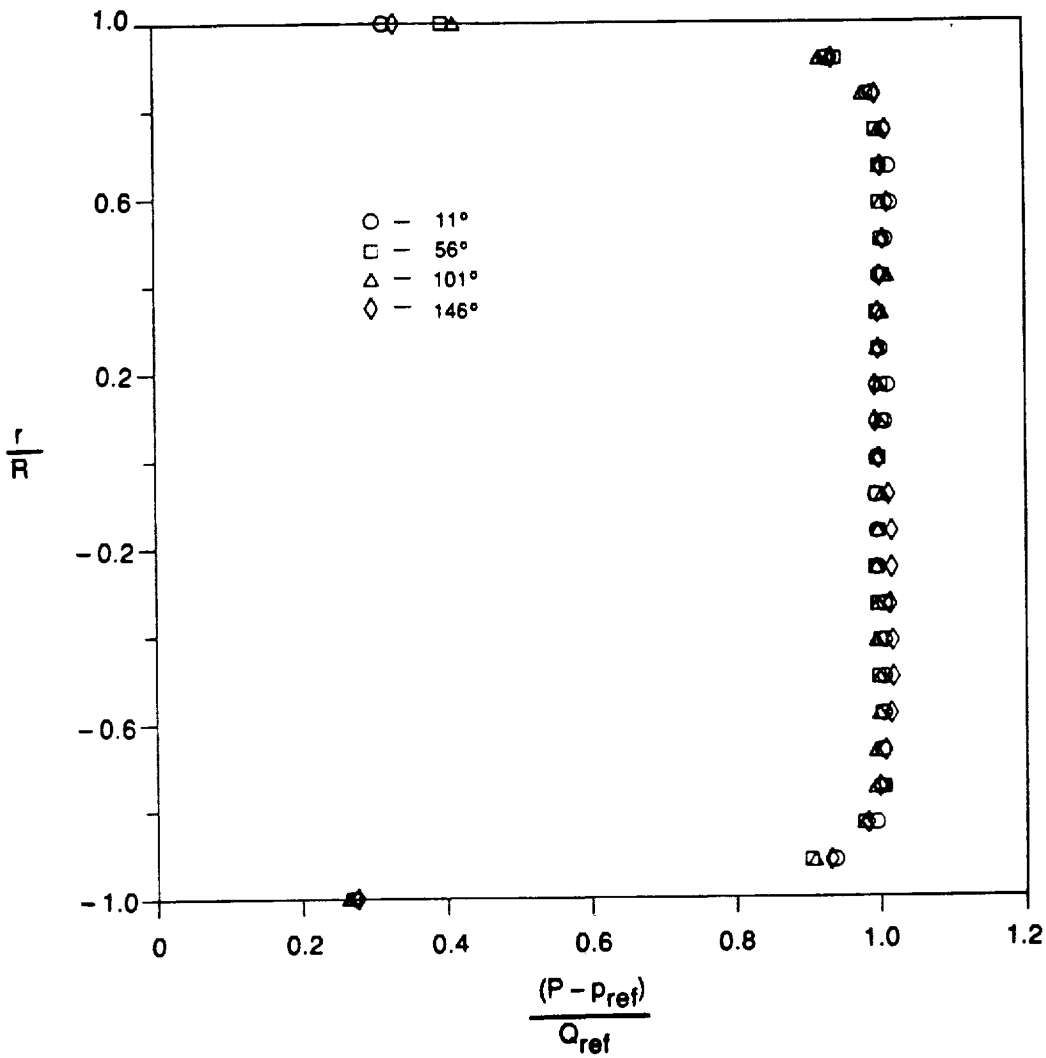

Figure 4-1. — Total Pressure Profiles in AR310 Inlet Plane

87-9-19-8

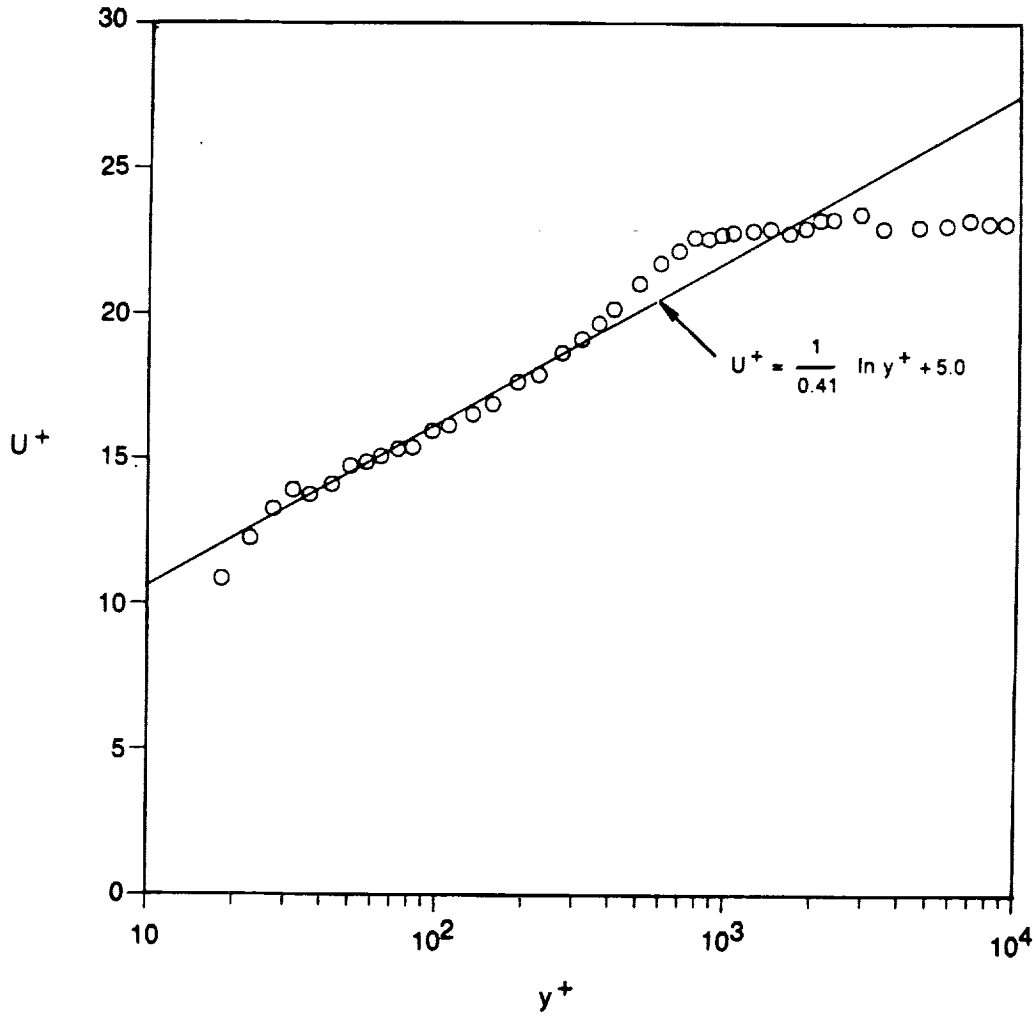

Figure 4-2. — Wall Boundary Layer In AR310 Inlet Plane

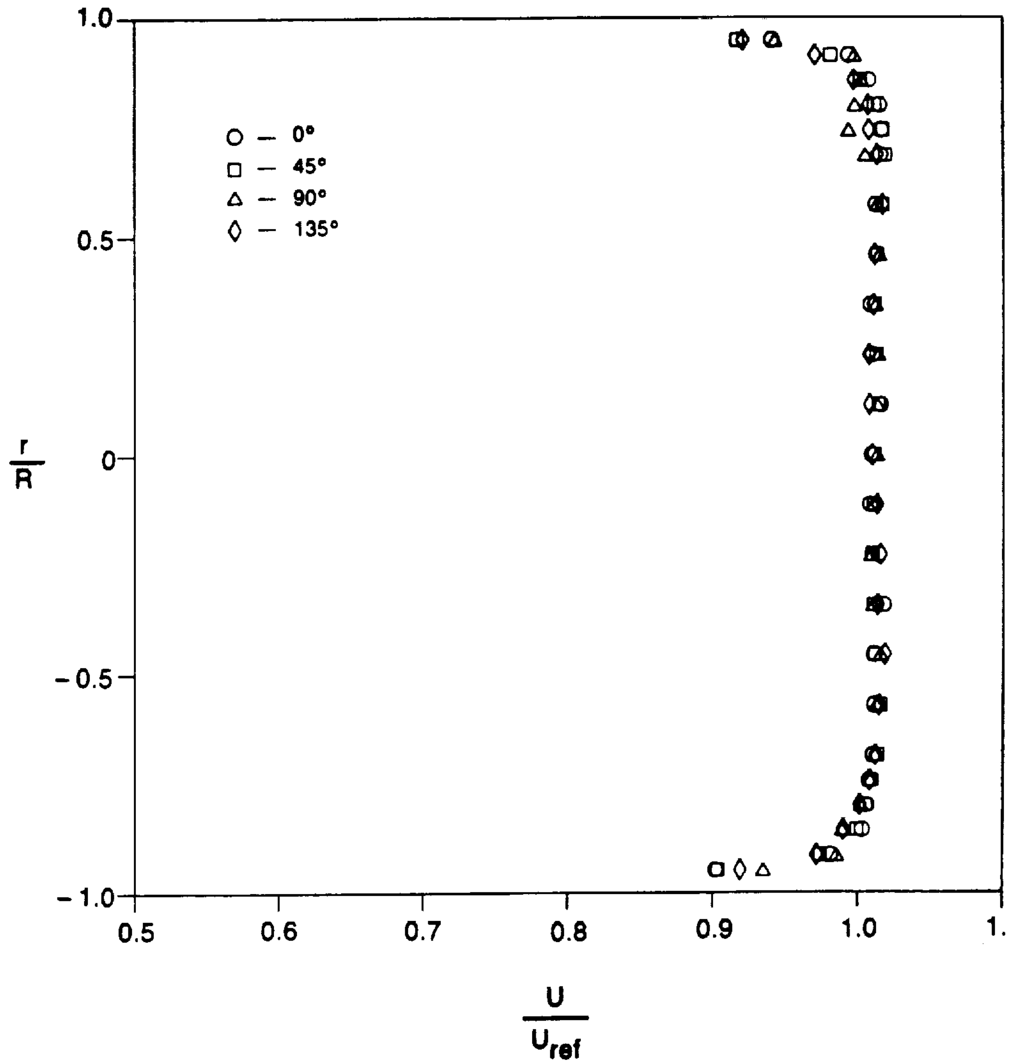

Figure 4.3. — Axial Velocity Profiles in AR310 Inlet Plane

87-9-19-11

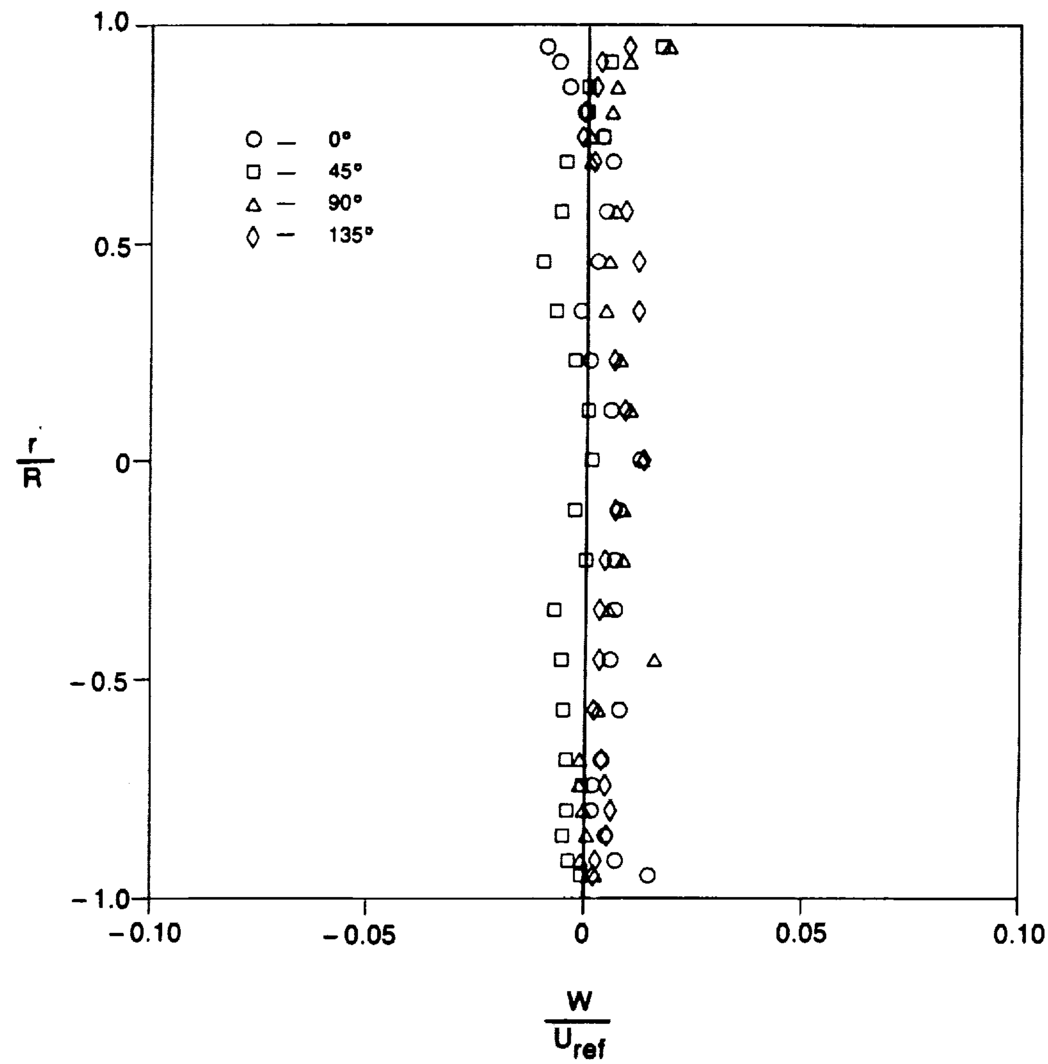

Figure 4-4. — Transverse Velocity Profiles in AR310 Inlet Plane

87-9-19-12

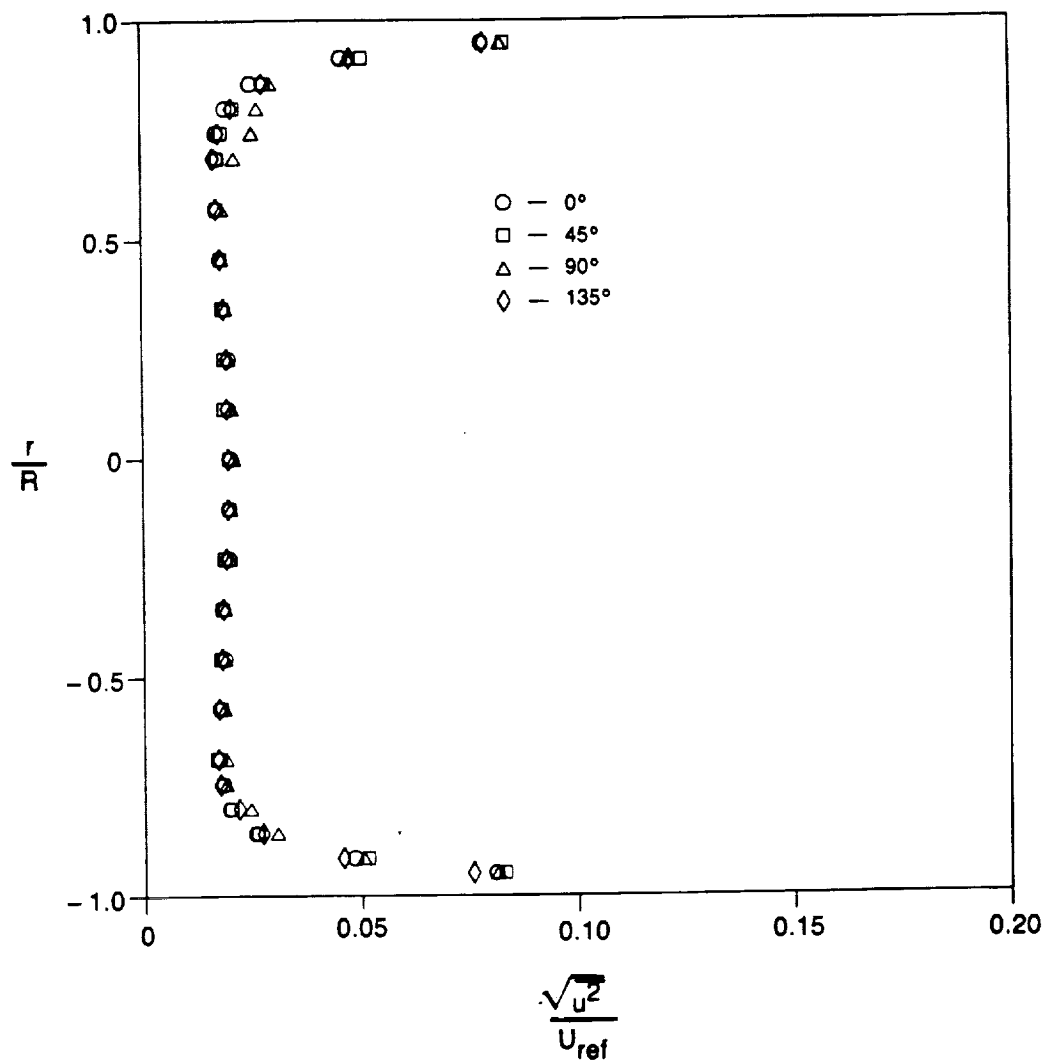

Figure 4-5. — Axial Turbulence Profiles In AR310 Inlet Plane

87-9-19-13

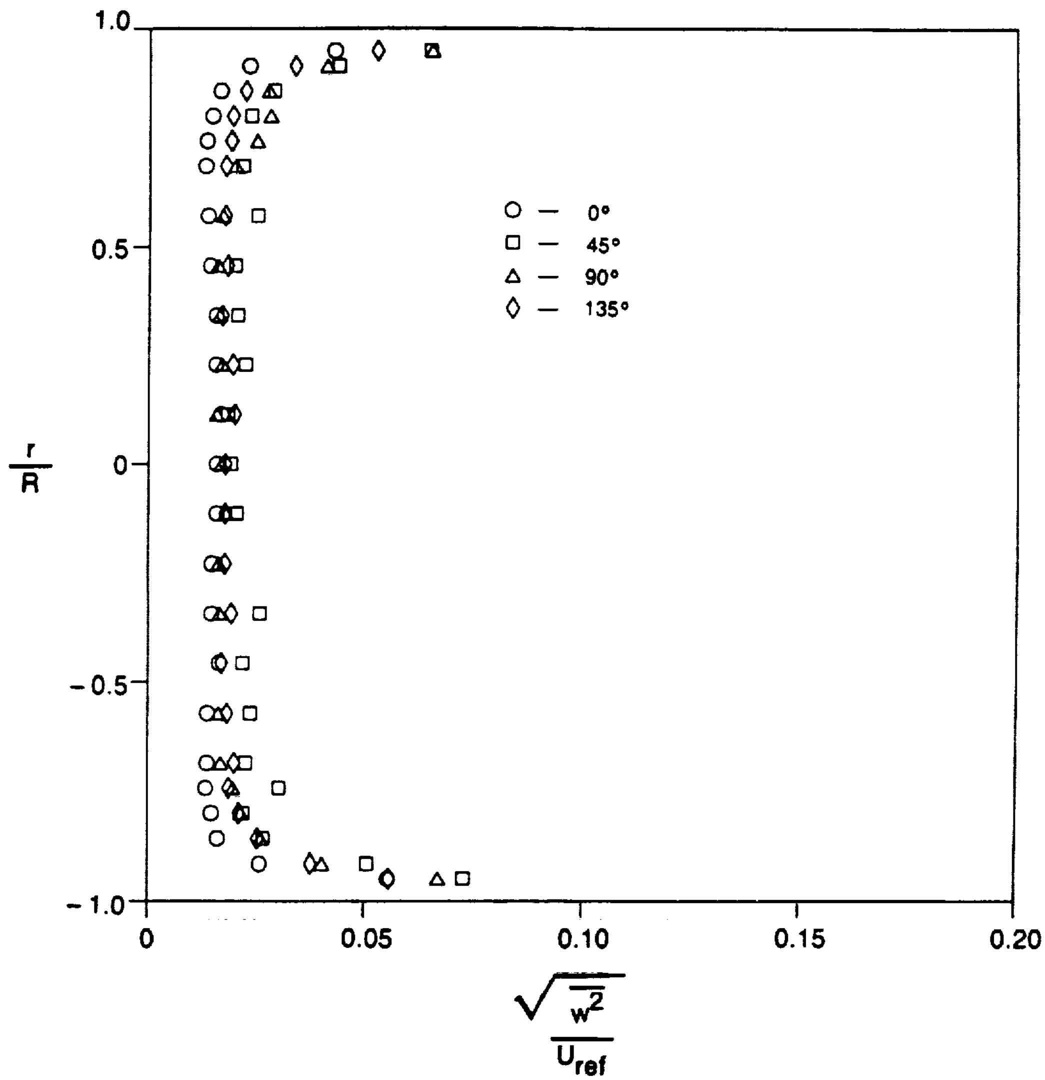

Figure 4-6. — Transverse Turbulence Profiles In AR310 Inlet Plane

87-9-19-14

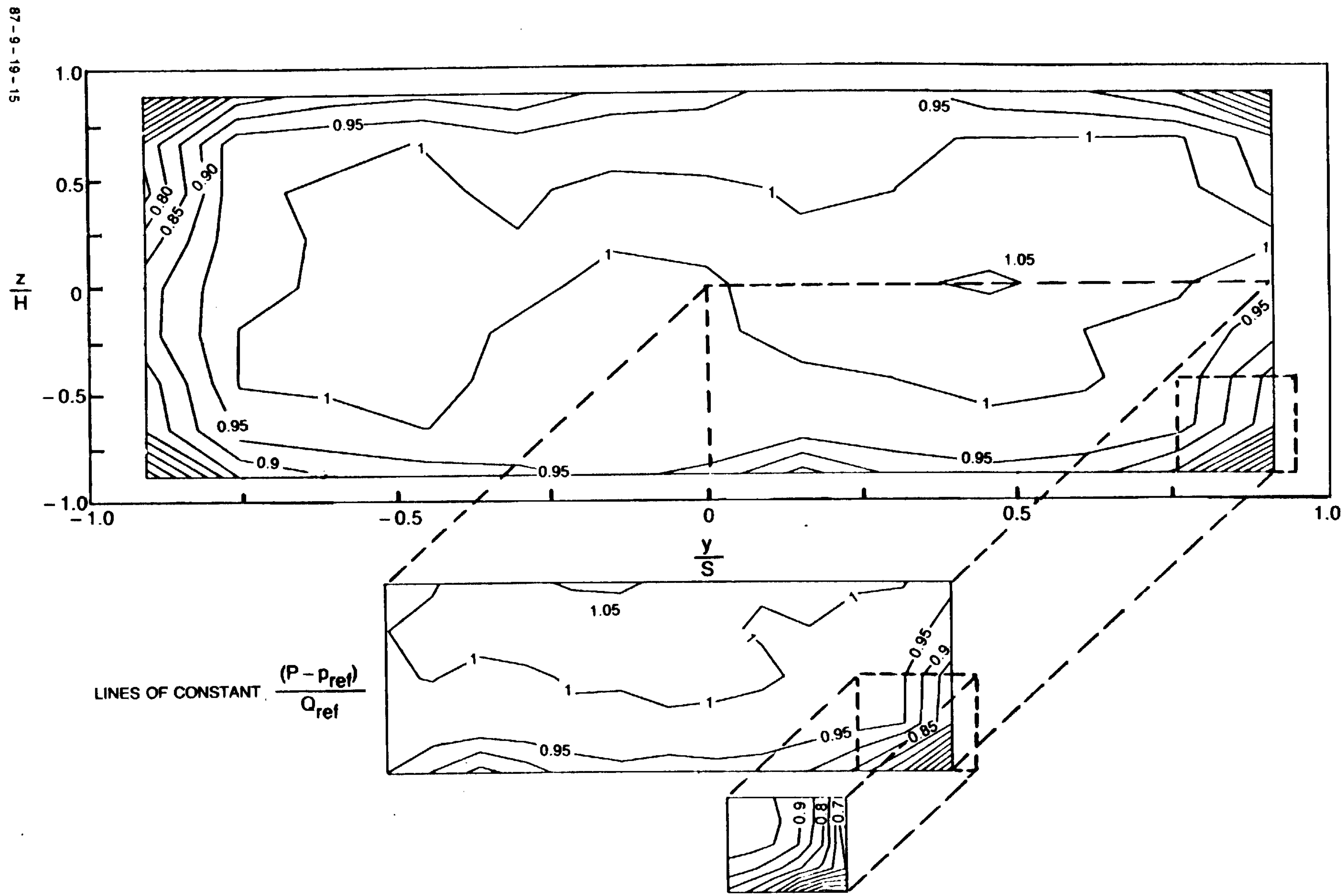

Figure 4-7a. — Total Pressure Distribution In AR310 Exit Plane

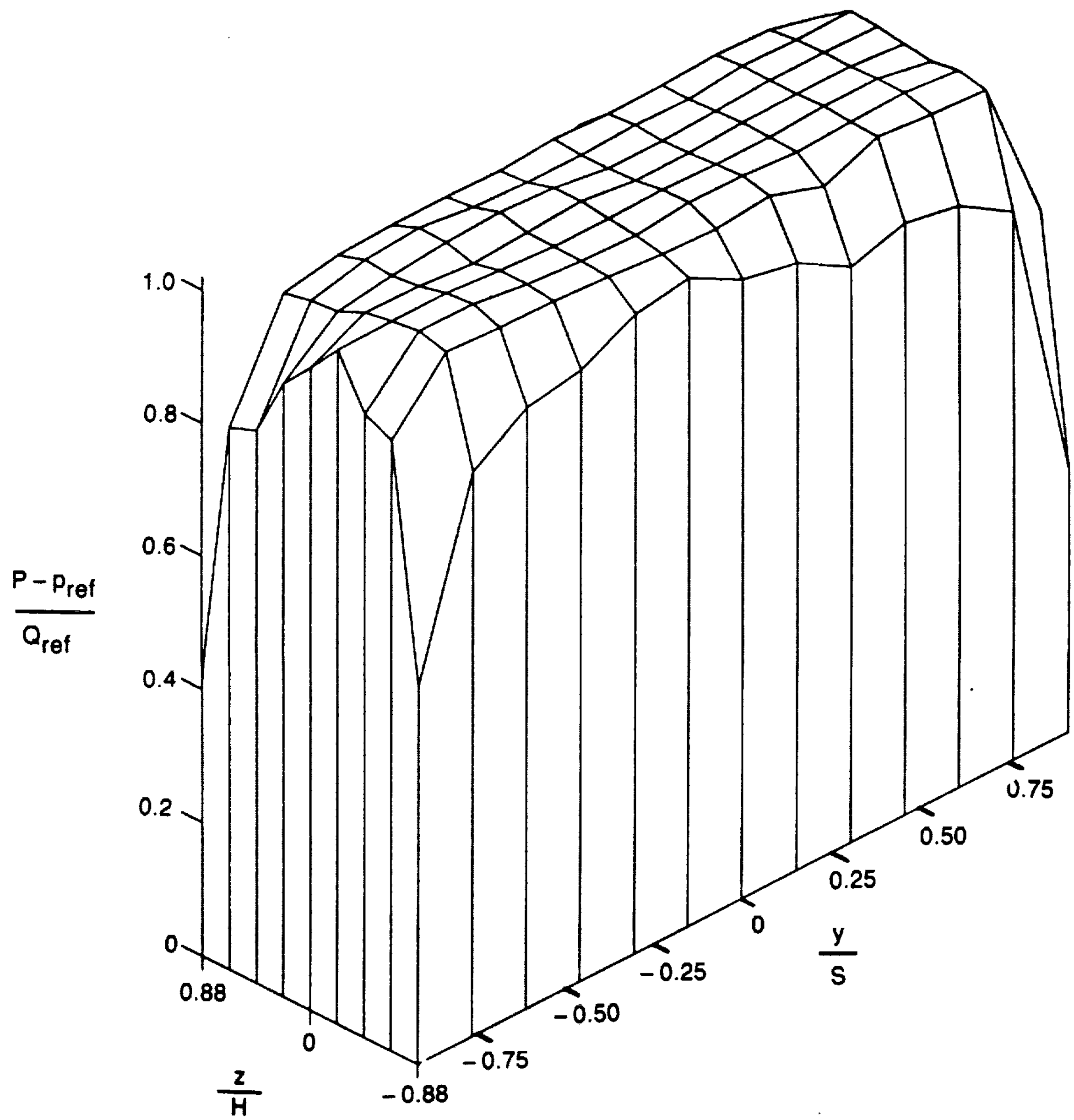

Figure 4-7b. — Total Pressure Distribution In AR310 Exit Plane

87-9-19-16

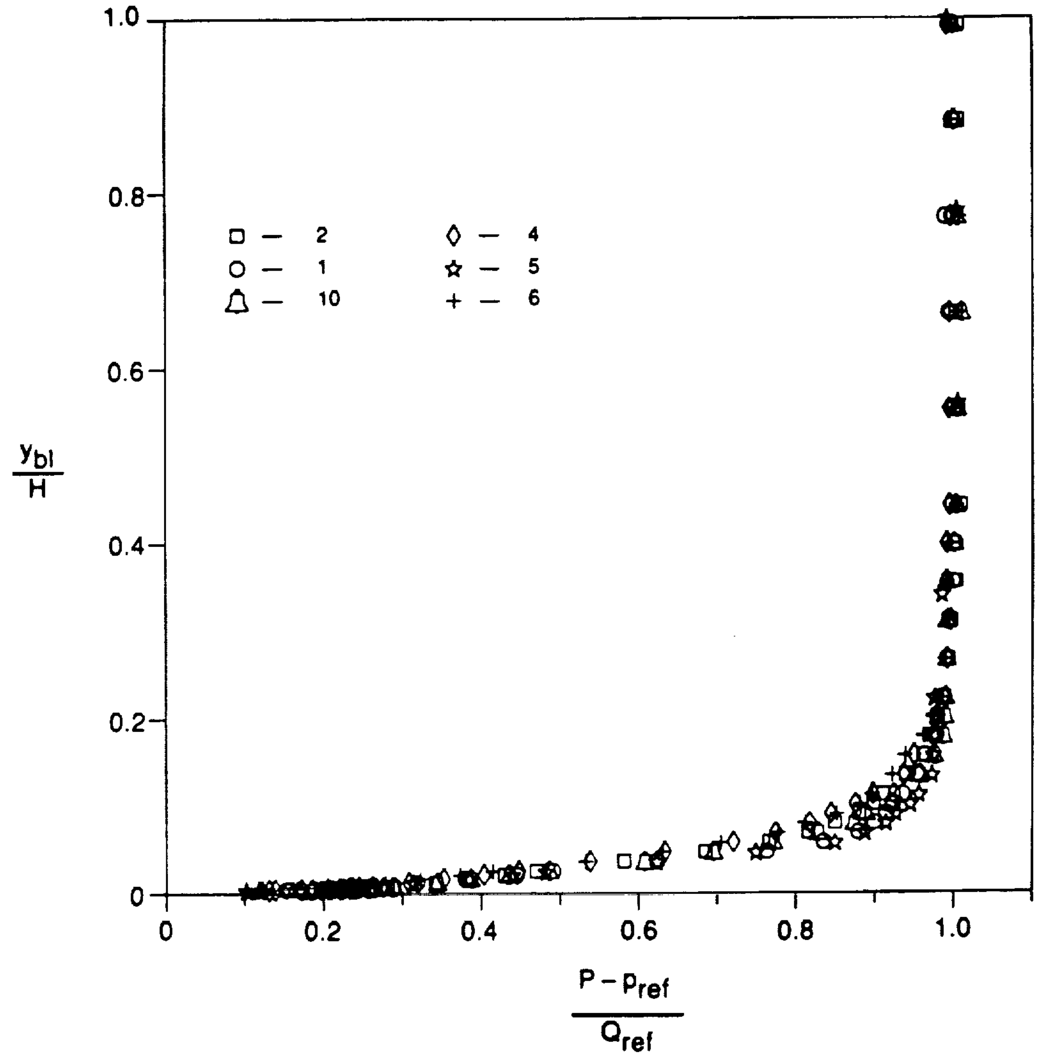

Figure 4-8a. — Transverse Total Pressure Boundary Layers in AR310 Exit Plane

87-9-19-17

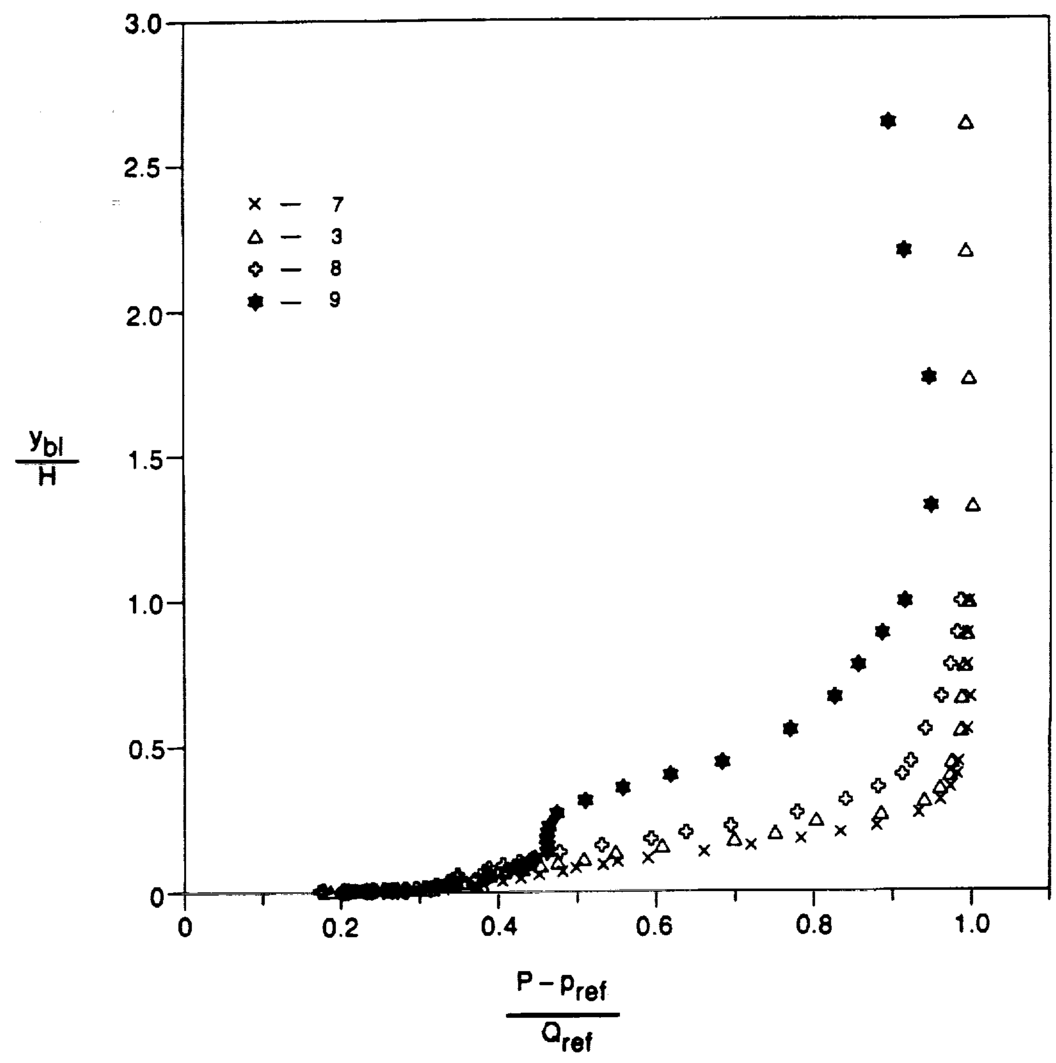

Figure 4-8b. — Spanwise Total Pressure Boundary Layers In AR310 Exit Plane

87-9-19-18

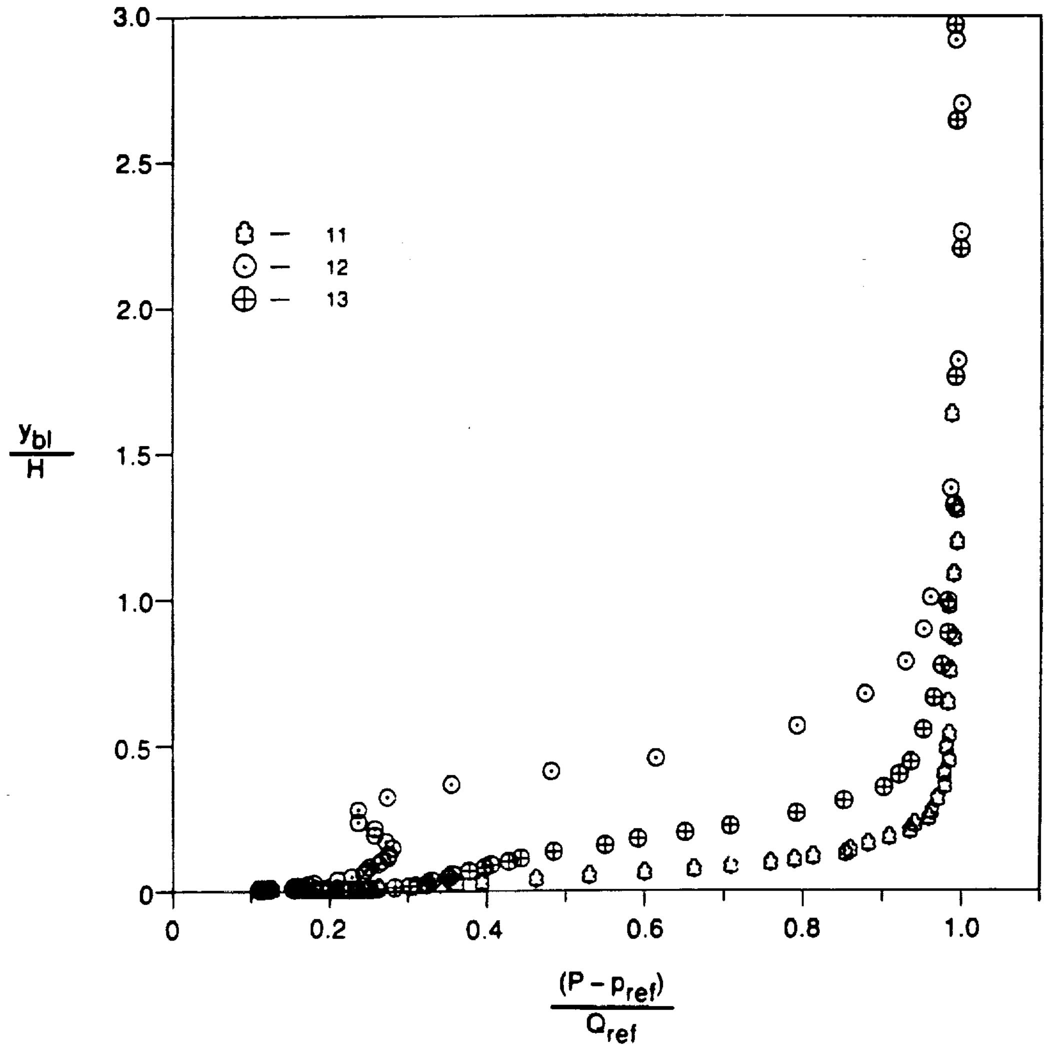

Figure 4-8c. — Corner Total Pressure Boundary Layers In AR310 Exit Plane

87-9-19-19

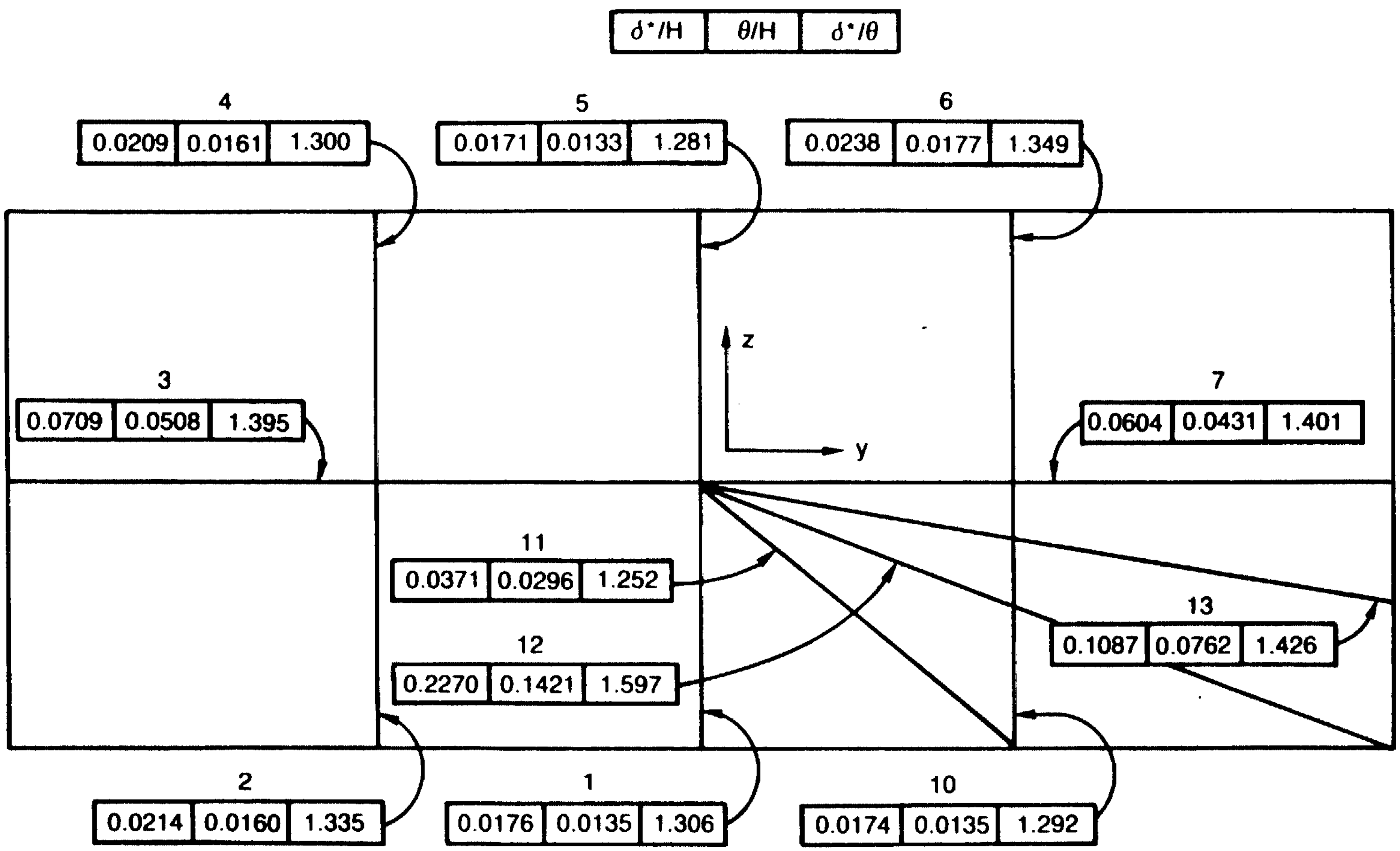

Figure 4-8d. — Boundary Layer Integral Parameters in AR310 Exit Plane

87-9-19-67

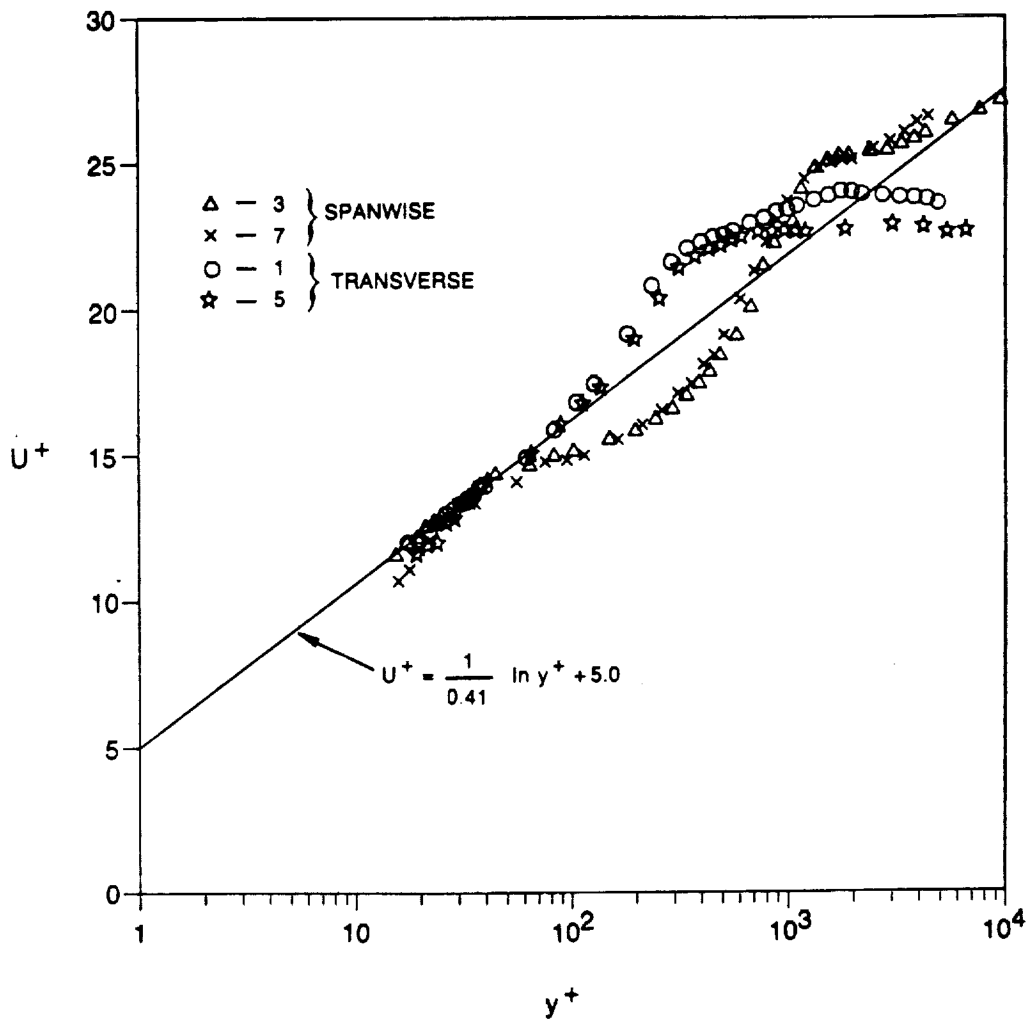

Figure 4-9. — Total Pressure Boundary Layers In AR310 Exit Plane, Law of the Wall Coordinates

87-9-19-20

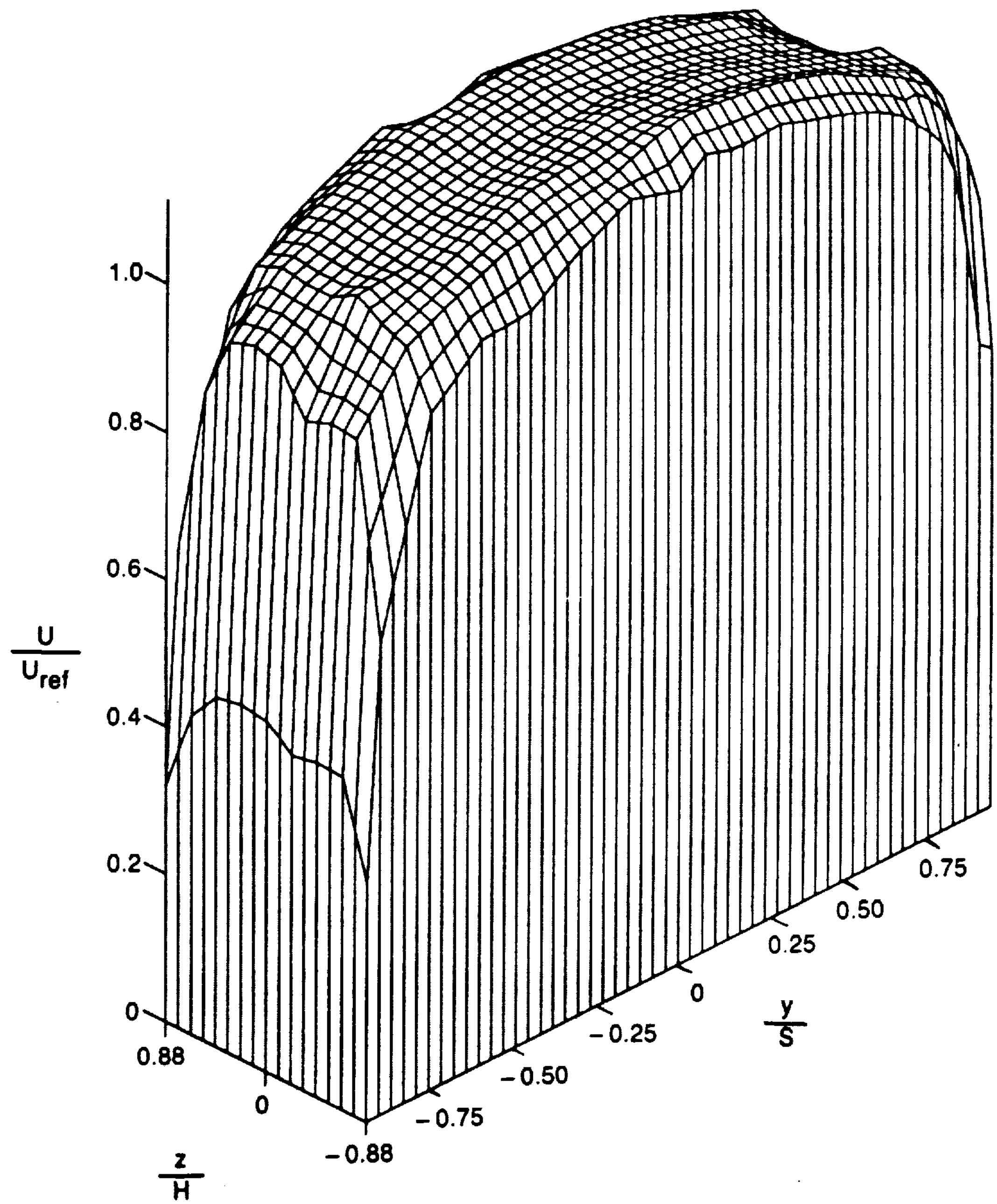

Figure 4-10a. — Axial Velocity Distribution In AR310 Exit Plane

87-9-19-22

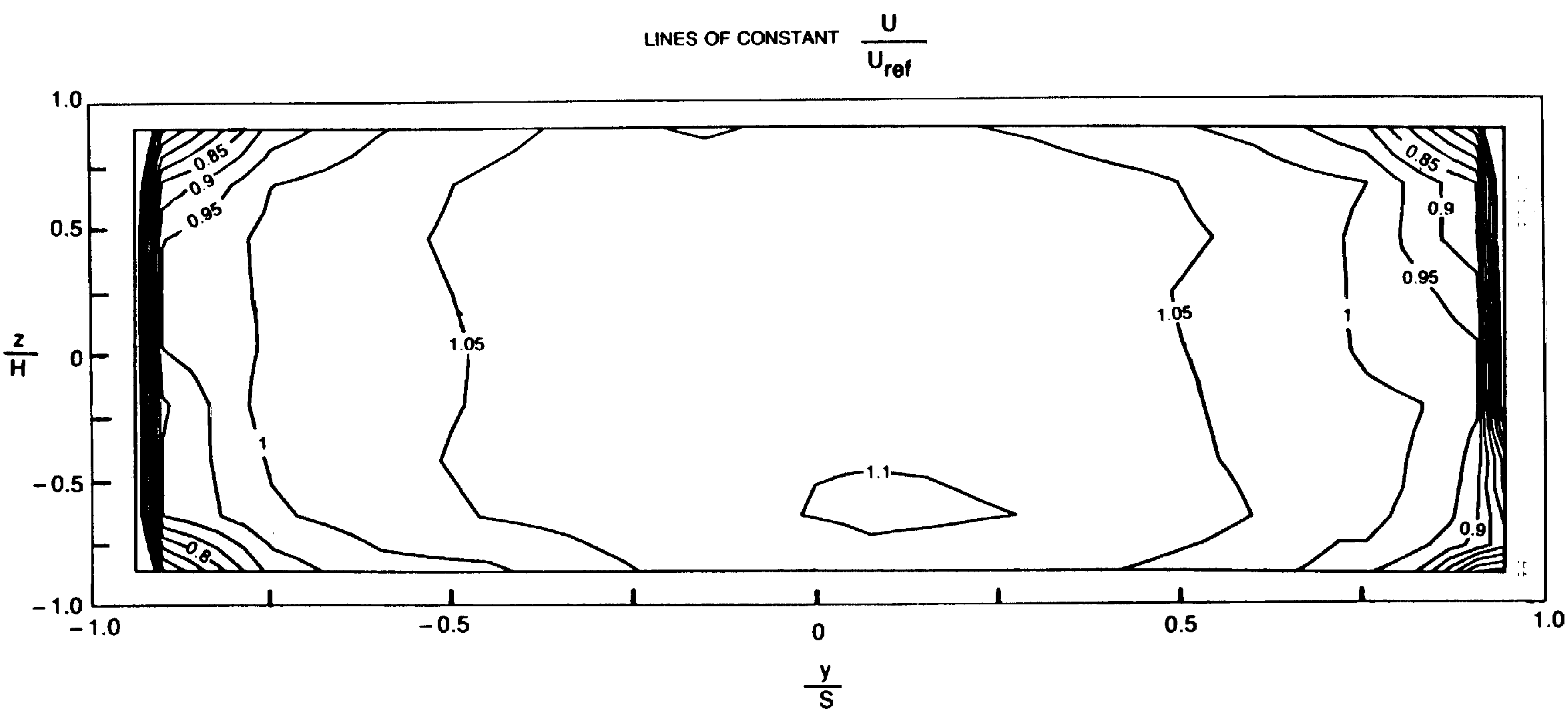

Figure 4-10b. — Axial Velocity Distribution In AR310 Exit Plane

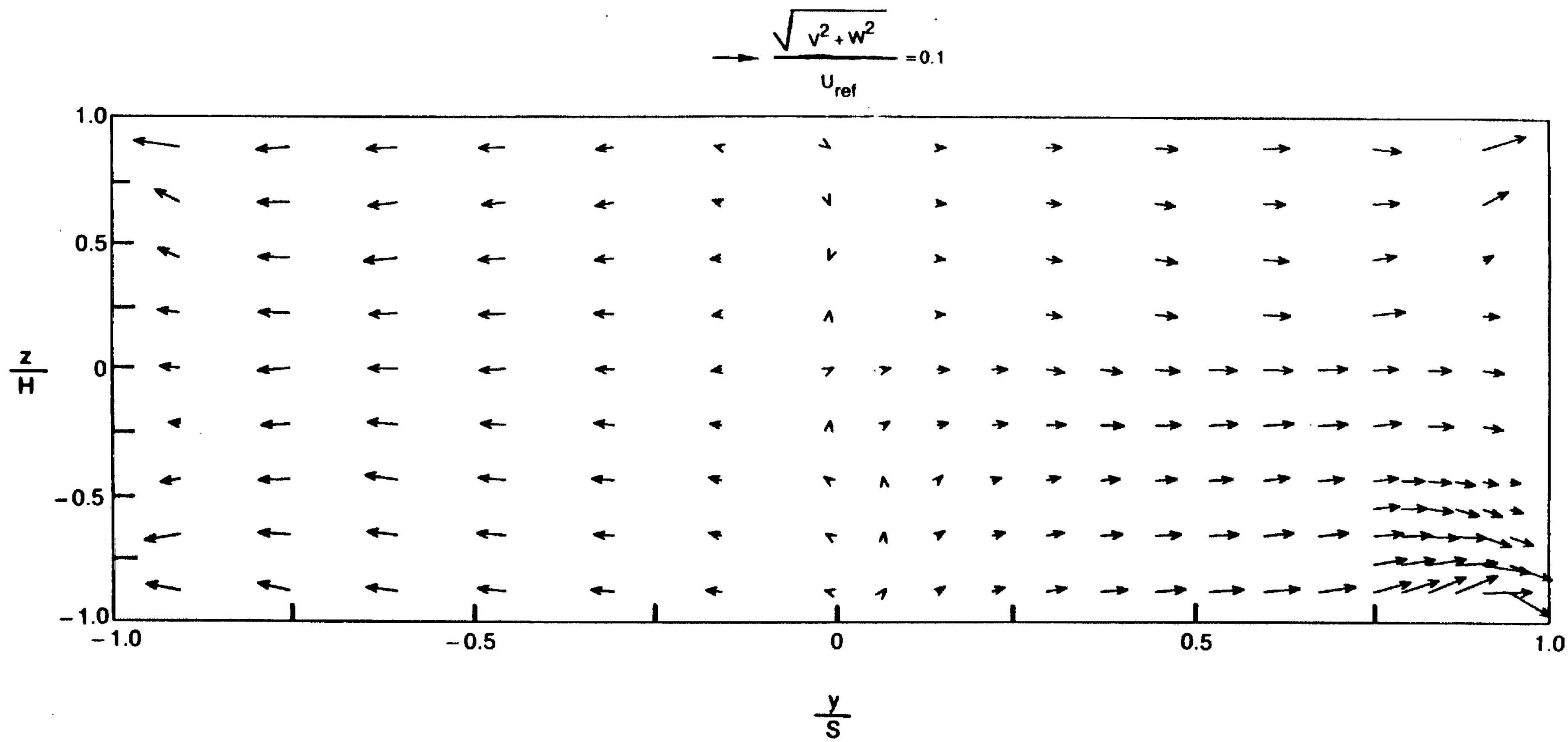

Figure 4-11. — Cross-Flow Velocity Vectors in AR310 Exit Plane

87-9-19-24

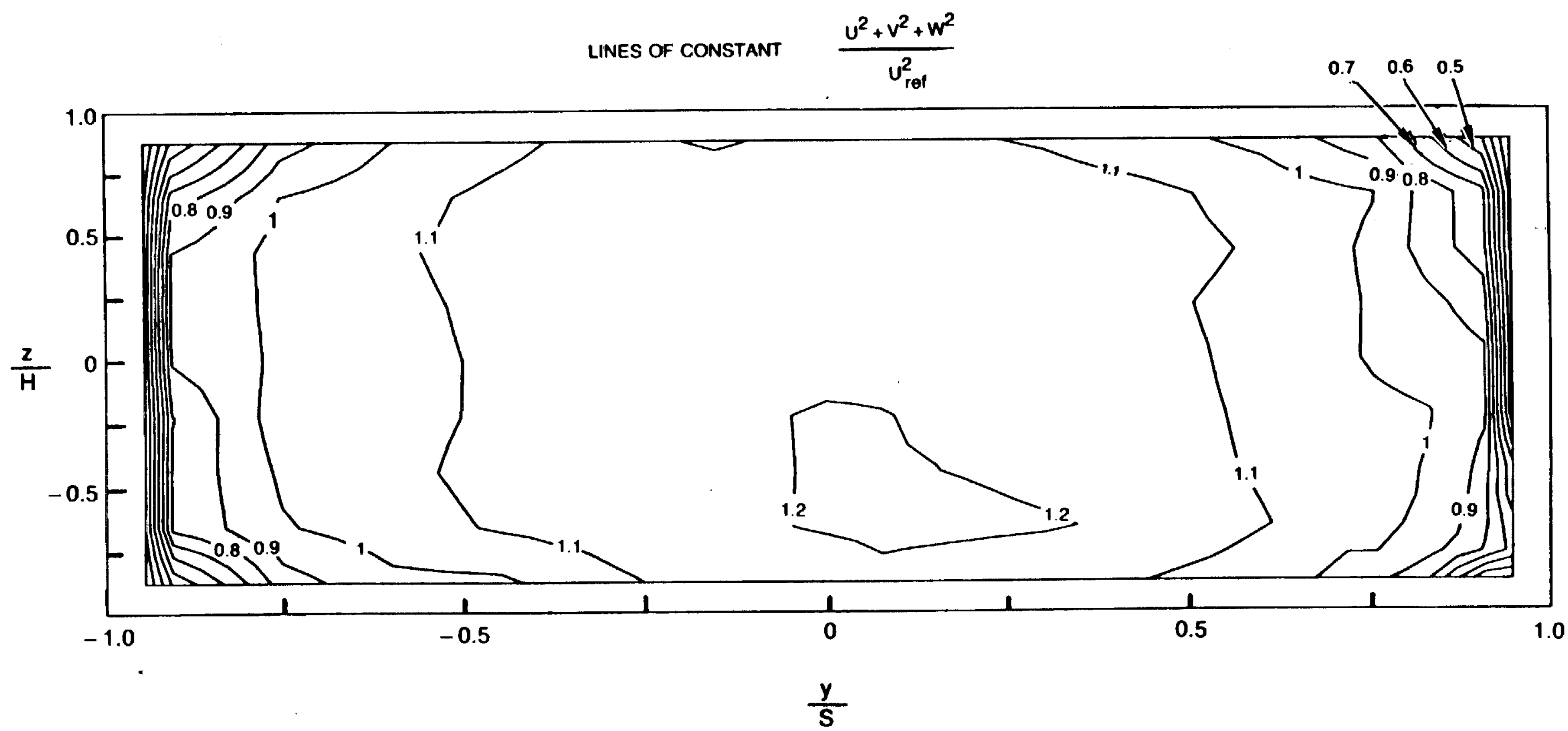

Figure 4-12. — Kinetic Energy Distribution in AR310 Exit Plane

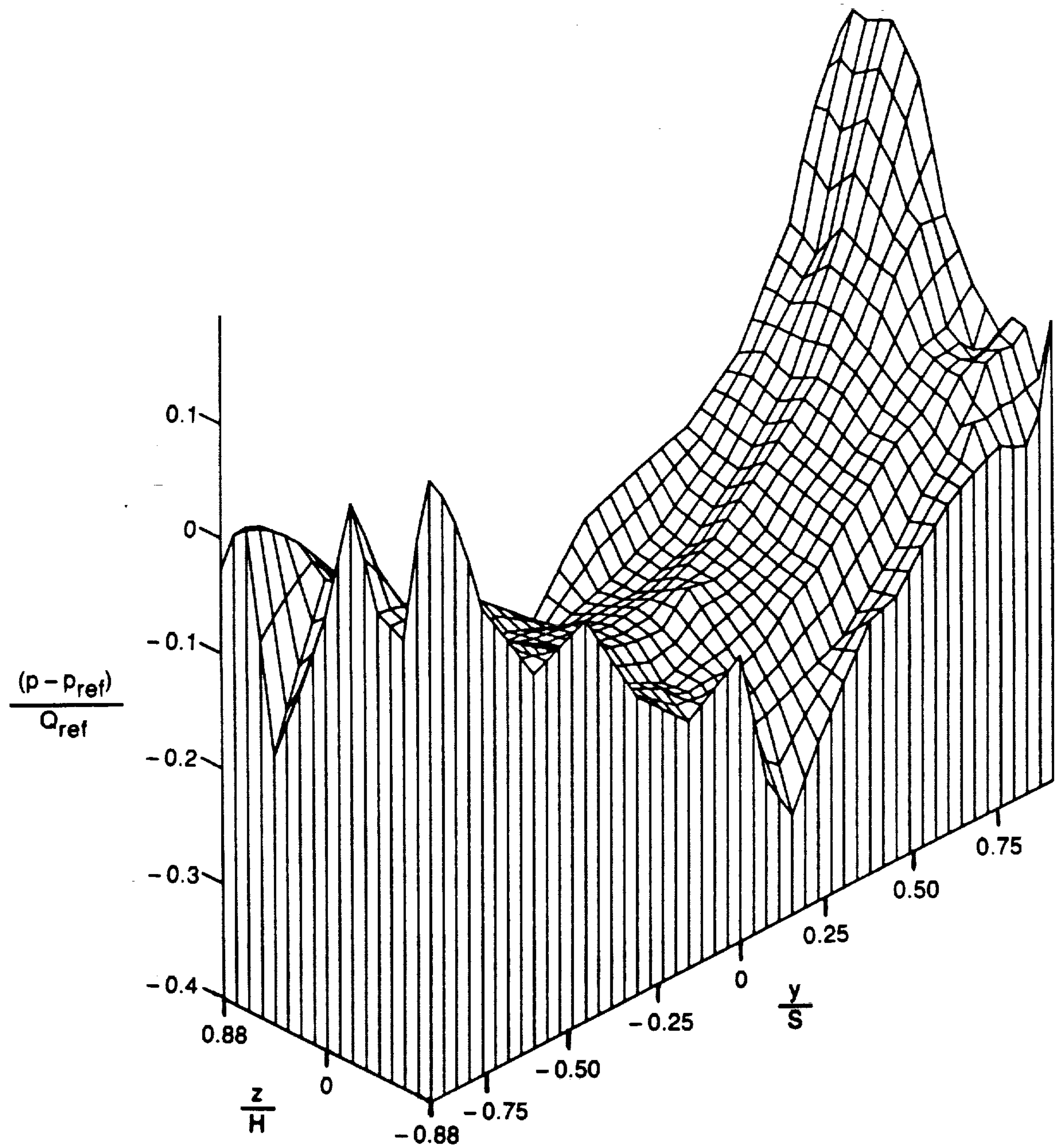

Figure 4-13a. — Static Pressure Distribution In AR310 Exit Plane

87-9-19-26

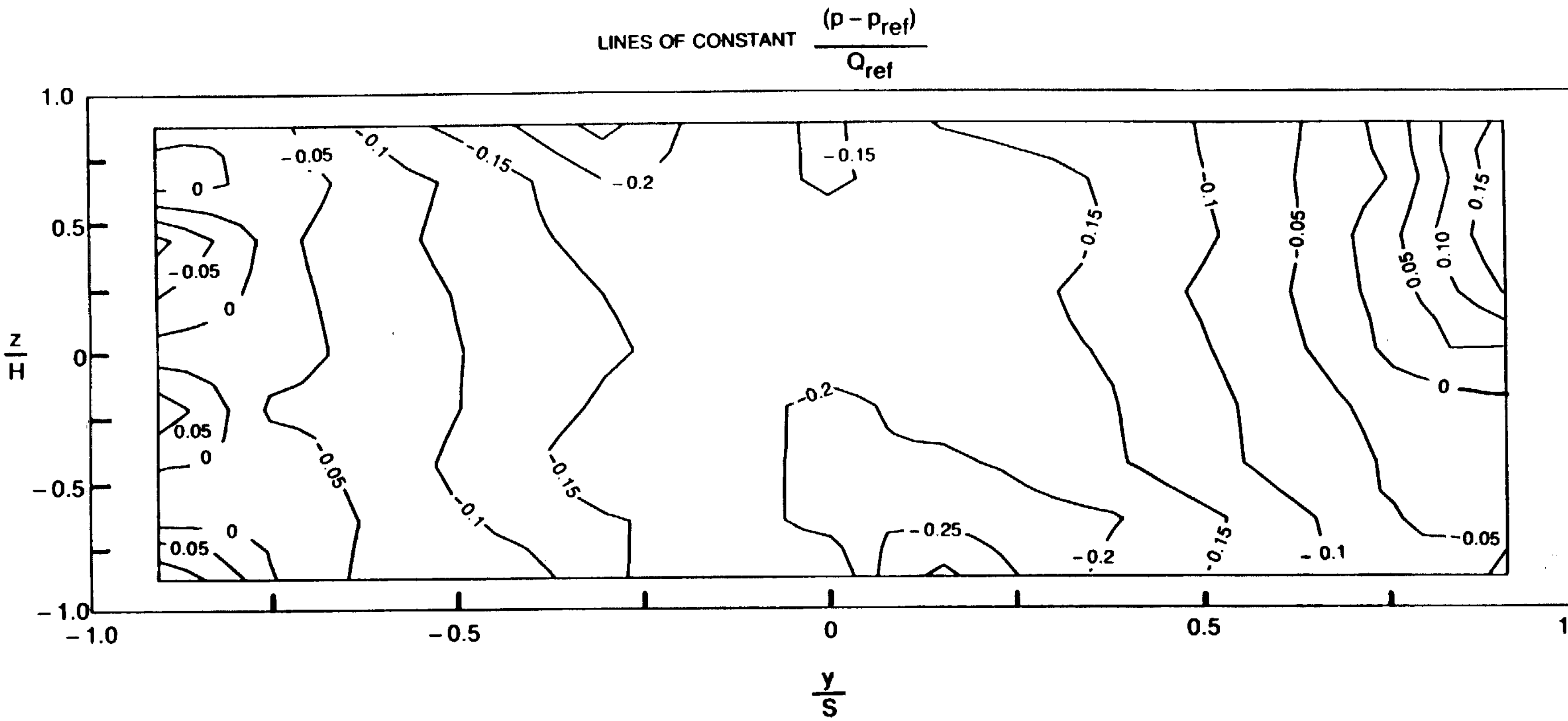

Figure 4-13b. — Static Pressure Distribution In AR310 Exit Plane

87-9-19-25

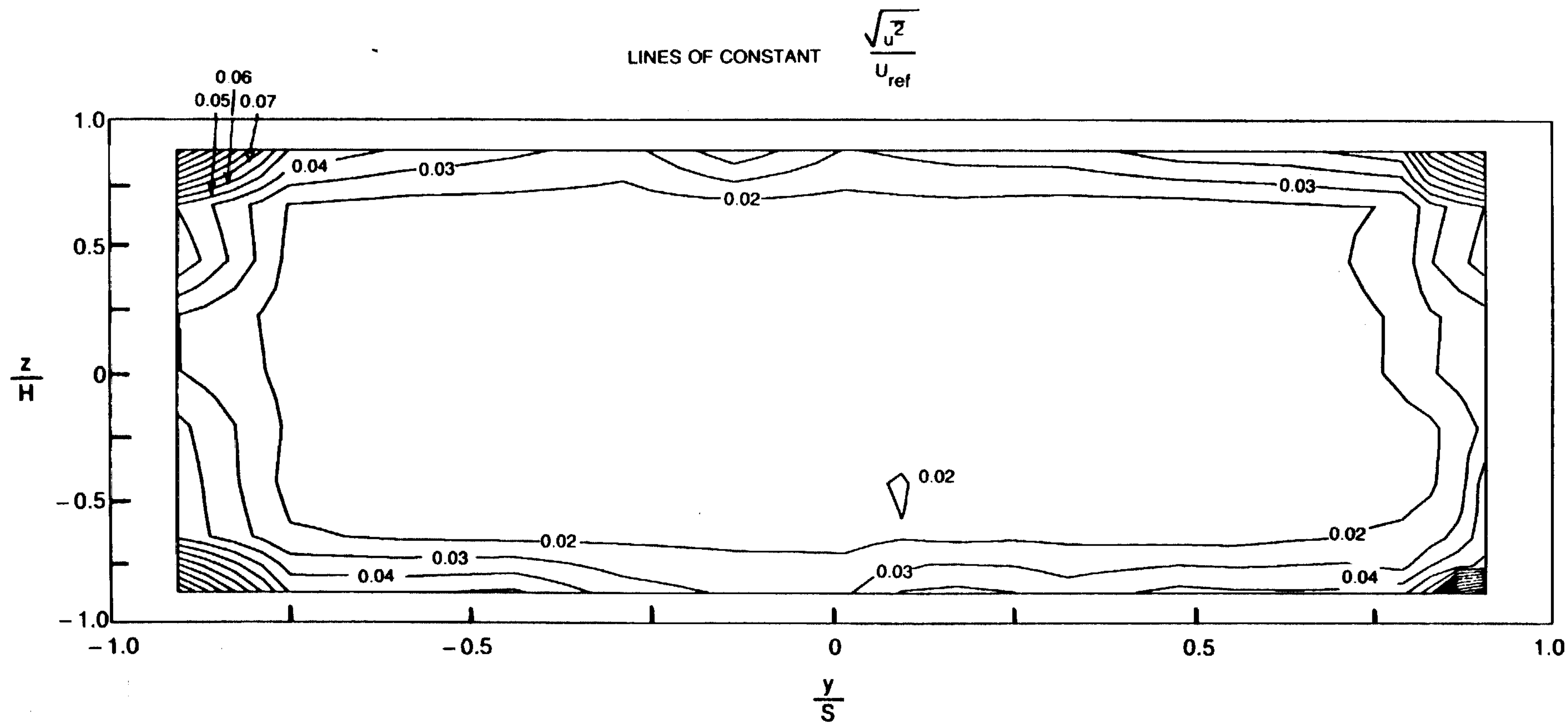

Figure 4-14. — Axial Turbulence Distribution In AR310 Exit Plane

87-9-19-27

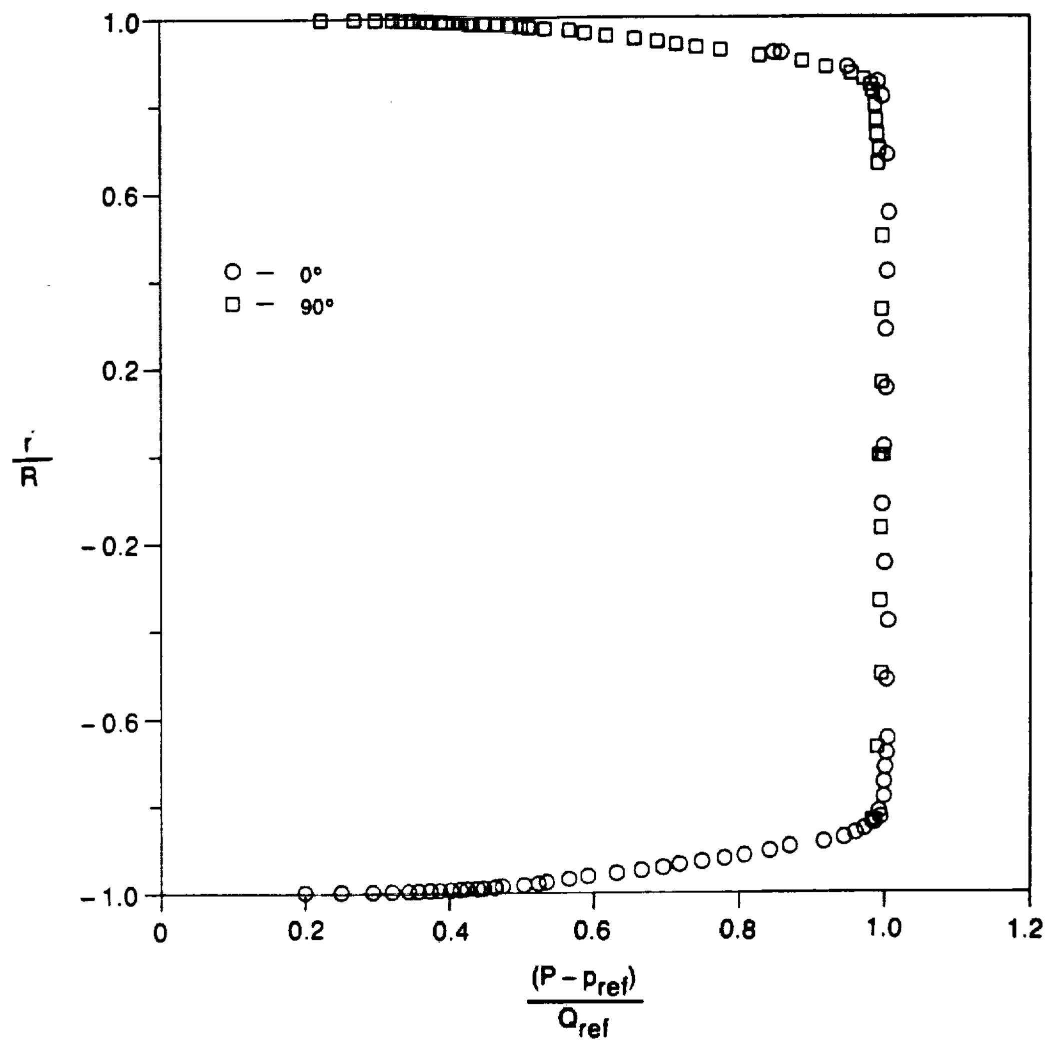

Figure 4-15. — Total Pressure Profiles In AR630 Inlet Plane

87-9-19-28

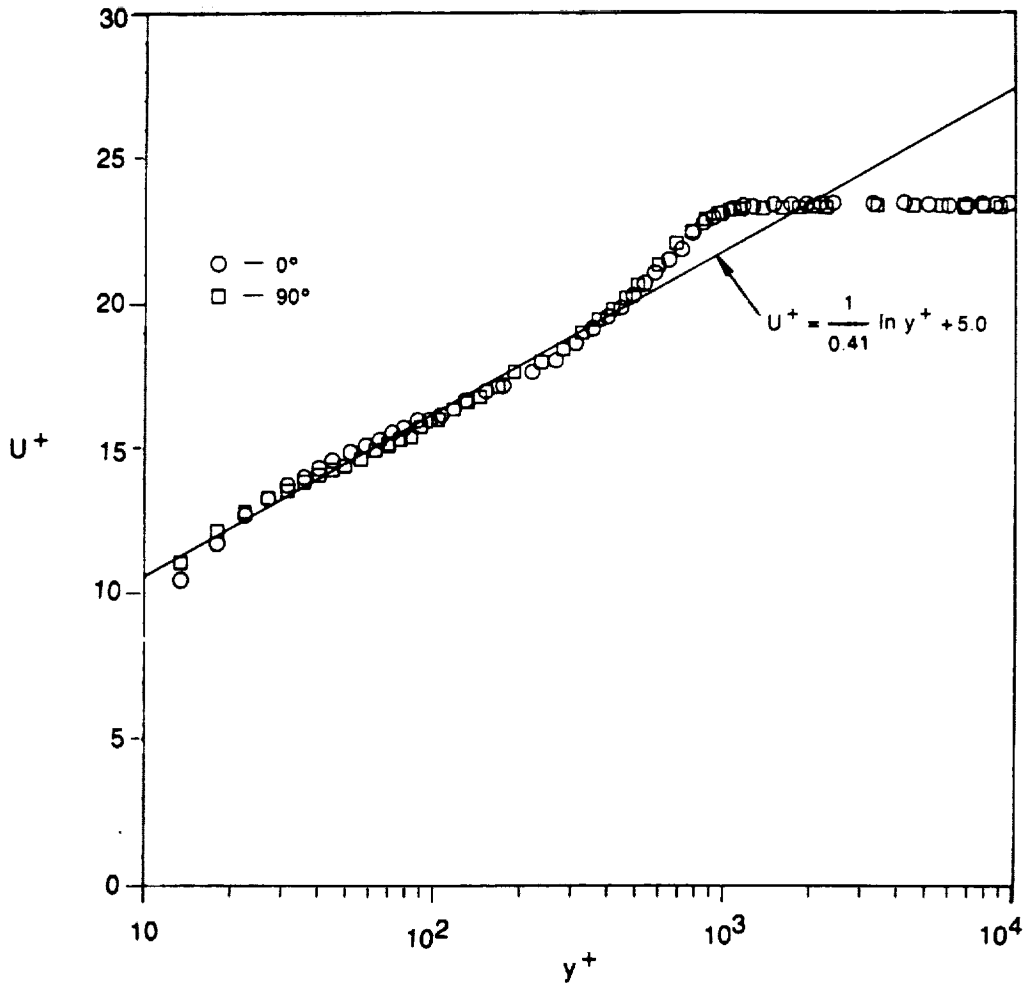

Figure 4-16. — Wall Boundary Layer In AR630 Inlet Plane

87-9-19-29

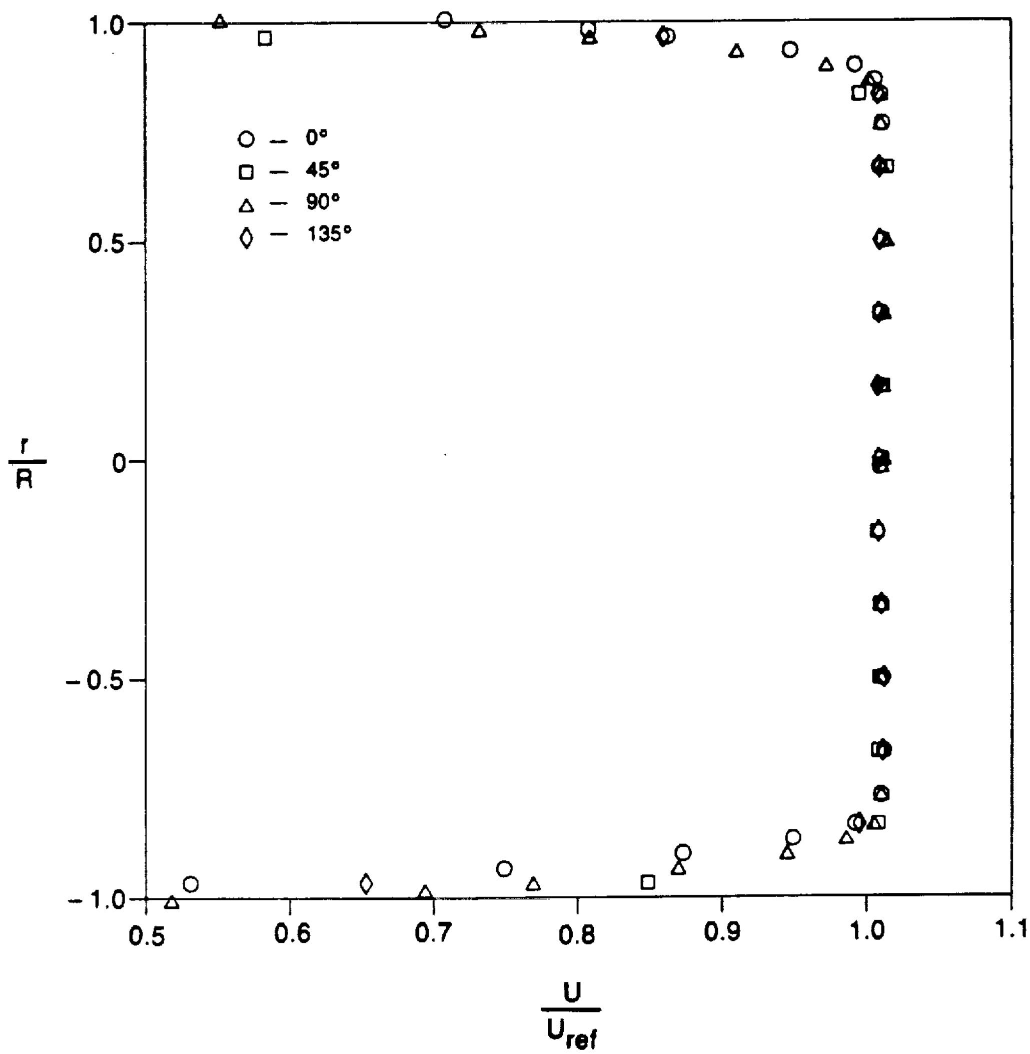

Figure 4-17. — Axial Velocity Profiles in AR630 Inlet Plane

87-9-19-10

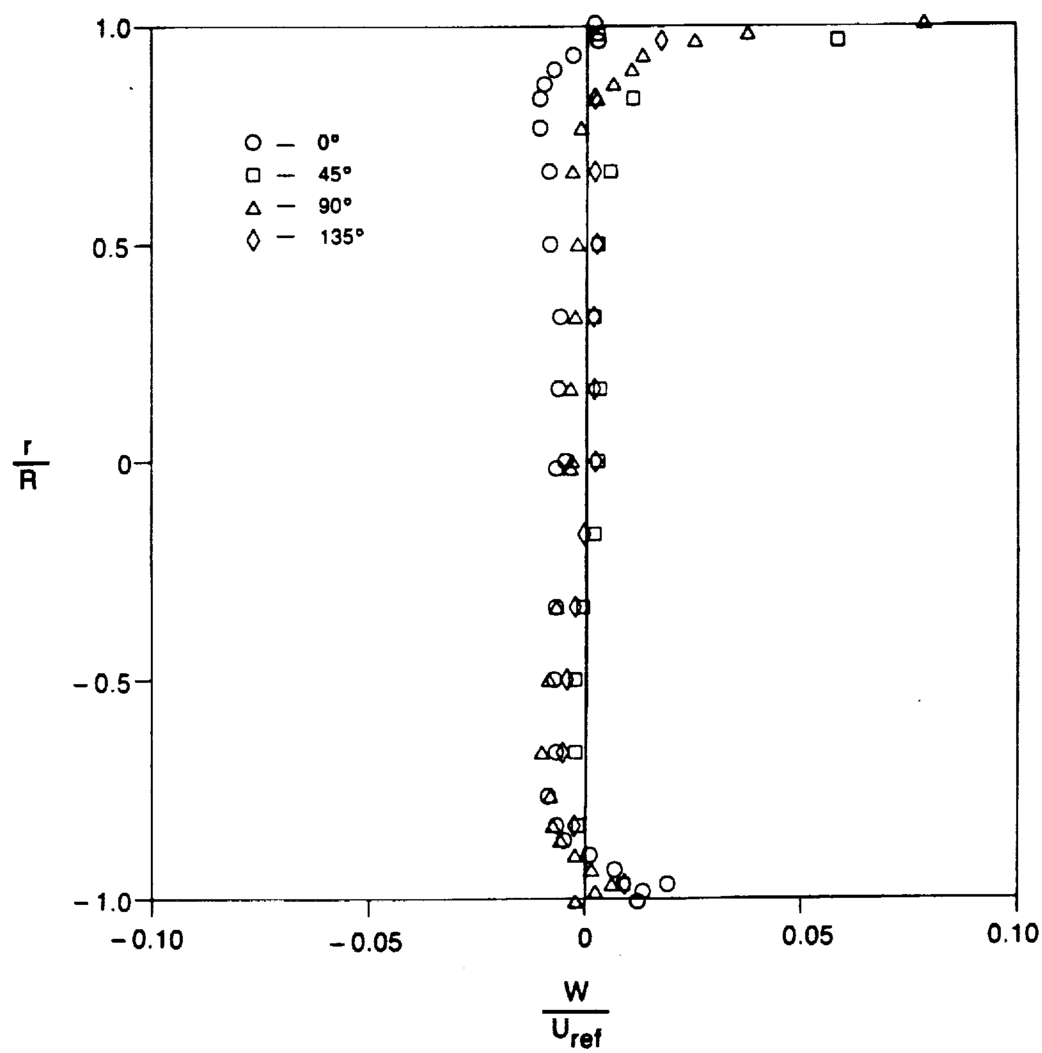

Figure 4-18. — Transverse Velocity Profiles In AR630 Inlet Plane

87-9-19-30

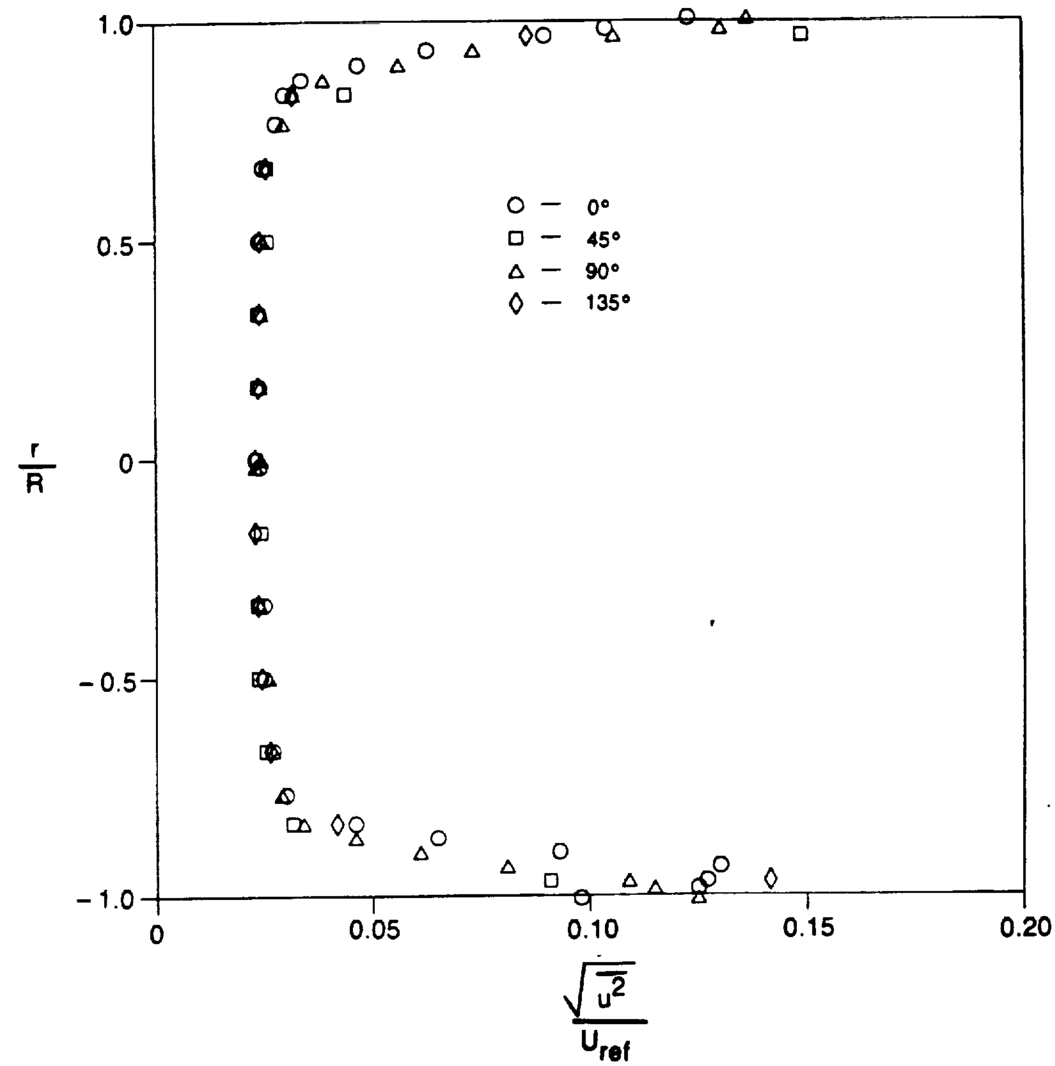

Figure 4-19. — Axial Turbulence Profiles in AR630 Inlet Plane

87-9-19-31

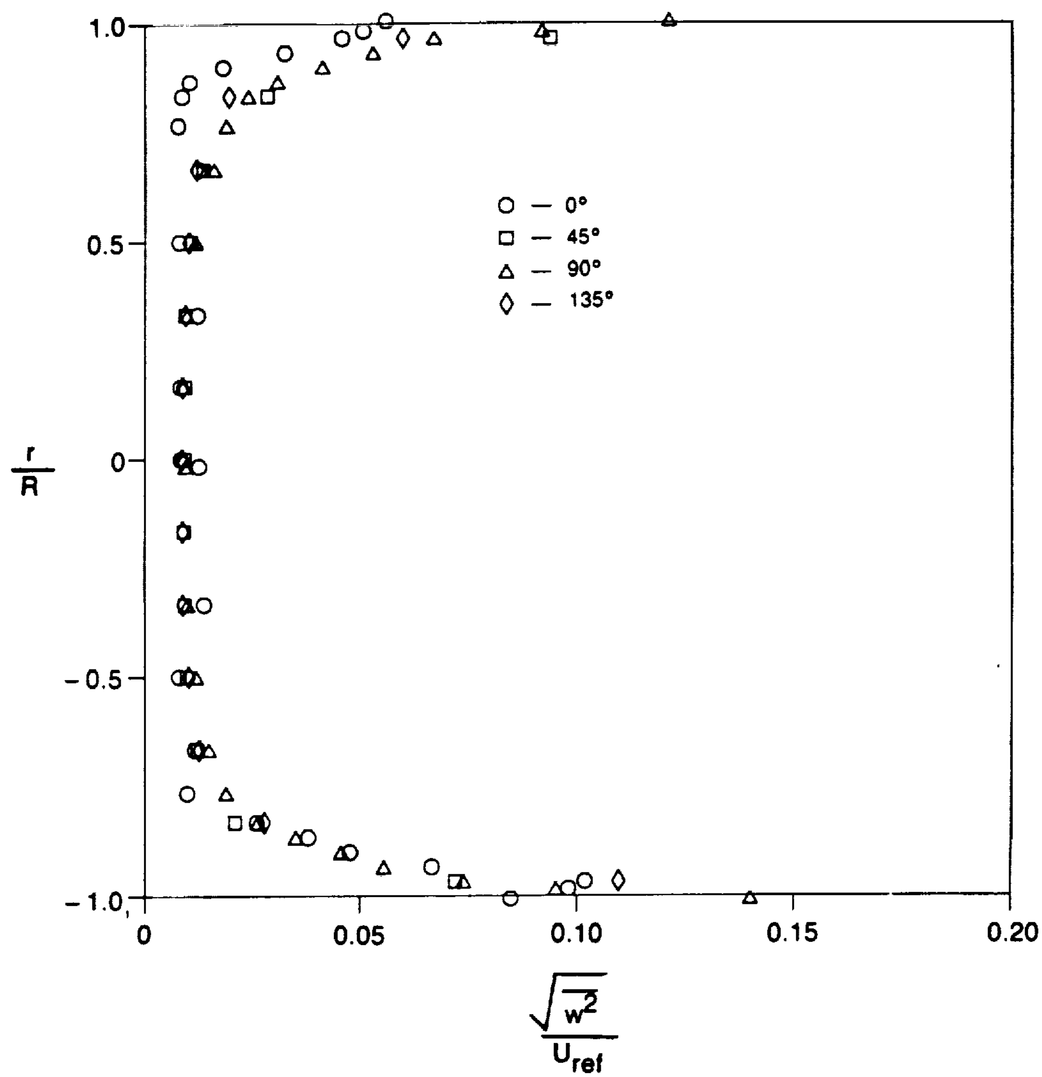

Figure 4-20. — Transverse Turbulence Profiles In AR630 Inlet Plane

87-9-19-32

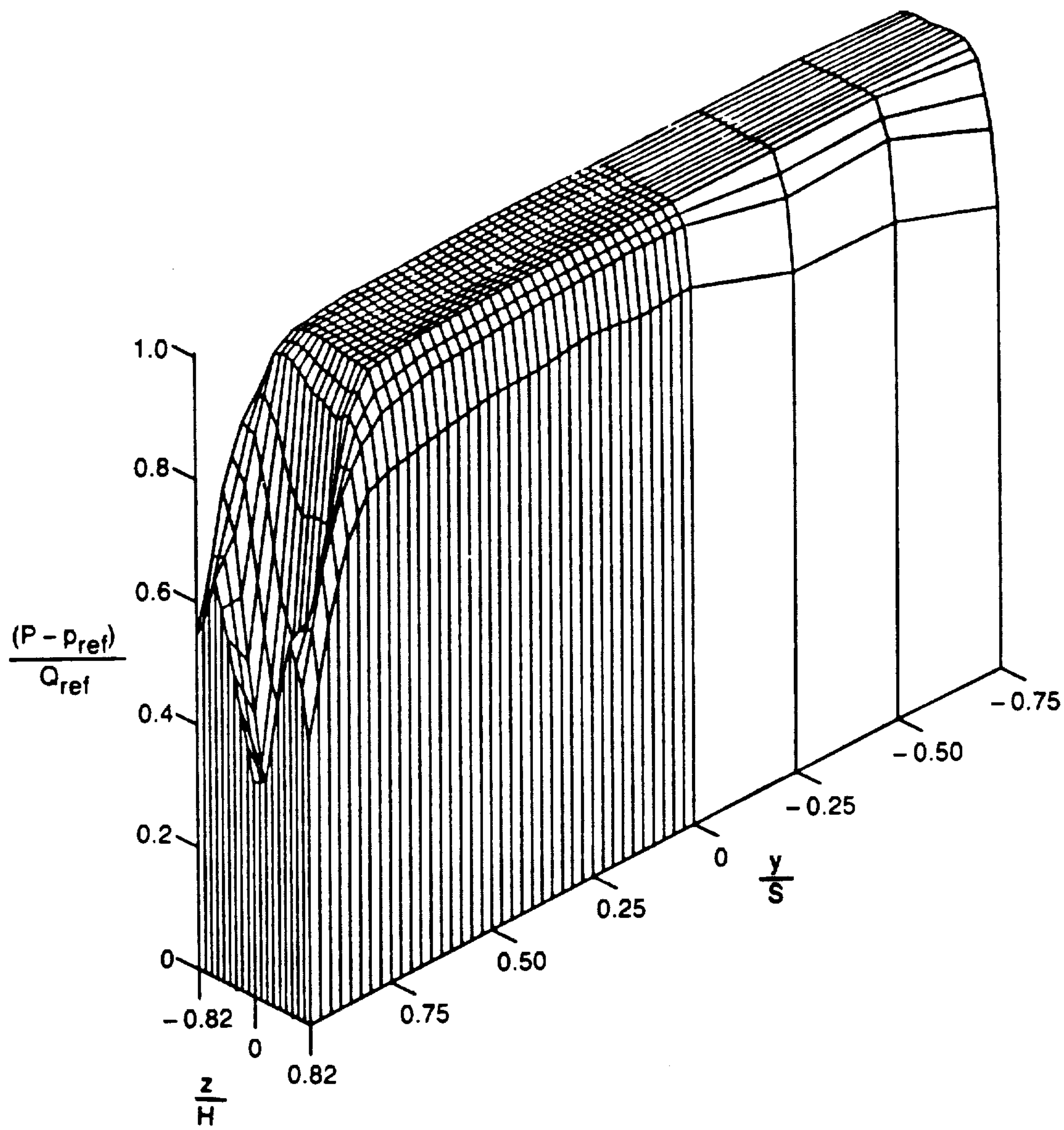

Figure 4-21a. — Total Pressure Distribution In AR630 Exit Plane

87-9-19-34

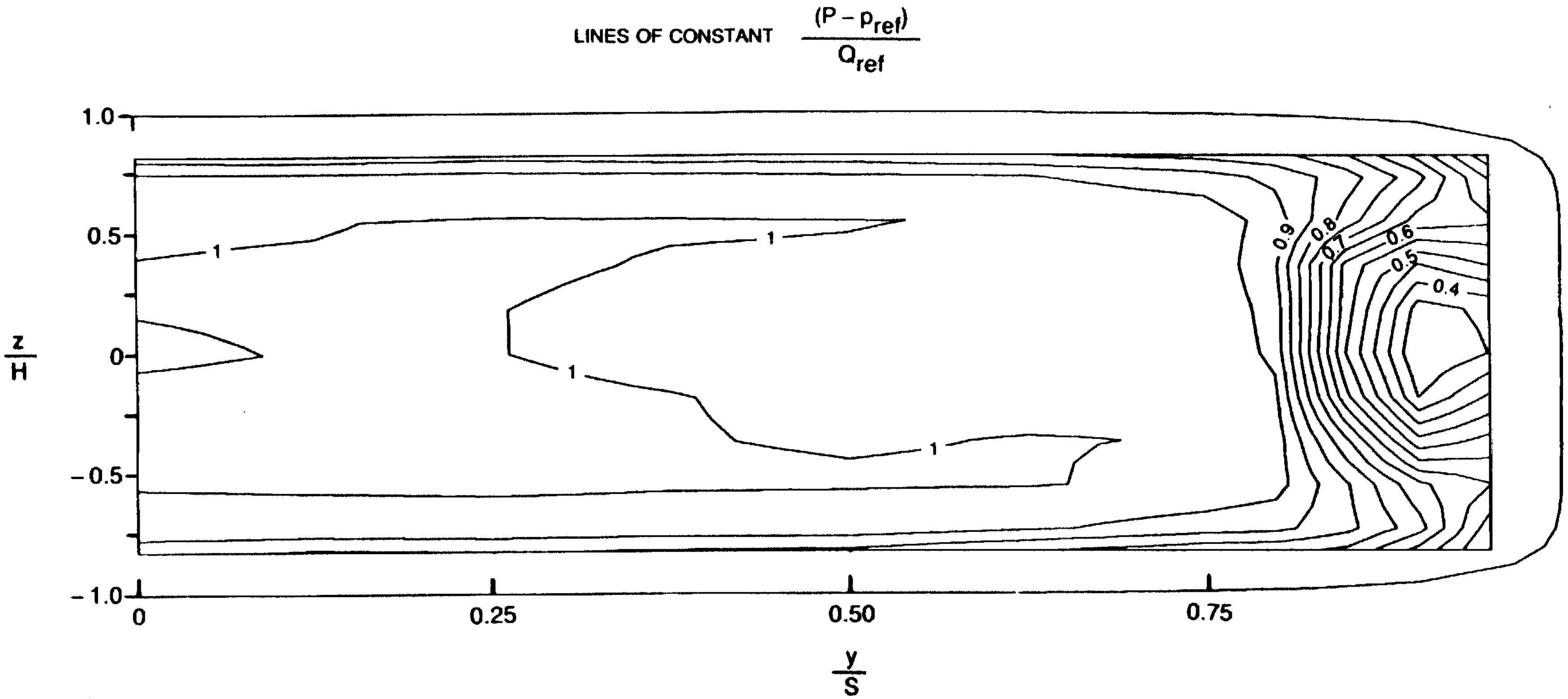

Figure 4-21b. — Total Pressure Distribution In AR630 Exit Plane

87-9-19-33

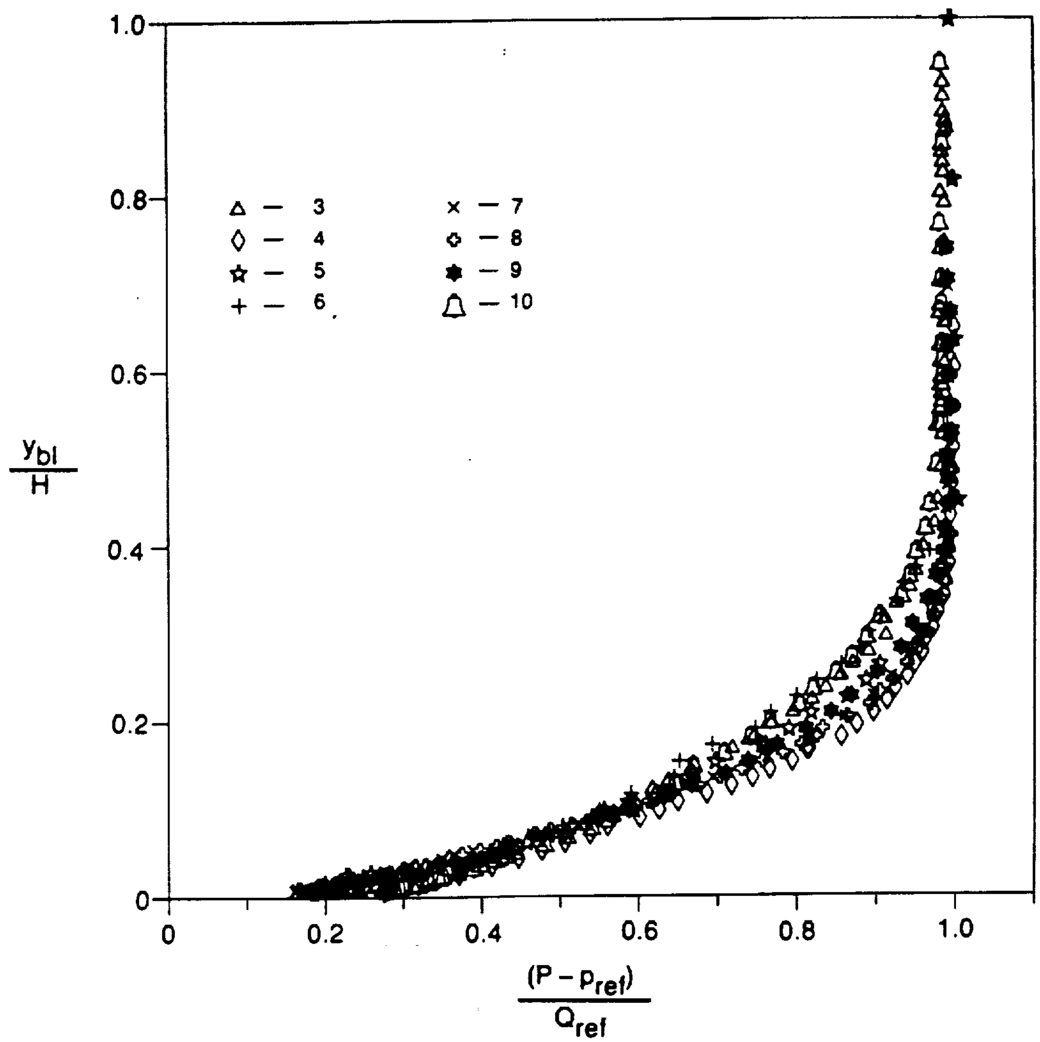

Figure 4-22a. — Transverse Total Pressure Boundary Layers in AR630 Exit Plane

87-9-19-35

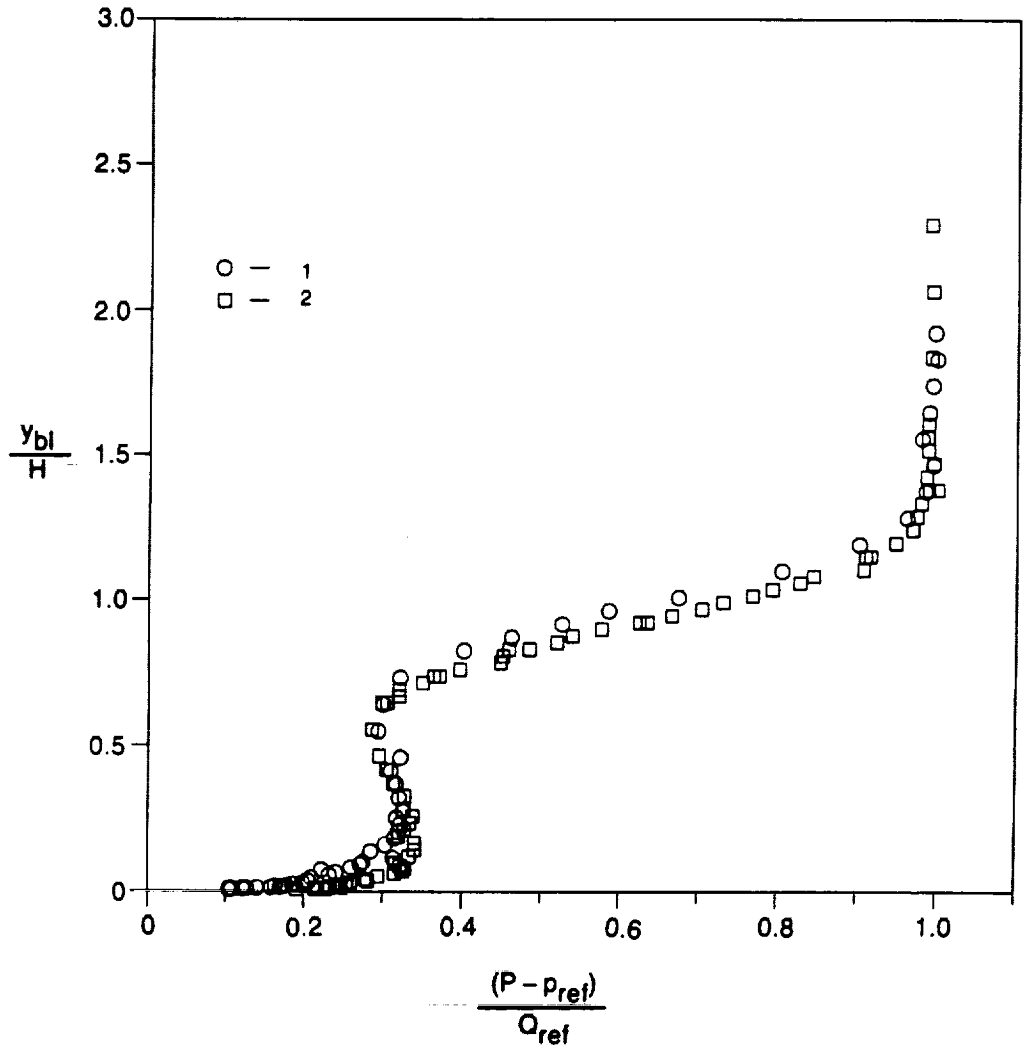

Figure 4-22b. — Spanwise Total Pressure Boundary Layers In AR630 Exit Plane

87-9-19-36

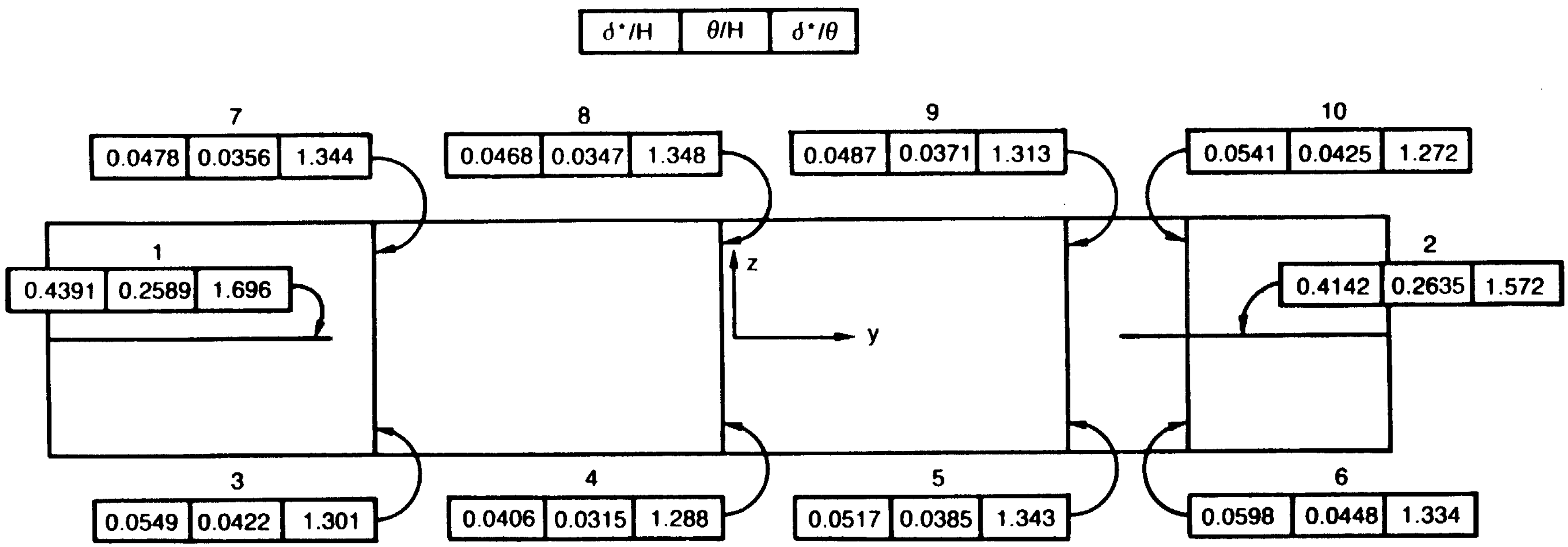

87-9-19-66

Figure 4-22c. — Boundary Layeer Integral Parameters in AR630 ExitPlane

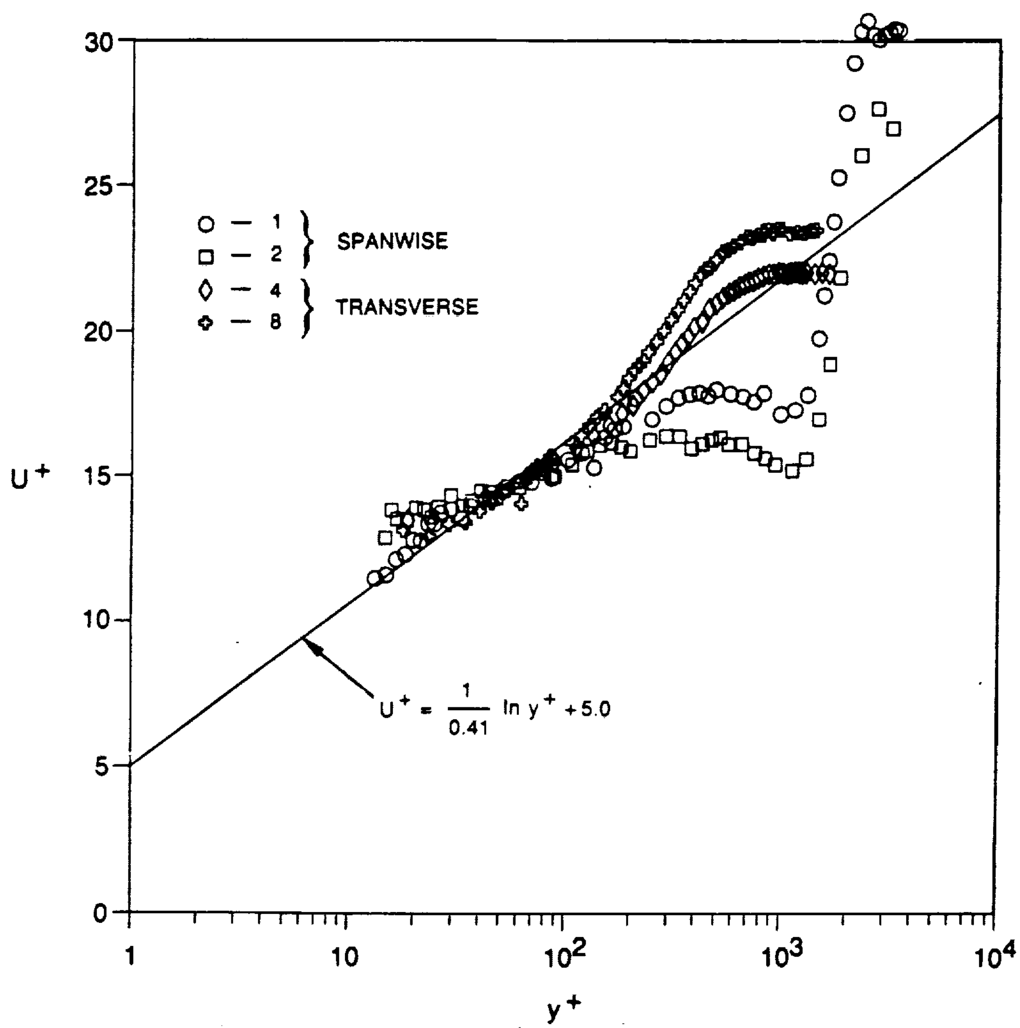

Figure 4-23. — Total Pressure Boundary Layer in AR630 Exit Plane, Law of the Wall Coordinates

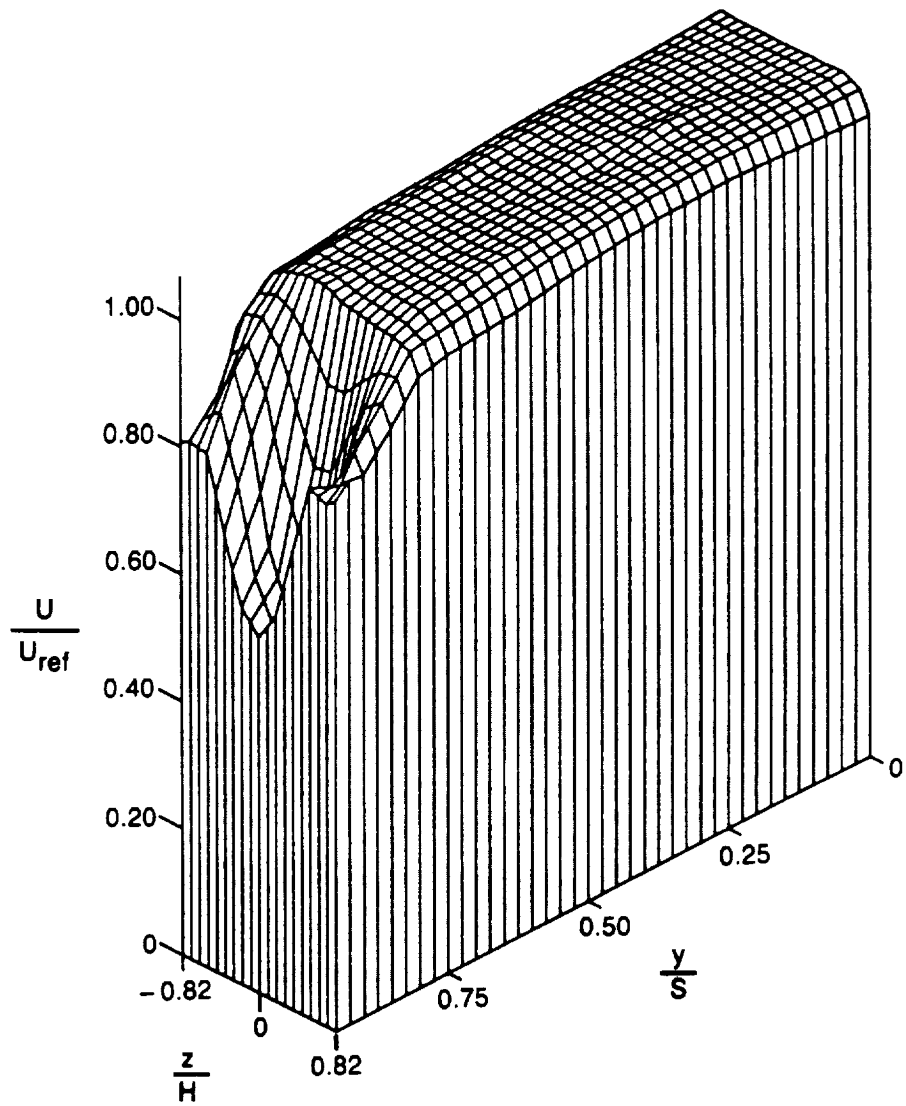

Figure 4-24a. — Axial Velocity in AR630 Exit Plane

87-9-19-39

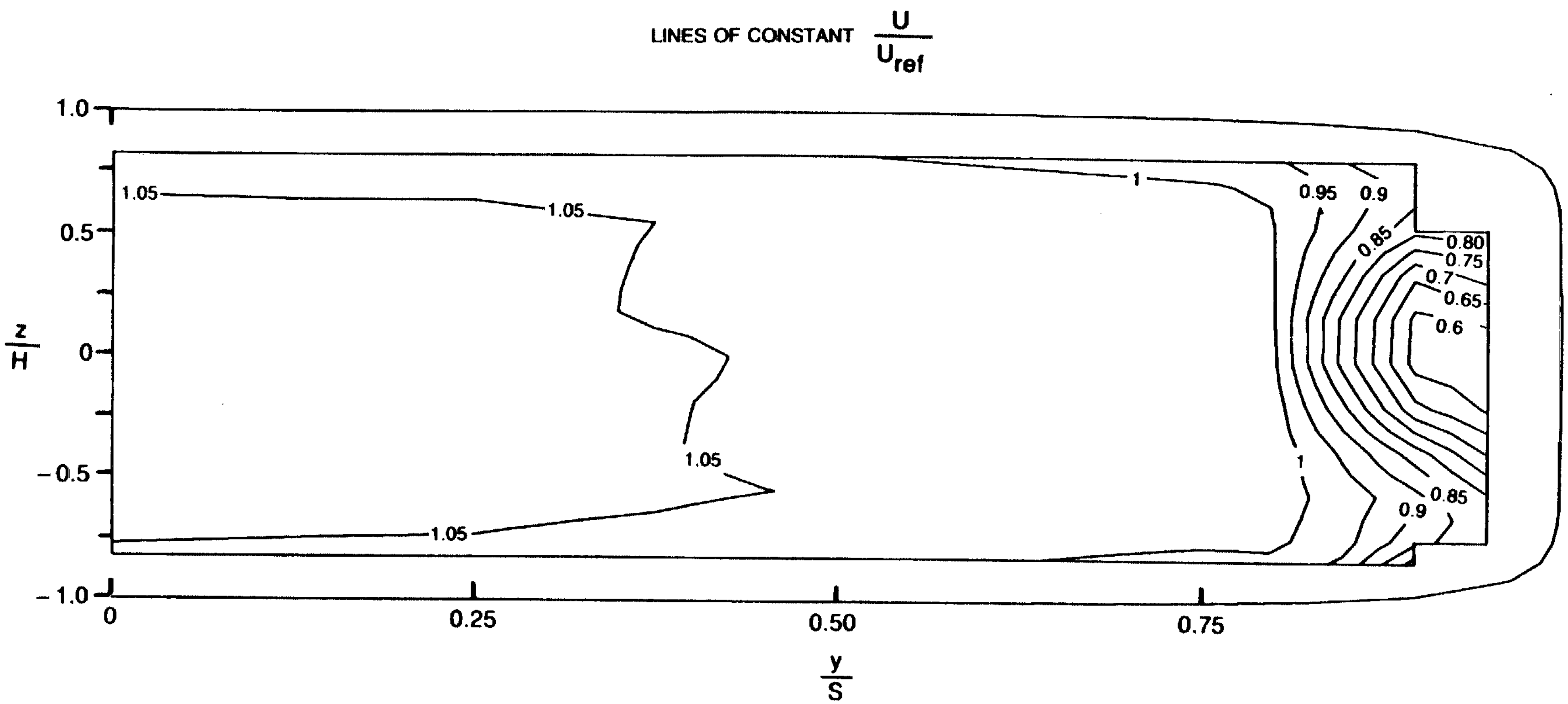

Figure 4-24b. — Axial Velocity Distribution In AR630 Exit Plane

87-9-19-38

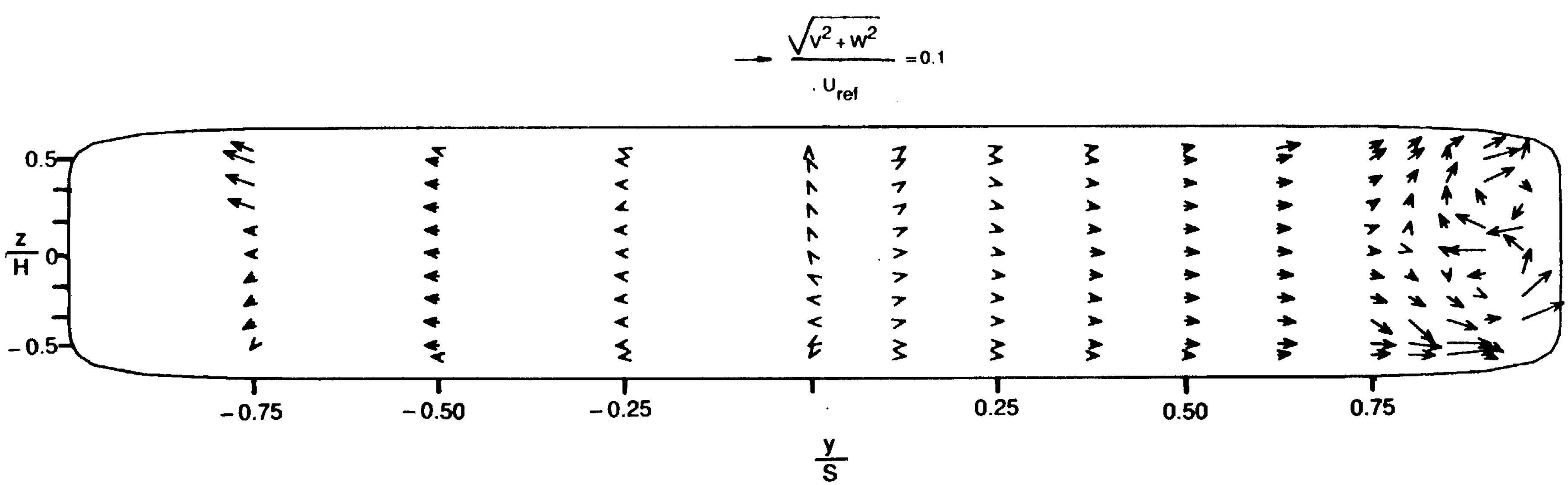

Figure 4-25. — Cross-Flow Velocity Vectors In AR630 Exit Plane

87-9-19-41

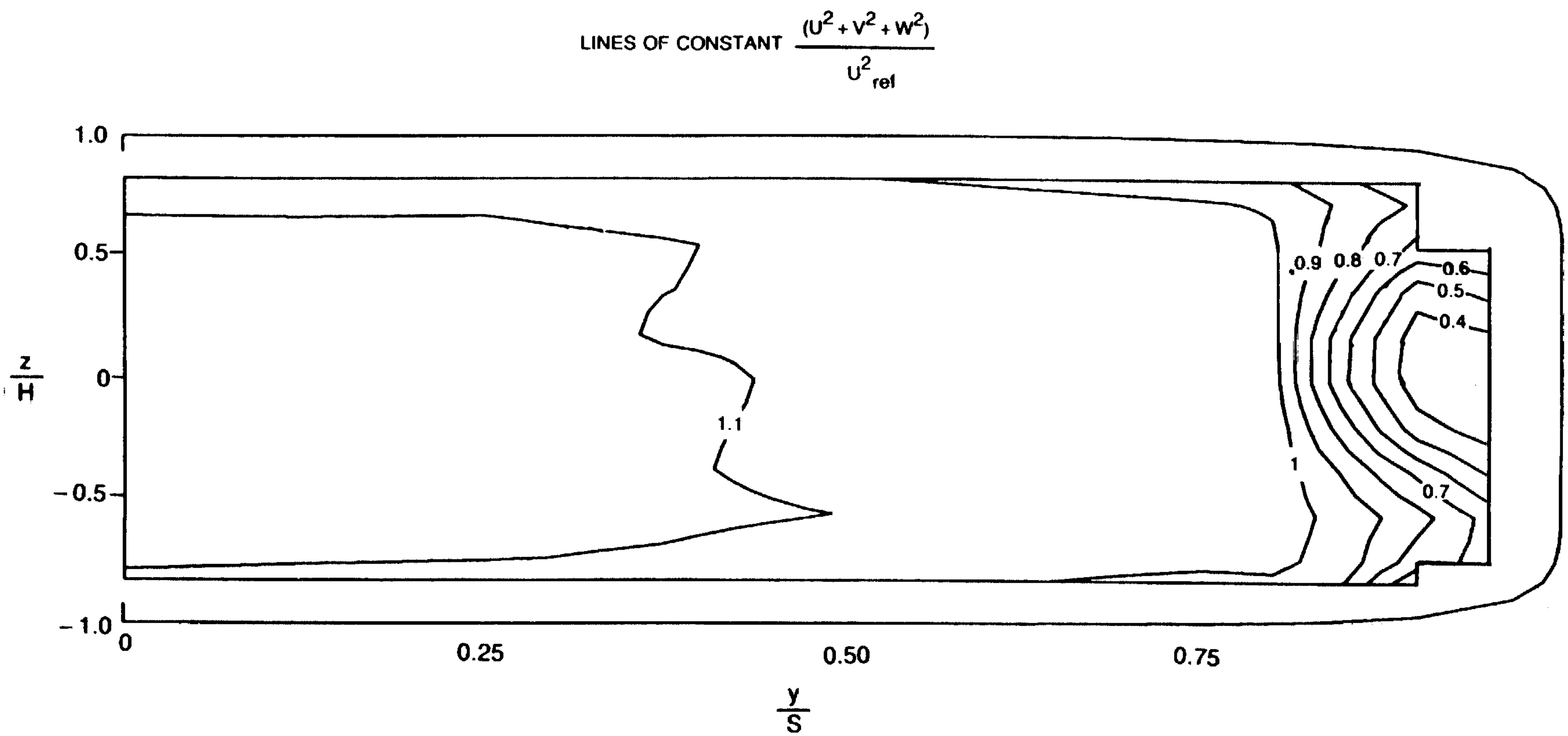

Figure 4-26. — Kinetic Energy Distribution In AR630 Exit Plane

87-9-19-40

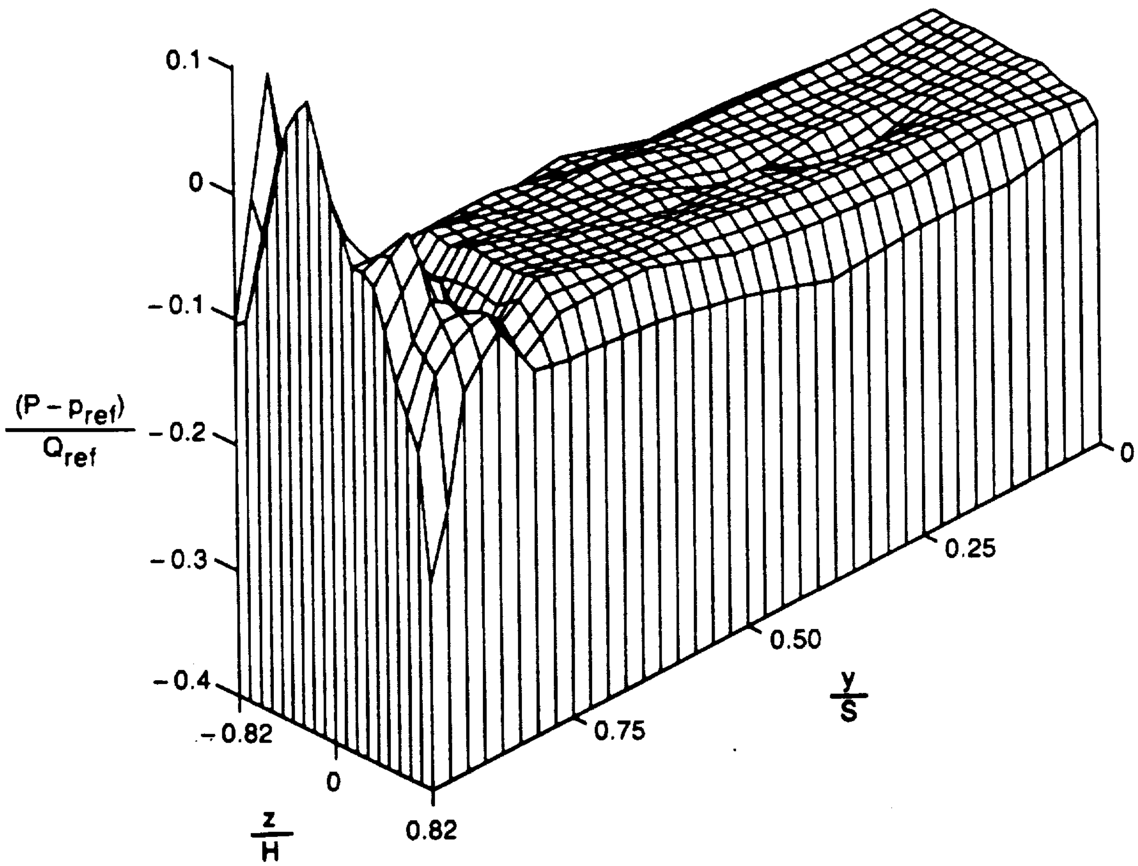

Figure 4-27a. — Static Pressure Distribution In AR630 Exit Plane

87-9-19-43

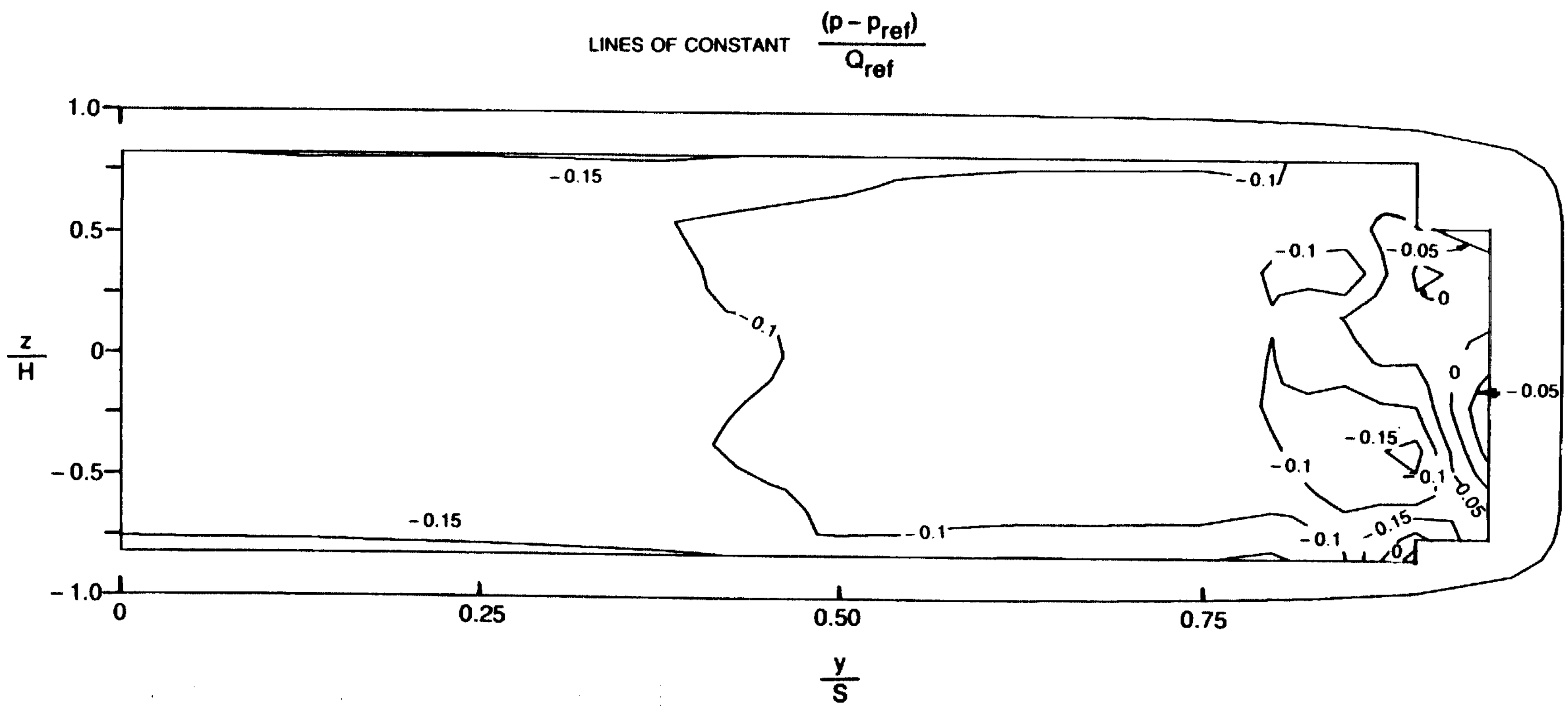

Figure 4-27b. — Static Pressure Distribution In AR630 Exit Plane

87-9-19-42

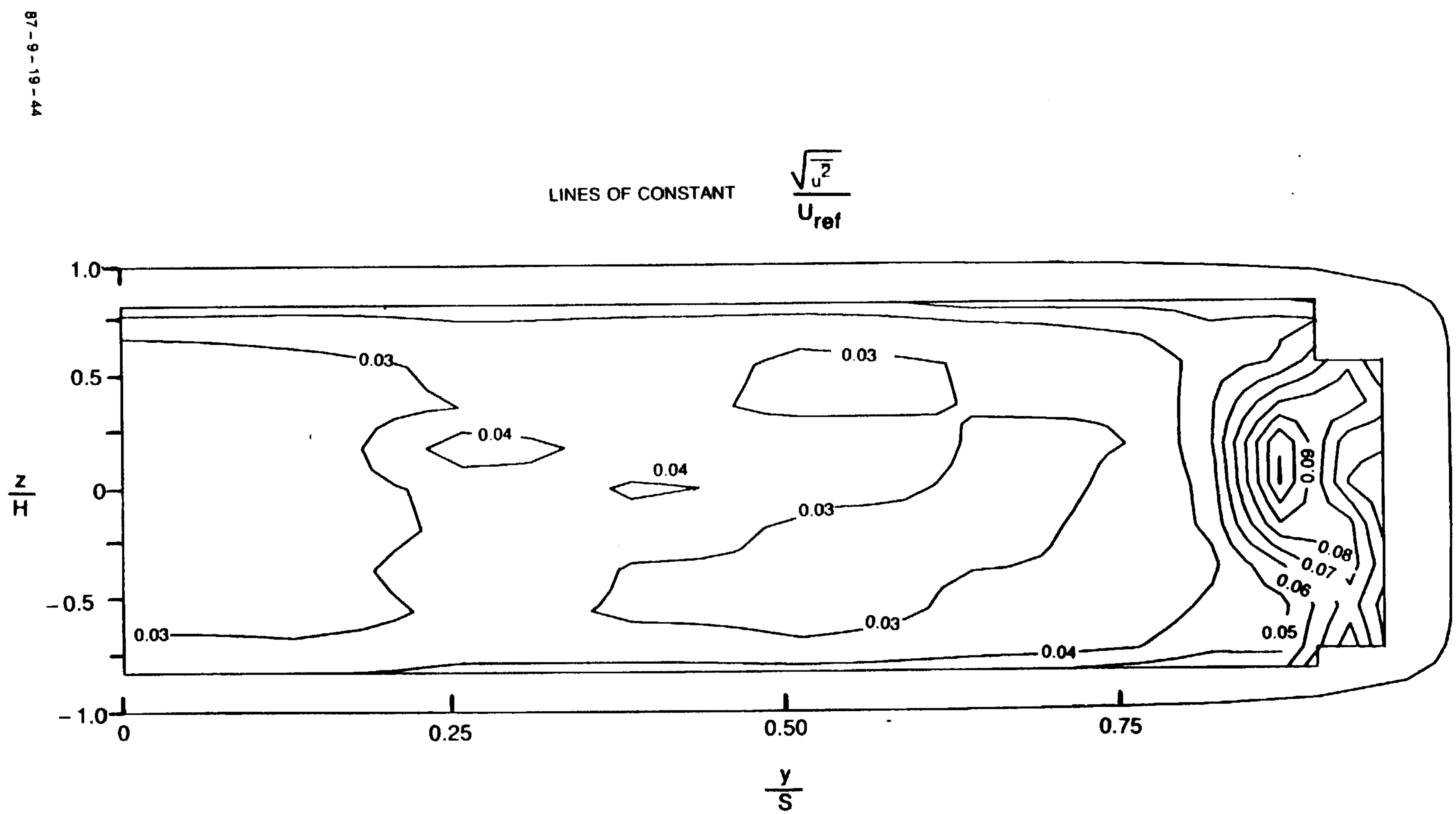

Figure 4-28. — Axial Turbulence Distribution In AR630 Exit Plane

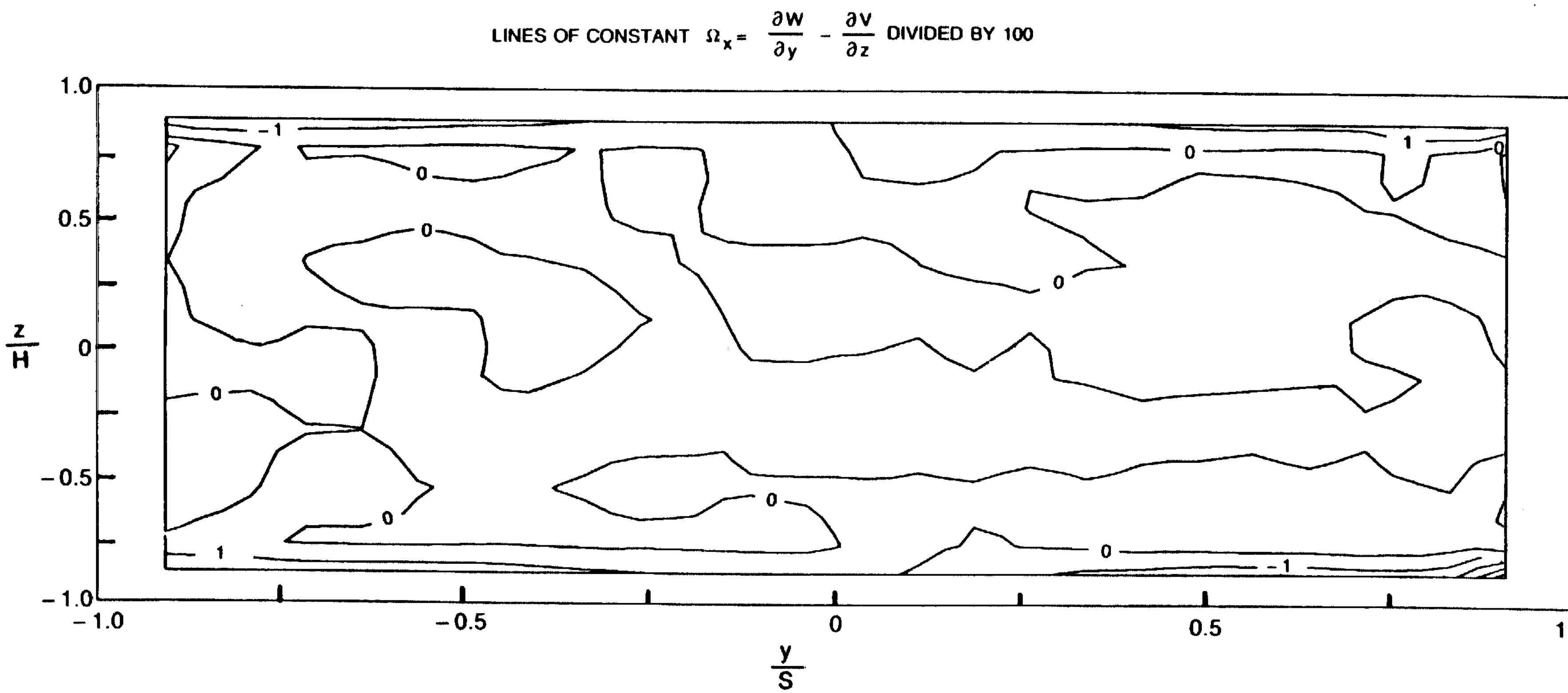

Figure 4-29a. — Axial Vorticity Distribution in AR310 Exit Plane

87-9-19-45

LINES OF CONSTANT $\xi = \frac{\partial w}{\partial y} - \frac{\partial v}{\partial z}$ DIVIDED BY 100

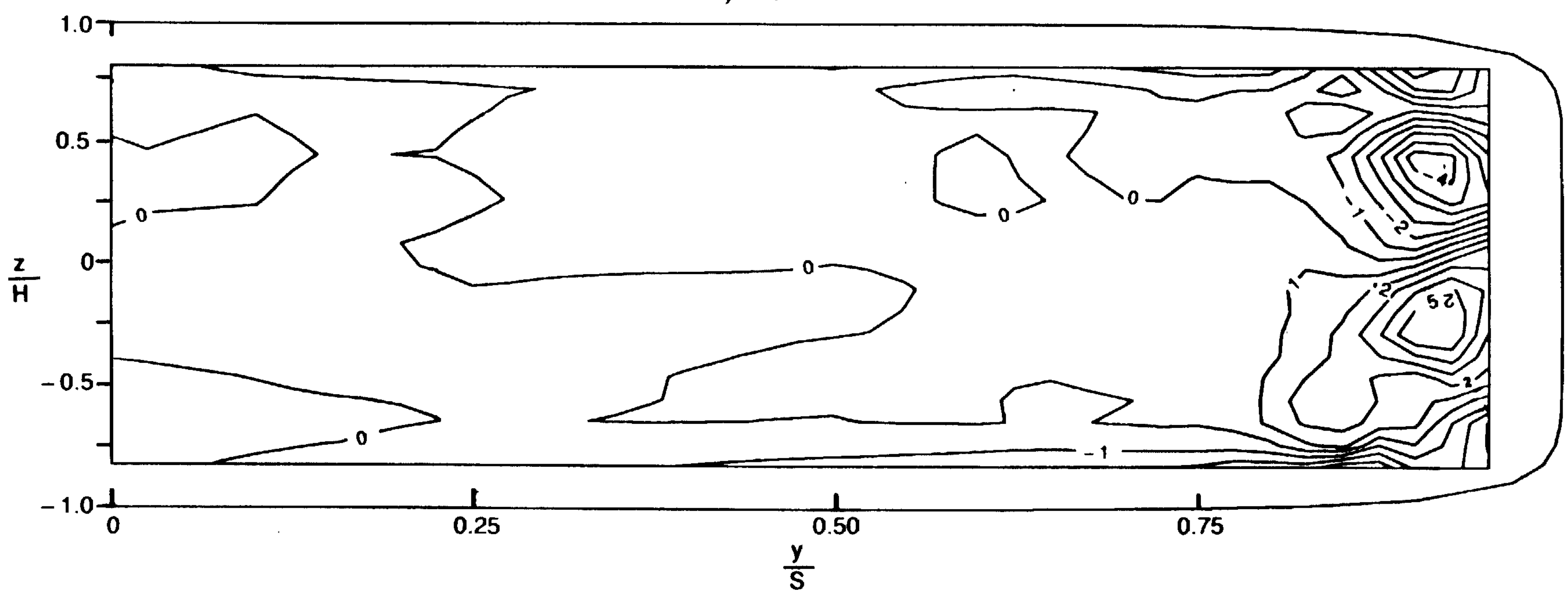

Figure 4-29b. — Axial Vorticity Distribution in AR630 Exit Plane

87-9-19-46

CHAPTER 5

CONCLUSIONS

Detailed data sets of the inlet and exit planes of two transition ducts, designated AR310 and AR630, have been obtained at low subsonic speeds (U_{ref} = 30.5 m/sec) using total pressure traverses and non-intrusive laser velocimetry measurements of three velocity components. The inlet flows had uniform, swirl-free velocity profiles with thin turbulent boundary layers (δ_{995}/D = 0.10) and turbulence levels on the order of two percent of the freestream velocity. Surface flow visualization showed that both ducts were unseparated throughout their transition sections.

The cross flows in the exit plane of each duct were small and were directed predominantly outward toward the sidewall. Maximum cross-flow velocities were 0.12 U_{ref} for the AR310 duct and 0.11 U_{ref} for the AR630 duct.

Total pressure distributions showed the flows to be symmetric in each duct. Axial velocity distributions in the exit plane were much flatter in the AR630 duct than the AR310 duct indicating that the flow had not completely expanded to fill the exit duct uniformly in the shorter AR310 duct prior to reaching the exit plane. The continuing expansion of the flow into the exit duct caused the outward cross flows.

The flow distributions differed significantly near the sidewalls of each duct. The sidewall boundary layers in the AR310 duct were relatively thin whereas the AR630 duct sidewall boundary layers were thickened by an axial vortex pair which transported low momentum fluid from the sidewalls into the core flow along the duct semi-major axis.

The fluid dynamics which created the sidewall vortex pair in the high aspect ratio AR630 duct are illustrated in Fig. (5-1). As shown in the figure, the streamtube near the sidewall of the transition duct approximates the shape of an S-duct. Towne and Schum (Ref. 20) have shown that the secondary flow pattern in an S-duct is initiated in the first bend where the higher velocity flow in the core flow moves away from the inner wall due to centrifugal force. This flow pattern results in lower static pressure along the inner wall (i.e. sidewall of transition duct) than along the adjacent walls (i.e. top and bottom walls of transition duct). The resulting pressure field creates a recirculation pattern within the boundary layers along the top and bottom walls toward the sidewall. At the inflection point of the S-duct a vortex pair has been formed. In the second bend of the S-duct, the pressure forces are reversed and the strength of the vortex pair may be diminished.

In the AR630 transition duct, however, the duct shape becomes nearly rectangular between the first and second bends in the sidewall causing the vortex pair to be concentrated and strengthened. Further assisting the strengthening of the vortex pair is the natural tendency of a flow in a straight rectangular duct to form corner vortices which induce flow to move from the sidewalls toward the core flow along the semi-major axis (Ref. 15). Each of these effects contributes to the vortex patterns in the AR630 exit plane.

Flow in the lower aspect ratio AR310 duct does not have the same contribution from vortex concentration and rectangular duct corner vortex development. Thus, the reduced strength of the vortices in the AR310 exit plane may result from the counteracting pressure forces at the second bend of the transition duct sidewall. Detailed surveys within the transition section are necessary to better define the secondary flow development within circular-to-rectangular transition ducts.

It is therefore concluded that secondary flows can play an important part in the fluid dynamics of transition ducts and needs to be addressed in computational analysis. The strength of the secondary flows depends on both the aspect ratio and relative axial duct length.

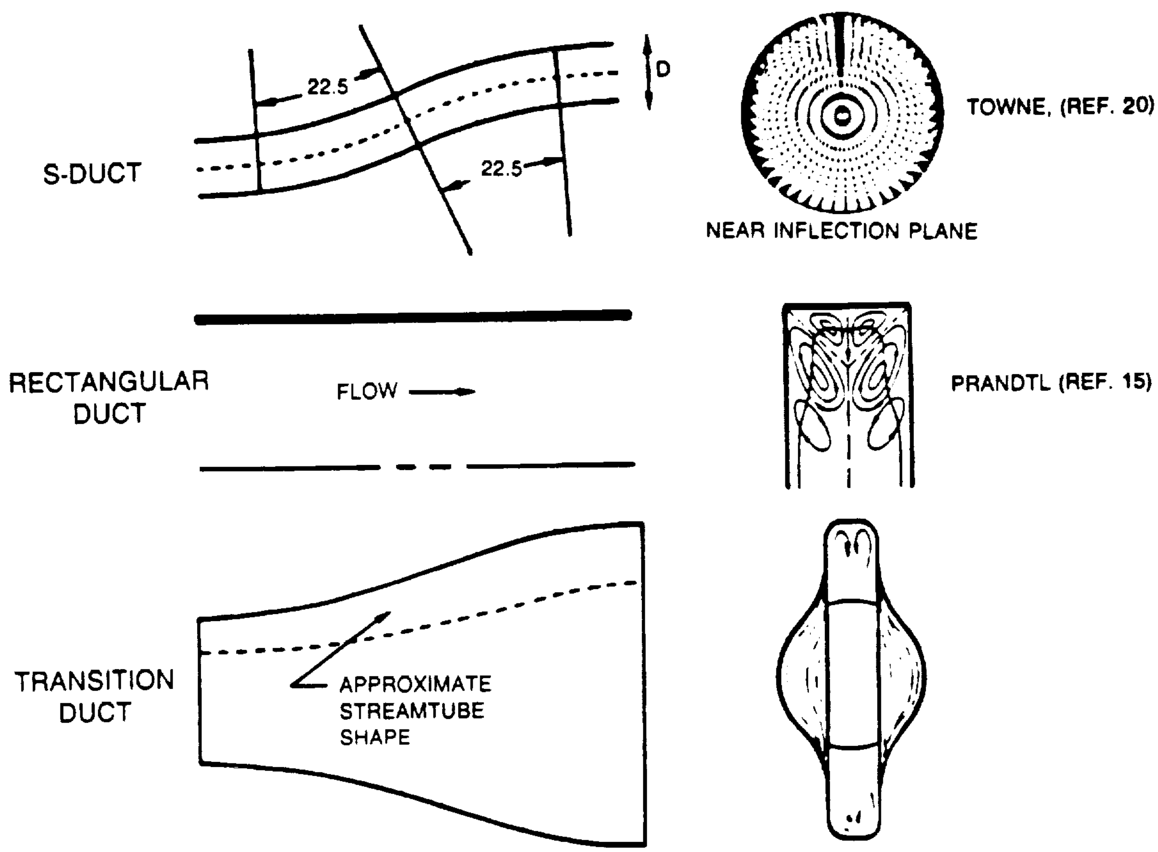

Figure 5-1. — High Aspect Ratio Duct Fluid Dynamics

87—9—19—73

REFERENCES

1. Burley, J.R., L.S. Bangert, and J.R. Carlson: Static Investigation of Circular-to-Rectangular Transition Ducts for High-Aspect-Ratio Nonaxisymmetric Nozzles, NASA TP-2534, March 1986.

2. Anderson, B.H.: Three-Dimensional Viscous Design Methodology for Advanced Technology Aircraft Supersonic Inlet Systems, AIAA Paper 84-0194, January 1984. (NASA TM-83558)

3. Anderson, B. H.: Personal Communication, 1985.

4. Mayer, E.: Einfluss der Querschnittsverformung auf die Entwicklung der Geschwindigkeits - und Druckverteilung bei turbulenten Stromungen in Rohren (Effect of Transition in Cross-Sectional Shape on Development of Velocity and Pressure Distribution of Turbulent Flow in Pipes), VDI-Forschungsheft 389 March/April 1938, (Available as NACA TM-903, August 1939).

5. Taylor, A.M.K.P., J.H. Whitelaw, and M. Yianneskis: Measurements of Laminar and Turbulent Flow in a Curved Duct with Thin Inlet Boundary Layers, NASA CR-3367, January 1981.

6. Enayet, M.M., M.M. Gibson, A.M.K.P. Taylor, and M. Yianneskis: Laser Doppler Measurements of Laminar and Turbulent Flow in a Pipe Bend, NASA CR-3551, May 1982.

7. Taylor, A.M.K.P., J.H. Whitelaw, and M. Yianneskis: Developing Flow in S-Shaped Ducts, I-Square Cross Section Duct, NASA CR-3550, May 1982.

8. Taylor, A.M.K.P., J.H. Whitelaw, and M. Yianneskis: Developing Flow in S-Shaped Ducts, II-Circular Cross Section Duct, NASA CR-3759, February 1984.

9. Taylor, A.M.K.P., J.H. Whitelaw, and M. Yianneskis: Turbulent Flow in a Square-to-Round Transition, NASA CR-3447, July 1981.

10. Vakili, A.D., J.M. Wu, P. Liver, and M.K. Bhat: Experimental Measurements in a Variable Area 30°-30° S-Duct, NASA CR-1985.

11. Crawford, R.A., C.E. Peters, J. Steinhoff, J.O. Hornkohl, J. Nourinejad, and K. Ramachandran: Mean Velocity, and Turbulence Measurements in a 90° Curved Duct with Thin Inlet Boundary Layer, NASA CR-174811, December 1985.

12. Melling, A., and J.H. Whitelaw: Turbulent Flow in a Rectangular Duct, J. of Fluid Mechanics, vol. 78, pt. 2, 1976, pp. 289-315.

13. Rowe, M.: Measurements and Computations of Flow in Pipe Bends, J. of Fluid Mechanics, vol. 43, pt. 4, 1970, pp. 771-783.

14. Bansod, P., and P. Bradshaw: The Flow in S-Shaped Ducts, Aeronautical Quarterly, vol. 23, May 1972, pp. 131-140.

15. Prandtl, L.: Turbulent Flow, NACA TM-435, October 1927.

16. Gutmark, E., and K.C. Schadow: Azimuthal Instabilities and Mixing Characteristics of a Small Aspect Ratio Slot Jet, AIAA Paper 87-0486, January 1987.

17. Gutmark, E., K.C. Schadow, T.P. Parr, D.M.Parr, and K.J. Wilson: Combustion Enhancement by Axial Vortices, AIAA Paper 87-1831, June 1987.

18. Roberts, D.W., and C.K. Forester: A Parabolic Computational Procedure for Three-Dimensional Flows in Ducts with Arbitrary Cross-Sections, AIAA Paper 78-143, January 1978.

19. Anderson, B.H., K.K. Muramoto, and R. Levy: A Study of Three-Dimensional Viscous Flow within High Aspect Ratio Transition Ducts, AIAA Paper 85-0085, January 1985.

20. Towne, C.E., and E.F. Schum: Application of Computational Fluid Dynamics to Complex Inlet Ducts, AIAA Paper 85-1213, July 1985.

21. Hama, F. R.: An Efficient Tripping Device, Journal of the Aeronautical Sciences, Vol. 24, March 1957, pp. 236-237.

22. Patrick, W. P.: Error Analysis for Benchmark Fluid Dynamic Experiments, Part I: Error Analysis Methodology and the Quantification of Laser Velocimeter Error Sources, Report R85-151772, United Technologies Research Center, East Hartford CT, 1985.

23. Coles, D. E.: The Turbulent Boundary Layer in a Compressible Fluid, Rand Corp. Report R-403-PR, September 1962.

24. Klebanoff, P. S.: Characteristics of Turbulence in a Boundary Layer with Zero Pressure Gradient, NACA Rep. No. 1247, 1955.

25. Kooi, J. W.: Influence of Free-Stream Mach Number on Transonic Shock-Wave Boundary-Layer Interaction, Report No. NLR MP 78013 U, National Aerospace Laboratory, Amsterdam, The Netherlands, May 23, 1978.

26. Patrick, W. P.: Flowfield Measurements in a Separated and Reattached Flat Plate Turbulent Boundary Layer, NASA CR-4052, March 1987.

C-2

TABLE I
COEFFICIENTS FOR SUPERELLIPSE EQUATION

AR310

x/R	rady	radz	η_y	η_z	AREA
0.00	1.0000000	1.0000000	2.0000000	2.0000000	1.0000
0.08	1.0024099	0.9975954	2.0000000	2.0000000	1.0000
0.16	1.0094080	0.9906801	2.0000000	2.0000000	1.0000
0.24	1.0206738	0.9797446	2.0000000	2.0000000	1.0000
0.32	1.0359344	0.9653125	2.0000000	2.0000000	1.0000
0.40	1.0549421	0.9479194	2.0000000	2.0000000	1.0000
0.48	1.0774775	0.9280938	2.0000000	2.0000000	1.0000
0.56	1.1033373	0.9063409	2.0000000	2.0000000	1.0000
0.64	1.1320353	0.8829026	2.0027151	2.0027151	1.0000
0.72	1.1614418	0.8568226	2.0255842	2.0255842	1.0000
0.80	1.1923180	0.8294398	2.0596504	2.0596504	1.0000
0.88	1.2242432	0.8011267	2.1072369	2.1072369	1.0000
0.96	1.2567968	0.7722556	2.1712093	2.1712093	1.0000
1.04	1.2895613	0.7431985	2.2551298	2.2551298	1.0000
1.12	1.3221149	0.7143273	2.3637581	2.3637581	1.0000
1.20	1.3540401	0.6860142	2.5035934	2.5035934	1.0000
1.28	1.3849163	0.6586313	2.6835108	2.6835108	1.0000
1.36	1.4143238	0.6325510	2.9163589	2.9163589	1.0000
1.44	1.4418430	0.6081454	3.2209034	3.2209034	1.0000
1.52	1.4670544	0.5857865	3.6254110	3.6254110	1.0000
1.60	1.4895382	0.5658464	4.1731195	4.1731195	1.0000
1.68	1.5088749	0.5486974	4.9304876	4.9304876	1.0000
1.76	1.5246449	0.5347114	5.9920216	5.9920216	1.0000
1.84	1.5364285	0.5242606	7.4425745	7.4425745	1.0000
1.92	1.5438070	0.5177172	9.1124592	9.1124592	1.0000
2.00	1.5463591	0.5154534	10.0000000	10.0000000	1.0000

AR630

x/R	rady	radz	η_y	η_z	AREA
0.00	1.0000000	1.0000000	2.0000000	2.0000000	1.0000
0.24	1.0007143	0.9996173	2.0000000	2.0000000	1.0003
0.48	1.0053711	0.9971241	2.0000000	2.0000000	1.0025
0.72	1.0169945	0.9909001	2.0000000	2.0000000	1.0077
0.96	1.0376930	0.9798167	2.0000000	2.0000000	1.0167
1.20	1.0687437	0.9631907	2.0000000	2.0000000	1.0294
1.44	1.1106777	0.9407371	2.0000000	2.0000000	1.0449
1.68	1.1633711	0.9125222	2.0000000	2.0000000	1.0616
1.92	1.2261314	0.8789169	2.0000000	2.0000000	1.0777
2.16	1.2977848	0.8405501	2.0000000	2.0000000	1.0909
2.40	1.3767633	0.7982608	2.0000000	2.0000000	1.0990
2.64	1.4611921	0.7530529	2.0000000	2.0000000	1.1004
2.88	1.5489798	0.7060472	2.0000000	2.0000000	1.0937
3.12	1.6379013	0.6584340	2.0000000	2.0000000	1.0784
3.36	1.7256889	0.6114279	2.0000000	2.0000000	1.0551
3.60	1.8101177	0.5662202	2.0000000	2.0000000	1.0249
3.84	1.8890963	0.5239310	2.0551491	2.0551491	1.0000
4.08	1.9607496	0.4855640	2.3025522	2.3025522	1.0000
4.32	2.0235100	0.4519587	2.6555567	2.6555567	1.0000
4.56	2.0762043	0.4237437	3.1646576	3.1646576	1.0000
4.80	2.1181374	0.4012903	3.9101000	3.9101000	1.0000
5.04	2.1491880	0.3846643	5.0090160	5.0090160	1.0000
5.28	2.1698866	0.3735808	6.5705433	6.5705433	1.0000
5.52	2.1815100	0.3673569	8.4278431	8.4278431	1.0000
5.76	2.1861649	0.3648642	9.7414103	9.7414103	1.0000
6.00	2.1868830	0.3644805	9.9999752	9.9999752	1.0000

TABLE IIa
AR310 INLET BOUNDARY LAYER

$\nu = 1.577 \times 10^{-5}\ m^2/s$
$U_\tau = 1.402$ m/s
$U_{ref} = 33.00$ m/s

y/R	U/U_{ref}	y+	U+
0.0018	0.463	18.06	10.893
0.0023	0.520	22.57	12.250
0.0027	0.563	27.09	13.247
0.0032	0.585	31.61	13.761
0.0037	0.596	36.13	14.021
0.0043	0.607	42.90	14.299
0.0050	0.634	49.67	14.915
0.0057	0.641	56.45	15.094
0.0064	0.650	63.23	15.303
0.0073	0.664	72.26	15.637
0.0082	0.671	81.29	15.784
0.0096	0.691	94.84	16.260
0.0110	0.704	108.39	16.569
0.0133	0.718	130.97	16.910
0.0155	0.731	153.54	17.201
0.0190	0.763	187.42	17.948
0.0224	0.772	221.30	18.180
0.0270	0.800	266.46	18.823
0.0315	0.814	311.61	19.167
0.0361	0.849	356.78	19.974
0.0407	0.865	401.94	20.354
0.0498	0.899	492.27	21.154
0.0590	0.923	582.59	21.719
0.0681	0.945	672.92	22.252
0.0773	0.953	763.25	22.423
0.0864	0.963	853.58	22.657
0.0955	0.956	943.89	22.493
0.1047	0.962	1034.22	22.644
0.1230	0.972	1214.87	22.887
0.1413	0.975	1395.53	22.944
0.1641	0.978	1621.34	23.031
0.1870	0.982	1847.15	23.116
0.2098	0.993	2072.96	23.373
0.2327	0.985	2298.78	23.192
0.2898	0.986	2863.31	23.197
0.3470	0.990	3427.85	23.308
0.4613	0.990	4556.92	23.305
0.5755	0.989	5685.98	23.277
0.6898	0.993	6815.05	23.379
0.8041	0.990	7944.12	23.308
0.9184	0.993	9073.19	23.363
1.0327	0.991	10202.25	23.336

87-9-19-53

TABLE IIb
AR630 INLET BOUNDARY LAYERS

$\nu = 1.411 \times 10^{-5}\ m^2/s$
$U_\tau = 1.234$ m/s
$U_{ref} = 28.96$ m/s

θ = 0

y/R	U/U_{ref}	y+	U+
0.0020	0.447	13.33	10.482
0.0020	0.447	13.33	10.487
0.0027	0.500	17.77	11.739
0.0033	0.542	22.22	12.724
0.0040	0.567	26.66	13.290
0.0047	0.587	31.11	13.766
0.0053	0.598	35.55	14.023
0.0060	0.611	39.99	14.341
0.0067	0.622	44.44	14.596
0.0077	0.635	51.10	14.885
0.0087	0.644	57.77	15.117
0.0097	0.652	64.43	15.291
0.0107	0.663	71.10	15.548
0.0117	0.669	77.76	15.703
0.0130	0.681	86.65	15.968
0.0143	0.682	95.54	15.986
0.0157	0.689	104.43	16.151
0.0190	0.710	126.65	16.647
0.0223	0.724	148.86	16.974
0.0257	0.732	171.08	17.162
0.0323	0.752	215.52	17.647
0.0390	0.769	259.96	18.047
0.0457	0.795	304.39	18.638
0.0523	0.816	348.83	19.138
0.0590	0.834	393.27	19.559
0.0657	0.847	437.71	19.876
0.0723	0.865	482.14	20.299
0.0790	0.883	526.58	20.713
0.0857	0.899	571.02	21.077
0.0957	0.918	637.67	21.532
0.1057	0.933	704.33	21.885
0.1157	0.958	770.98	22.465
0.1257	0.972	837.64	22.803
0.1357	0.980	904.30	22.995
0.1457	0.986	970.95	23.137
0.1590	0.993	1059.83	23.293
0.1723	0.997	1148.70	23.395
0.1857	0.996	1237.57	23.372
0.2190	1.000	1459.76	23.445
0.2523	1.000	1681.95	23.453
0.2857	1.000	1904.13	23.466
0.3190	1.001	2126.32	23.488
0.3523	1.002	2348.50	23.505
0.4857	1.001	3237.24	23.486
0.6190	1.002	4125.99	23.512
0.7523	1.000	5014.73	23.457
0.8857	0.998	5903.47	23.419
1.0190	1.000	6792.22	23.450
1.1523	1.001	7680.96	23.486
1.2857	1.001	8569.70	23.478
1.4190	1.002	9458.45	23.502
1.5523	1.003	10347.18	23.532
1.6857	1.002	11235.93	23.508
1.8190	0.999	12124.67	23.435
1.8523	0.996	12346.85	23.362

θ = 90

y/R	U/U_{ref}	y+	U+
0.0020	0.473	13.33	11.096
0.0020	0.472	13.33	11.073
0.0027	0.519	17.77	12.180
0.0033	0.547	22.22	12.830
0.0040	0.568	26.66	13.319
0.0047	0.578	31.11	13.564
0.0053	0.591	35.55	13.866
0.0060	0.601	39.99	14.093
0.0067	0.609	44.44	14.283
0.0073	0.614	48.88	14.405
0.0083	0.624	55.55	14.637
0.0093	0.638	62.21	14.959
0.0103	0.647	68.88	15.169
0.0103	0.643	68.88	15.094
0.0113	0.653	75.54	15.327
0.0123	0.656	82.21	15.398
0.0133	0.671	88.87	15.748
0.0153	0.682	102.21	15.994
0.0173	0.697	115.54	16.357
0.0193	0.707	128.87	16.590
0.0213	0.715	142.20	16.771
0.0247	0.730	164.42	17.119
0.0280	0.753	186.64	17.656
0.0347	0.767	231.07	17.987
0.0413	0.786	275.51	18.430
0.0480	0.810	319.95	19.001
0.0547	0.829	364.38	19.450
0.0613	0.845	408.82	19.813
0.0680	0.861	453.26	20.199
0.0747	0.880	497.70	20.644
0.0880	0.910	586.57	21.354
0.1013	0.942	675.44	22.102
0.1147	0.960	764.32	22.510
0.1280	0.978	853.19	22.931
0.1413	0.986	942.07	23.135
0.1547	0.991	1030.94	23.253
0.1680	0.993	1119.82	23.283
0.2013	0.994	1342.00	23.318
0.2347	0.995	1564.19	23.333
0.2680	0.995	1786.37	23.344
0.3013	0.997	2008.56	23.382
0.3347	0.996	2230.74	23.357
0.5013	0.999	3341.67	23.427
0.6680	0.998	4452.60	23.414
0.8347	0.998	5563.53	23.414
1.0013	1.000	6674.46	23.448
1.0013	0.999	6674.46	23.422
1.0013	0.996	6674.46	23.365
1.1680	0.997	7785.39	23.398
1.3347	0.997	8896.31	23.376
1.5013	0.998	10007.24	23.402
1.6680	0.995	11118.16	23.338
1.8347	0.992	12229.09	23.261
1.8347	0.994	12229.09	23.309
1.8347	0.991	12229.09	23.253
1.8857	0.975	12569.04	22.867
1.9190	0.921	12791.23	21.610
1.9190	0.927	12791.23	21.740

87-9-19-54

TABLE IIIa
AR310 EXIT PLANE DATA

y/S	z/H	$(P - P_{ref})/Q_{ref}$	$(p - P_{ref})/Q_{ref}$	U/U_{ref}	V/U_{ref}	W/U_{ref}	$\sqrt{\overline{u^2}}/U_{ref}$	$\sqrt{\overline{v^2}}/U_{ref}$	$\sqrt{\overline{w^2}}/U_{ref}$	
-0.908	0.879	0.3949	-0.0276	0.6409	-0.1073	0.0150	0.1374	0.0991	0.0864	(5)
-0.908	0.659	0.7654	0.0178	0.8622	-0.0571	0.0297	0.0493	0.0407	0.0420	(5)
-0.908	0.440	0.7336	-0.1675	0.9478	-0.0485	0.0208	0.0587	0.0301	0.0400	
-0.908	0.220	0.8222	-0.1014	0.9597	-0.0505	0.0068	0.0301	0.0279	0.0351	
-0.908	0.000	0.8785	-0.0245	0.9492	-0.0451	0.0048	0.0304	0.0261	0.0331	
-0.908	-0.220	0.8806	0.0853	0.8915	-0.0243	0.0031	0.0427	0.0354	0.0291	
-0.908	-0.440	0.8229	0.0007	0.9056	-0.0455	-0.0070	0.0466	0.0331	0.0335	
-0.908	-0.659	0.8090	-0.0108	0.9014	-0.0843	-0.0144	0.0475	0.0377	0.0641	(-5)
-0.908	-0.879	0.5583	0.1390	0.6424	-0.0797	0.0147	0.1329	0.1066	0.0841	(-5)
-0.757	0.879	0.8243	-0.0305	0.9215	-0.0751	-0.0059	0.0494	0.0374	0.0413	(5)
-0.757	0.659	0.9865	-0.0163	0.9988	-0.0722	-0.0006	0.0195	0.0141	0.0188	(5)
-0.757	0.440	0.9954	-0.0367	1.0135	-0.0700	0.0009	0.0171	0.0113	0.0140	
-0.757	0.220	0.9887	-0.0330	1.0084	-0.0693	0.0010	0.0161	0.0157	0.0120	
-0.757	0.000	0.9953	-0.0251	1.0075	-0.0728	-0.0059	0.0172	0.0141	0.0166	
-0.757	-0.220	1.0008	-0.0584	1.0271	-0.0656	-0.0037	0.0183	0.0139	0.0104	
-0.757	-0.440	1.0030	-0.0145	1.0061	-0.0726	-0.0026	0.0164	0.0118	0.0119	
-0.757	-0.659	0.9758	-0.0143	0.9924	-0.0720	0.0048	0.0213	0.0144	0.0187	(-5)
-0.757	-0.879	0.8561	0.0044	0.9198	-0.0734	0.0169	0.0483	0.0396	0.0411	(-5)
-0.606	0.879	0.8748	-0.1232	0.9964	-0.0719	-0.0033	0.0384	0.0284	0.0315	(5)
-0.606	0.659	0.9924	-0.0761	1.0314	-0.0680	-0.0084	0.0163	0.0120	0.0145	(5)
-0.606	0.440	1.0044	-0.0840	1.0403	-0.0782	-0.0077	0.0163	0.0099	0.0117	
-0.606	0.220	1.0041	-0.0739	1.0362	-0.0656	-0.0028	0.0158	0.0131	0.0106	
-0.606	0.000	1.0026	-0.0730	1.0349	-0.0676	0.0009	0.0170	0.0113	0.0124	
-0.606	-0.220	1.0036	-0.0676	1.0325	-0.0714	0.0057	0.0163	0.0123	0.0095	
-0.606	-0.440	1.0021	-0.0741	1.0345	-0.0[illegible]9	0.0112	0.0164	0.0105	0.0109	
-0.606	-0.659	0.9962	-0.0595	1.0249	-0.0717	0.0094	0.0187	0.0128	0.0123	(-5)
-0.606	-0.879	0.8987	-0.0755	0.9841	-0.0750	0.0089	0.0485	0.0370	0.0294	(-5)
-0.454	0.879	0.8905	-0.1816	1.0336	-0.0615	-0.0005	0.0323	0.0228	0.0314	(5)
-0.454	0.659	1.0008	-0.1219	1.0582	-0.0534	-0.0041	0.0162	0.0108	0.0164	(5)
-0.454	0.440	1.0017	-0.1294	1.0617	-0.0622	-0.0042	0.0157	0.0093	0.0113	
-0.454	0.220	1.0049	-0.1155	1.0567	-0.0619	-0.0028	0.0153	0.0126	0.0112	
-0.454	0.000	1.0029	-0.1096	1.0530	-0.0607	-0.0036	0.0166	0.0124	0.0116	
-0.454	-0.220	1.0029	-0.1133	1.0549	-0.0583	0.0026	0.0158	0.0145	0.0103	
-0.454	-0.440	1.0040	-0.1282	1.0621	-0.0647	0.0060	0.0160	0.0100	0.0109	
-0.454	-0.659	1.0001	-0.1120	1.0524	-0.0670	0.0055	0.0177	0.0122	0.0124	(-5)
-0.454	-0.879	0.9288	-0.0525	0.9884	-0.0660	0.0062	0.0519	0.0362	0.0257	(-5)
-0.303	0.879	0.8663	-0.2695	1.0650	-0.0404	-0.0043	0.0253	0.0174	0.0271	(5)
-0.303	0.659	0.9664	-0.1980	1.0782	-0.0419	-0.0073	0.0158	0.0100	0.0217	(5)
-0.303	0.440	0.9978	-0.1667	1.0783	-0.0428	-0.0036	0.0161	0.0091	0.0114	
-0.303	0.220	1.0005	-0.1502	1.0717	-0.0460	0.0020	0.0157	0.0118	0.0111	
-0.303	0.000	1.0020	-0.1425	1.0690	-0.0418	0.0002	0.0171	0.0110	0.0122	
-0.303	-0.220	0.9988	-0.1583	1.0747	-0.0453	0.0050	0.0169	0.0114	0.0105	
-0.303	-0.440	0.9958	-0.1824	1.0842	-0.0519	0.0046	0.0160	0.0095	0.0113	
-0.303	-0.659	0.9971	-0.1451	1.0677	-0.0472	0.0030	0.0180	0.0103	0.0125	(-5)
-0.303	-0.879	0.9377	-0.1417	1.0375	-0.0550	0.0032	0.0349	0.0262	0.0227	(-5)
-0.151	0.879	0.9132	-0.1707	1.0410	-0.0148	0.0049	0.0473	0.0286	0.0265	(5)
-0.151	0.659	0.9937	-0.1859	1.0859	-0.0203	0.0076	0.0164	0.0089	0.0158	(5)
-0.151	0.440	1.0038	-0.1806	1.0880	-0.0251	-0.0009	0.0170	0.0087	0.0116	
-0.151	0.220	1.0009	-0.1766	1.0849	-0.0218	-0.0036	0.0159	0.0110	0.0114	
-0.151	0.000	0.9980	-0.1722	1.0815	-0.0234	-0.0029	0.0175	0.0096	0.0128	
-0.151	-0.220	0.9964	-0.1862	1.0871	-0.0282	0.0040	0.0164	0.0120	0.0106	
-0.151	-0.440	0.9988	-0.1910	1.0903	-0.0305	0.0078	0.0167	0.0089	0.0116	
-0.151	-0.659	0.9952	-0.1685	1.0783	-0.0299	0.0089	0.0174	0.0094	0.0123	(-5)
-0.151	-0.879	0.9605	-0.1863	1.0702	-0.0378	0.0038	0.0284	0.0214	0.0193	(-5)
0.000	0.879	0.9299	-0.2103	1.0678	0.0022	-0.0016	0.0294	0.0198	0.0245	(5)
0.000	0.659	0.9854	-0.2045	1.0908	0.0023	-0.0054	0.0163	0.0091	0.0166	(5)
0.000	0.440	1.0050	-0.1886	1.0925	-0.0017	-0.0043	0.0169	0.0079	0.0120	
0.000	0.220	1.0039	-0.1814	1.0887	0.0011	0.0076	0.0163	0.0103	0.0110	
0.000	0.000	0.9925	-0.1835	1.0844	0.0092	0.0046	0.0173	0.0104	0.0122	
0.000	-0.220	0.9997	-0.2088	1.0993	0.0015	0.0103	0.0180	0.0094	0.0108	
0.000	-0.440	0.9982	-0.2061	1.0973	-0.0129	0.0099	0.0185	0.0150	0.0117	
0.000	-0.659	0.9954	-0.2215	1.1031	-0.0094	0.0059	0.0168	0.0098	0.0125	(-5)
0.000	-0.879	0.9491	-0.1519	1.0492	-0.0114	0.0031	0.0288	0.0193	0.0180	(-5)
0.076	0.000	1.0034	-0.1802	1.0878	0.0165	0.0045	0.0169	0.0108	0.0128	
0.076	-0.220	0.9778	-0.2246	1.0964	0.0150	0.0091	0.0176	0.0095	0.0125	
0.076	-0.440	0.9500	-0.2542	1.0973	-0.0012	0.0096	0.0205	0.0137	0.0132	
0.076	-0.659	0.9492	-0.2848	1.1108	0.0012	0.0090	0.0197	0.0111	0.0155	
0.076	-0.879	0.7019	-0.4643	1.0799	0.0052	0.0058	0.0411	0.0204	0.0237	(-6)
0.151	0.879	0.9740	-0.1454	1.0578	0.0205	0.0004	0.0345	0.0222	0.0206	(5)
0.151	0.659	0.9896	-0.1866	1.0843	0.0220	-0.0023	0.0174	0.0101	0.0125	(5)
0.151	0.440	0.9971	-0.1870	1.0880	0.0187	-0.0029	0.0178	0.0085	0.0123	
0.151	0.220	1.0023	-0.1740	1.0844	0.0197	0.0005	0.0156	0.0113	0.0116	
0.151	0.000	1.0083	-2.3414	1.0830	0.0287	-0.0007	0.0163	0.0105	0.0148	
0.151	-0.220	1.0081	-0.1841	1.0915	0.0275	0.0068	0.0170	0.0101	0.0108	
0.151	-0.440	0.9933	-0.2075	1.0957	0.0124	0.0118	0.0164	0.0138	0.0115	
0.151	-0.659	0.9921	-0.2387	1.1092	0.0173	0.0109	0.0183	0.0097	0.0140	(-5)
0.151	-0.879	0.8288	-0.3146	1.0691	0.0178	0.0122	0.0432	0.0225	0.0296	(-5)

TABLE IIIa
AR310 EXIT PLANE DATA (CONTINUED)

y/S	z/H	$(P - P_{ref})/Q_{ref}$	$(p - P_{ref})/Q_{ref}$	U/U_{ref}	V/U_{ref}	W/U_{ref}	$\sqrt{\overline{u^2}}/U_{ref}$	$\sqrt{\overline{v^2}}/U_{ref}$	$\sqrt{\overline{w^2}}/U_{ref}$
0.227	0.000	1.0038	-0.1653	1.0806	0.0370	0.0001	0.0157	0.0114	0.0128
0.227	-0.220	1.0161	-0.1764	1.0914	0.0369	0.0042	0.0160	0.0102	0.0119
0.227	-0.440	0.9943	-0.1959	1.0907	0.0233	0.0075	0.0168	0.0169	0.0123
0.227	-0.659	0.9913	-0.2268	1.1032	0.0316	0.0085	0.0192	0.0102	0.0161
0.227	-0.879	0.8761	-0.2633	1.0669	0.0312	0.0109	0.0405	0.0215	0.0325 (-6)
0.303	0.879	0.9612	-0.1261	1.0420	0.0388	0.0015	0.0357	0.0234	0.0208 (5)
0.303	0.659	0.9966	-0.1623	1.0759	0.0362	-0.0018	0.0159	0.0099	0.0131 (5)
0.303	0.440	0.9999	-0.1700	1.0809	0.0383	-0.0055	0.0169	0.0096	0.0114
0.303	0.220	1.0014	-0.1513	1.0730	0.0373	-0.0060	0.0154	0.0125	0.0112
0.303	0.000	0.9974	-0.1541	1.0722	0.0431	-0.0072	0.0179	0.0120	0.0124
0.303	-0.220	1.0133	-0.1653	1.0846	0.0468	0.0017	0.0164	0.0103	0.0102
0.303	-0.440	1.0036	-0.1728	1.0841	0.0332	0.0078	0.0187	0.0127	0.0115
0.303	-0.659	0.9931	-0.2150	1.0983	0.0424	0.0090	0.0182	0.0110	0.0127 (-5)
0.303	-0.879	0.9232	-0.2219	1.0690	0.0478	0.0088	0.0349	0.0207	0.0260 (-5)
0.379	0.000	0.9984	-0.1447	1.0679	0.0515	-0.0066	0.0152	0.0116	0.0117
0.379	-0.220	1.0053	-0.1531	1.0749	0.0547	-0.0013	0.0152	0.0107	0.0116
0.379	-0.440	1.0044	-0.1566	1.0766	0.0438	0.0039	0.0159	0.0131	0.0124
0.379	-0.659	0.9894	-0.2048	1.0916	0.0511	0.0041	0.0173	0.0110	0.0148
0.379	-0.879	0.9387	-0.1803	1.0560	0.0626	0.0053	0.0393	0.0227	0.0234 (-6)
0.454	0.879	0.9189	-0.1103	1.0130	0.0550	-0.0012	0.0454	0.0304	0.0276 (5)
0.454	0.659	1.0018	-0.1214	1.0587	0.0484	-0.0063	0.0153	0.0105	0.0137 (5)
0.454	0.440	1.0071	-0.1264	1.0633	0.0530	-0.0075	0.0158	0.0096	0.0116
0.454	0.220	1.0077	-0.1084	1.0551	0.0538	-0.0043	0.0158	0.0144	0.0106
0.454	0.000	1.0017	-0.1213	1.0581	0.0591	-0.0032	0.0160	0.0115	0.0118
0.454	-0.220	1.0098	-0.1234	1.0628	0.0604	0.0014	0.0149	0.0112	0.0104
0.454	-0.440	1.0097	-0.1311	1.0669	0.0503	0.0041	0.0169	0.0135	0.0110
0.454	-0.659	0.9946	-0.1764	1.0804	0.0611	0.0041	0.0169	0.0105	0.0123 (-5)
0.454	-0.879	0.9265	-0.1708	1.0450	0.0721	0.0063	0.0434	0.0258	0.0231 (-5)
0.530	0.000	1.0066	-0.0954	1.0477	0.0655	-0.0010	0.0148	0.0117	0.0115
0.530	-0.220	1.0037	-0.1050	1.0508	0.0673	0.0033	0.0154	0.0109	0.0111
0.530	-0.440	1.0064	-0.1087	1.0545	0.0556	0.0043	0.0162	0.0144	0.0118
0.530	-0.659	0.9944	-0.1509	1.0680	0.0683	0.0048	0.0165	0.0117	0.0149
0.530	-0.879	0.9346	-0.1384	1.0327	0.0808	0.0054	0.0418	0.0275	0.0247 (-6)
0.606	0.879	0.9033	-0.0697	0.9844	0.0624	0.0019	0.0474	0.0314	0.0296 (5)
0.606	0.659	1.0032	-0.0586	1.0291	0.0529	-0.0001	0.0183	0.0121	0.0138 (5)
0.606	0.440	1.0189	-0.0698	1.0417	0.0590	-0.0037	0.0159	0.0105	0.0115
0.606	0.220	1.0149	-0.0580	1.0338	0.0645	-0.0027	0.0152	0.0148	0.0108
0.606	0.000	1.0028	-0.0731	1.0349	0.0701	-0.0010	0.0149	0.0126	0.0126
0.606	-0.220	0.9975	-0.0832	1.0371	0.0712	0.0051	0.0157	0.0119	0.0106
0.606	-0.440	1.0047	-0.0825	1.0409	0.0602	0.0081	0.0170	0.0155	0.0112
0.606	-0.659	0.9888	-0.1157	1.0485	0.0707	0.0091	0.0190	0.0130	0.0146 (-5)
0.606	-0.879	0.9278	-0.1140	1.0170	0.0858	0.0082	0.0413	0.0274	0.0266 (-5)
0.681	0.000	1.0076	-0.0364	1.0194	0.0698	0.0034	0.0152	0.0150	0.0112
0.681	-0.220	0.9995	-0.0545	1.0243	0.0693	0.0043	0.0163	0.0126	0.0113
0.681	-0.440	0.9944	-0.0670	1.0285	0.0601	0.0056	0.0160	0.0161	0.0128
0.681	-0.659	0.9795	-0.0900	1.0317	0.0709	0.0094	0.0204	0.0155	0.0180
0.681	-0.879	0.8984	-0.0978	0.9942	0.0872	0.0123	0.0418	0.0310	0.0313 (-6)
0.757	0.879	0.8469	0.0186	0.9076	0.0668	-0.0056	0.0561	0.0412	0.0383 (5)
0.757	0.659	1.0079	0.0030	1.0005	0.0624	0.0040	0.0205	0.0154	0.0177 (5)
0.757	0.440	1.0191	0.0393	0.9883	0.0546	0.0094	0.0235	0.0164	0.0133
0.757	0.220	1.0140	0.0227	0.9927	0.0756	0.0099	0.0210	0.0207	0.0114
0.757	0.000	1.0025	0.0158	0.9916	0.0585	0.0042	0 0226	0.0203	0.0126
0.757	-0.220	0.9928	-0.0335	1.0110	0.0645	0.0073	0.0162	0.0136	0.0129
0.757	-0.440	0.9823	-0.0420	1.0103	0.0590	0.0085	0.0178	0.0148	0.0147
0.757	-0.549	0.9886	-0.0414	1.0129	0.0628	0.0065	0.0193	0.0178	0.0180
0.757	-0.659	0.9686	-0.0578	1.0107	0.0698	0.0090	0.0214	0.0200	0.0191 (-5)
0.757	-0.769	0.9368	-0.0666	0.9986	0.0777	0.0136	0.0269	0.0209	0.0256
0.757	-0.879	0.8354	-0.0854	0.9552	0.0884	0.0244	0.0473	0.0358	0.0367 (-5)
0.795	-0.440	0.9726	-0.0380	1.0037	0.0560	0.0018	0.0180	0.0160	0.0190
0.795	-0.549	0.9758	-0.0349	1.0034	0.0623	0.0022	0.0198	0.0184	0.0206
0.795	-0.659	0.9714	-0.0296	0.9979	0.0715	0.0046	0.0234	0.0185	0.0213
0.795	-0.769	0.9097	-0.0622	0.9824	0.0809	0.0135	0.0312	0.0239	0.0313
0.795	-0.879	0.7877	-0.0924	0.9333	0.0908	0.0290	0.0500	0.0497	0.0447 (-6)
0.833	0.000	1.0034	0.0596	0.9699	0.0550	0.0010	0.0291	0.0189	0.0155
0.833	-0.220	0.9778	-0.0269	1.0006	0.0590	0.0004	0.0176	0.0139	0.0190
0.833	-0.440	0.9500	-0.0437	0.9953	0.0550	-0.0027	0.0188	0.0164	0.0216
0.833	-0.549	0.9580	-0.0302	0.9923	0.0590	-0.0058	0.0214	0.0220	0.0227
0.833	-0.659	0.9492	-0.0250	0.9843	0.0729	-0.0019	0.0259	0.0196	0.0247
0.833	-0.769	0.8657	-0.0631	0.9595	0.0894	0.0142	0.0397	0.0275	0.0391
0.833	-0.879	0.7019	-0.0967	0.8884	0.0896	0.0371	0.0665	0.0608	0.0588 (-6)
0.871	-0.440	0.9230	-0.0401	0.9802	0.0465	-0.0085	0.0242	0.0212	0.0266
0.871	-0.549	0.9258	-0.0218	0.9717	0.0564	-0.0156	0.0278	0.0249	0.0283
0.871	-0.659	0.9000	-0.0272	0.9600	0.0746	-0.0014	0.0335	0.0264	0.0339
0.871	-0.769	0.8073	-0.0583	0.9249	0.1007	0.0059	0.0473	0.0368	0.0461
0.871	-0.879	0.5402	-0.0740	0.7762	0.1004	0.0401	0.1347	0.0737	0.0799 (-6)

87-9-19-56

TABLE IIIa
AR310 EXIT PLANE DATA (CONCLUDED)

y/S	z/H	$(P - p_{ref})/Q_{ref}$	$(p - p_{ref})/Q_{ref}$	U/U_{ref}	V/U_{ref}	W/U_{ref}	$\sqrt{\overline{u^2}}/U_{ref}$	$\sqrt{\overline{v^2}}/U_{ref}$	$\sqrt{\overline{w^2}}/U_{ref}$	
0.908	0.879	0.5653	0.1619	0.6256	0.1040	0.0335	0.1330	0.0906	0.0754	(5)
0.908	0.659	0.9157	0.1832	0.8531	0.0601	0.0335	0.0504	0.0406	0.0388	(5)
0.908	0.440	0.9355	0.1934	0.8610	0.0251	0.0130	0.0548	0.0407	0.0325	
0.908	0.220	1.0119	0.1544	0.9252	0.0390	-0.0008	0.0361	0.0275	0.0277	
0.908	0.000	0.9622	0.0432	0.9573	0.0503	-0.0065	0.0364	0.0224	0.0249	
0.908	-0.220	0.9256	-0.0016	0.9617	0.0481	-0.0075	0.0321	0.0261	0.0302	
0.908	-0.440	0.8140	-0.0312	0.9186	0.0364	-0.0069	0.0462	0.0356	0.0419	
0.908	-0.549	0.8084	-0.0140	0.9056	0.0451	-0.0160	0.0457	0.0369	0.0433	
0.908	-0.659	0.8023	-0.0162	0.9019	0.0681	-0.0211	0.0464	0.0377	0.0450	(-5)
0.908	-0.769	0.7365	-0.0549	0.8821	0.1139	-0.0170	0.0524	0.0423	0.0529	
0.908	-0.879	0.4205	-0.0002	0.6379	0.1176	0.0020	0.1498	0.0821	0.0837	(-5)
0.946	-0.440	0.6097	0.0752	0.7307	0.0253	-0.0040	0.1102	0.0624	0.0681	
0.946	-0.549	0.5824	0.0392	0.7363	0.0317	-0.0067	0.1067	0.0561	0.0667	
0.946	-0.659	0.6192	-0.0094	0.7906	0.0565	-0.0194	0.0778	0.0495	0.0620	
0.946	-0.769	0.6475	-0.0259	0.8136	0.1009	-0.0358	0.0633	0.0513	0.0601	
0.946	-0.879	0.4423	0.0402	0.6243	0.0963	-0.0550	0.1210	0.0833	0.0780	(-6)

87-9-19-57

TABLE IIIb
AR630 EXIT PLANE DATA

y/S	z/H	$(P - P_{ref})/Q_{ref}$	$(p - p_{ref})/Q_{ref}$	U/U_{ref}	V/U_{ref}	W/U_{ref}	$\sqrt{\overline{u^2}}/U_{ref}$	$\sqrt{\overline{v^2}}/U_{ref}$	$\sqrt{\overline{w^2}}/U_{ref}$
-0.750	0.823	0.7501	-0.1669	0.9560	-0.0510	0.0200	0.0465	-	0.0332 (3.4)
-0.750	0.732	0.8700	-0.1076	0.9860	-0.0691	0.0254	0.0391	-	0.0250 (3.4)
-0.750	0.549	0.9726	-0.0441	1.0060	-0.0644	0.0232	0.0312	-	0.0192 (3.4)
-0.750	0.366	0.9955	-0.0185	1.0050	-0.0597	0.0199	0.0301	-	0.0177 (3.4)
-0.750	0.183	0.9966	-0.0119	1.0040	-0.0221	0.0012	0.0323	-	0.0186
-0.750	0.000	0.9962	-0.0102	1.0030	-0.0199	-0.0008	0.0304	-	0.0199
-0.750	-0.183	0.9922	-0.0245	1.0080	-0.0224	-0.0126	0.0316	-	0.0183
-0.750	-0.366	0.9948	-0.0240	1.0090	-0.0223	-0.0144	0.0306	-	0.0163 (-2.9)
-0.750	-0.549	0.9883	-0.0226	1.0050	-0.0247	-0.0146	0.0337	-	0.0188 (-2.9)
-0.750	-0.732	0.9269	-0.0161	0.9710	-0.0083	-0.0102	0.0438	-	0.0292 (-2.9)
-0.750	-0.823	0.8443	-	0.9230	-	-0.0087	0.0543	-	0.0375 (-2.9)
-0.500	0.823	0.8098	-0.1626	0.9860	-0.0132	0.0048	0.0562	0.0388	0.0325 (3.4)
-0.500	0.732	0.9374	-0.1285	1.0320	-0.0290	0.0042	0.0367	0.0200	0.0230 (3.4)
-0.500	0.549	0.9952	-0.1041	1.0480	-0.0315	0.0032	0.0285	0.0076	0.0163 (3.4)
-0.500	0.366	0.9996	-0.1082	1.0520	-0.0337	0.0021	0.0271	0.0063	0.0148 (3.4)
-0.500	0.183	0.9968	-0.0963	1.0450	-0.0323	0.0009	0.0276	0.0060	0.0148
-0.500	0.000	1.0000	-0.1057	1.0510	-0.0318	0.0021	0.0280	0.0063	0.0147
-0.500	-0.183	0.9975	-0.1103	1.0520	-0.0320	0.0013	0.0302	0.0062	0.0150
-0.500	-0.366	0.9963	-0.1073	1.0500	-0.0320	0.0025	0.0291	0.0067	0.0156 (-2.9)
-0.500	-0.549	0.9970	-0.1067	1.0500	-0.0353	0.0024	0.0314	0.0083	0.0171 (-2.9)
-0.500	-0.732	0.9439	-0.1389	1.0400	-0.0342	-0.0005	0.0354	0.0195	0.0244 (-2.9)
-0.500	-0.823	0.8633	-0.1734	1.0180	-0.0176	0.0017	0.0468	0.0331	0.0324 (-2.9)
-0.250	0.823	0.8151	-0.2071	1.0110	-0.0080	0.0028	0.0480	0.0327	0.0319 (3.4)
-0.250	0.732	0.9298	-0.1709	1.0490	-0.0162	0.0019	0.0334	0.0156	0.0239 (3.4)
-0.250	0.549	0.9957	-0.1261	1.0590	-0.0177	0.0004	0.0282	0.0069	0.0191 (3.4)
-0.250	0.366	0.9999	-0.1283	1.0620	-0.0173	-0.0049	0.0268	0.0052	0.0205
-0.250	0.183	0.9967	-0.1230	1.0580	-0.0195	0.0007	0.0273	0.0057	0.0144
-0.250	0.000	0.9981	-0.1322	1.0630	-0.0178	0.0014	0.0263	0.0055	0.0138
-0.250	-0.183	0.9994	-0.1246	1.0600	-0.0184	0.0022	0.0285	0.0053	0.0163
-0.250	-0.366	1.0014	-0.1247	1.0610	-0.0202	-0.0004	0.0286	0.0056	0.0158
-0.250	-0.549	0.9991	-0.1228	1.0590	-0.0199	0.0002	0.0297	0.0067	0.0160 (-2.9)
-0.250	-0.732	0.9750	-0.1258	1.0490	-0.0192	-0.0013	0.0340	0.0154	0.0197 (-2.9)
-0.250	-0.823	0.9232	-0.1461	1.0340	-0.0115	-0.0009	0.0440	0.0259	0.0255 (-2.9)
0.000	0.823	0.8760	-0.1422	1.0090	0.0000	0.0069	0.0473	0.0276	0.0230 (6.3)
0.000	0.732	0.9613	-0.1287	1.0440	-0.0020	0.0044	0.0317	0.0126	0.0129 (6.4)
0.000	0.549	0.9941	-0.1253	1.0580	-0.0026	0.0066	0.0261	0.0056	0.0122 (6.1)
0.000	0.366	0.9985	-0.1167	1.0560	-0.0026	0.0062	0.0287	0.0050	0.0101 (3.1)
0.000	0.183	0.9979	-0.1194	1.0570	-0.0020	0.0048	0.0249	0.0048	0.0079 (2.0)
0.000	0.000	0.9976	-0.1175	1.0560	-0.0025	0.0036	0.0249	0.0048	0.0057
0.000	-0.183	0.9993	-0.1159	1.0560	-0.0027	0.0014	0.0265	0.0049	0.0067 (-1.5)
0.000	-0.366	0.9980	-0.1172	1.0560	-0.0046	0.0007	0.0271	0.0050	0.0075 (-3.6)
0.000	-0.549	0.9989	-0.1162	1.0560	-0.0036	0.0000	0.0268	0.0056	0.0080 (-5.0)
0.000	-0.732	0.9783	-0.1411	1.0580	-0.0036	-0.0022	0.0329	0.0116	0.0143 (-6.5)
0.000	-0.823	0.9109	-0.1707	1.0400	-0.0017	-0.0024	0.0371	0.0240	0.0270 (-8.2)
0.125	0.823	0.8720	-0.1563	1.0140	0.0085	0.0060	0.0447	0.0285	0.0243 (6.3)
0.125	0.732	0.9737	-0.1184	1.0450	0.0067	0.0035	0.0330	0.0147	0.0126 (6.4)
0.125	0.549	0.9989	-0.1142	1.0550	0.0071	0.0051	0.0274	0.0066	0.0124 (6.1)
0.125	0.366	1.0018	-0.1177	1.0580	0.0088	0.0059	0.0275	0.0056	0.0098 (3.1)
0.125	0.183	1.0017	-0.1156	1.0570	0.0091	0.0041	0.0256	0.0055	0.0070 (2.0)
0.125	0.000	1.0009	-0.1206	1.0590	0.0078	0.0007	0.0277	0.0055	0.0057
0.125	-0.183	1.0044	-0.1192	1.0600	0.0078	0.0017	0.0264	0.0054	0.0055
0.125	-0.366	1.0024	-0.1233	1.0610	0.0046	0.0013	0.0271	0.0053	0.0075 (-3.6)
0.125	-0.549	1.0044	-0.1149	1.0580	0.0039	0.0008	0.0270	0.0064	0.0078 (-5.0)
0.125	-0.732	0.9783	-0.1305	1.0530	0.0057	0.0001	0.0316	0.0141	0.0154 (-6.5)
0.125	-0.823	0.8945	-0.1809	1.0370	0.0056	-0.0007	0.0394	0.0276	0.0276 (-8.2)
0.250	0.823	0.8848	-0.1538	1.0190	0.0142	0.0047	0.0469	0.0293	0.0249 (6.3)
0.250	0.732	0.9704	-0.1239	1.0460	0.0135	-0.0015	0.0382	0.0161	0.0121 (6.4)
0.250	0.549	1.0032	-0.1079	1.0540	0.0138	-0.0027	0.0324	0.0077	0.0089 (6.1)
0.250	0.366	1.0039	-0.1116	1.0560	0.0162	-0.0034	0.0301	0.0067	0.0091 (3.1)
0.250	0.183	1.0006	-0.1360	1.0660	0.0156	-0.0036	0.0465	0.0064	0.0058
0.250	0.000	1.0004	-0.1151	1.0560	0.0189	-0.0037	0.0322	0.0064	0.0055
0.250	-0.183	1.0033	-0.1185	1.0590	0.0192	-0.0016	0.0321	0.0064	0.0058
0.250	-0.366	1.0039	-0.1157	1.0580	0.0167	-0.0007	0.0377	0.0065	0.0081 (-3.6)
0.250	-0.549	1.0062	-0.1113	1.0570	0.0162	-0.0001	0.0324	0.0074	0.0089 (-5.0)
0.250	-0.732	0.9805	-0.1222	1.0500	0.0160	-0.0002	0.0363	0.0141	0.0194 (-6.5)
0.250	-0.823	0.9029	-0.1726	1.0370	0.0141	-0.0012	0.0433	0.0265	0.0316 (-8.2)
0.375	0.823	0.8725	-0.1601	1.0160	0.0191	0.0042	0.0469	0.0276	0.0277 (6.3)
0.375	0.732	0.9669	-0.1172	1.0410	0.0201	-0.0020	0.0357	0.0166	0.0148 (6.4)
0.375	0.549	1.0021	-0.1009	1.0500	0.0208	-0.0015	0.0335	0.0078	0.0079 (6.1)
0.375	0.366	0.9984	-0.1025	1.0490	0.0215	-0.0030	0.0319	0.0073	0.0070 (3.1)
0.375	0.183	0.9934	-0.1013	1.0460	0.0242	-0.0030	0.0305	0.0083	0.0055
0.375	0.000	0.9959	-0.1223	1.0570	0.0315	-0.0030	0.0418	0.0083	0.0057
0.375	-0.183	1.0006	-0.1069	1.0520	0.0274	-0.0018	0.0350	0.0079	0.0055
0.375	-0.366	1.0010	-0.1063	1.0520	0.0243	-0.0029	0.0290	0.0073	0.0083 (-3.6)
0.375	-0.549	1.0041	-0.1074	1.0540	0.0241	-0.0015	0.0286	0.0082	0.0086 (-5.0)
0.375	-0.732	0.9751	-0.1196	1.0460	0.0246	-0.0009	0.0337	0.0170	0.0188 (-6.5)
0.375	-0.823	0.8957	-0.1573	1.0260	0.0185	0.0003	0.0456	0.0290	0.0324 (-8.2)

TABLE IIIb
AR630 EXIT PLANE DATA (CONTINUED)

y/S	z/H	$(P - P_{ref})/Q_{ref}$	$(p - p_{ref})/Q_{ref}$	U/U_{ref}	V/U_{ref}	W/U_{ref}	$\sqrt{\overline{u^2}}/U_{ref}$	$\sqrt{\overline{v^2}}/U_{ref}$	$\sqrt{\overline{w^2}}/U_{ref}$
0.500	0.823	0.8694	-0.1373	1.0030	0.0252	0.0064	0.0468	0.0309	0.0310 (6.3)
0.500	0.732	0.9585	-0.1074	1.0320	0.0289	0.0010	0.0340	0.0164	0.0174 (6.4)
0.500	0.549	1.0007	-0.0879	1.0430	0.0287	-0.0008	0.0276	0.0083	0.0084 (6.1)
0.500	0.366	0.9979	-0.0909	1.0430	0.0298	-0.0006	0.0273	0.0078	0.0062
0.500	0.183	0.9932	-0.0977	1.0440	0.0315	-0.0012	0.0375	0.0087	0.0054
0.500	0.000	0.9933	-0.0894	1.0400	0.0330	-0.0017	0.0327	0.0092	0.0054
0.500	-0.183	0.9966	-0.0922	1.0430	0.0306	-0.0011	0.0276	0.0090	0.0056
0.500	-0.366	0.9982	-0.0844	1.0400	0.0304	-0.0013	0.0280	0.0072	0.0063
0.500	-0.549	1.0026	-0.0967	1.0480	0.0324	-0.0020	0.0270	0.0086	0.0087 (-5.0)
0.500	-0.732	0.9793	-0.0971	1.0370	0.0323	-0.0019	0.0314	0.0196	0.0191 (-6.5)
0.500	-0.823	0.8918	-0.1369	1.0140	0.0222	-0.0013	0.0442	0.0313	0.0333 (-8.2)
0.625	0.823	0.8520	-0.1211	0.9850	0.0530	0.0104	0.0547	0.0334	0.0330 (6.3)
0.625	0.732	0.9530	-0.0825	1.0170	0.0333	0.0093	0.0399	0.0202	0.0237 (6.3)
0.625	0.549	0.9985	-0.0822	1.0390	0.0334	0.0017	0.0307	0.0089	0.0087 (6.4)
0.625	0.366	0.9930	-0.0813	1.0360	0.0316	0.0015	0.0304	0.0089	0.0066
0.625	0.183	0.9914	-0.0787	1.0340	0.0295	0.0005	0.0291	0.0088	0.0056
0.625	0.000	0.9923	-0.0841	1.0370	0.0309	-0.0012	0.0286	0.0081	0.0057
0.625	-0.183	0.9936	-0.0808	1.0360	0.0338	-0.0020	0.0289	0.0077	0.0054
0.625	-0.366	1.0009	-0.0841	1.0410	0.0364	-0.0029	0.0298	0.0075	0.0064
0.625	-0.549	1.0026	-0.0806	1.0400	0.0398	-0.0035	0.0319	0.0085	0.0090 (-5.0)
0.625	-0.732	0.9583	-0.1064	1.0310	0.0414	-0.0017	0.0352	0.0212	0.0192 (-6.5)
0.625	-0.823	0.8542	-0.1526	1.0030	0.0278	0.0039	0.0482	0.0340	0.0345 (-8.2)
0.750	0.823	0.8336	-0.1143	0.9730	0.0292	0.0174	0.0537	0.0345	-
0.750	0.732	0.9238	-0.0821	1.0020	0.0351	0.0254	0.0434	0.0233	0.0269 (6.3)
0.750	0.549	0.9856	-0.0619	1.0230	0.0268	0.0160	0.0330	0.0121	0.0105 (6.4)
0.750	0.366	0.9878	-0.0655	1.0260	0.0198	0.0144	0.0302	0.0103	0.0083
0.750	0.183	0.9921	-0.0650	1.0280	0.0175	0.0062	0.0301	0.0097	0.0073
0.750	0.000	0.9973	-0.0620	1.0290	0.0215	-0.0021	0.0312	0.0086	0.0072
0.750	-0.183	0.9997	-0.0703	1.0340	0.0281	-0.0080	0.0321	0.0083	0.0081
0.750	-0.366	0.9992	-0.0652	1.0310	0.0362	-0.0122	0.0314	0.0081	0.0100
0.750	-0.549	0.9909	-0.0815	1.0340	0.0476	-0.0315	0.0335	0.0114	0.0190 (-5.0)
0.750	-0.732	0.9256	-0.1076	1.0150	0.0546	-0.0056	0.0403	0.0265	0.0235 (-6.5)
0.750	-0.823	0.8177	-0.1445	0.9800	0.0429	0.0026	0.0530	0.0373	-
0.800	0.823	0.8179	-0.1092	0.9620	0.0313	0.0245	0.0532	0.0352	-
0.800	0.732	0.8879	-0.1041	0.9950	0.0355	0.0262	0.0501	0.0261	-
0.800	0.549	0.9281	-0.0833	1.0050	0.0225	0.0301	0.0449	0.0199	0.0182
0.800	0.366	0.9124	-0.1064	1.0090	0.0084	0.0252	0.0481	0.0196	0.0195
0.800	0.183	0.9307	-0.0977	1.0140	0.0039	0.0152	0.0482	0.0199	0.0235
0.800	0.000	0.9375	-0.1029	1.0200	0.0068	-0.0022	0.0438	0.0198	0.0249
0.800	-0.183	0.9623	-0.1054	1.0330	0.0193	-0.0163	0.0423	0.0163	0.0239
0.800	-0.366	0.9774	-0.0956	1.0350	0.0361	-0.0221	0.0377	0.0133	0.0209
0.800	-0.549	0.9699	-0.0884	1.0260	0.0555	-0.0504	0.0424	0.0152	0.0253
0.800	-0.732	0.9141	-0.1156	1.0120	0.0734	-0.0100	0.0476	0.0249	0.0272 (-6.5)
0.800	-0.823	0.8153	-0.1662	0.9890	0.0585	-0.0013	0.0569	0.0383	-
0.850	0.823	0.7546	-0.0631	0.9030	0.0402	0.0261	0.0591	0.0348	-
0.850	0.732	0.8256	-0.0534	0.9370	0.0045	0.0313	0.0482	0.0274	-
0.850	0.549	0.7799	-0.0599	0.9150	0.0230	0.0453	0.0509	0.0300	0.0376
0.850	0.366	0.5848	-0.1498	0.8560	-0.0007	0.0432	0.0799	0.0387	0.0453
0.850	0.183	0.5738	-0.0485	0.7880	-0.0179	0.0316	0.1095	0.0481	0.0501
0.850	0.000	0.5473	-0.0662	0.7830	-0.0183	0.0092	0.1108	0.0495	0.0508
0.850	-0.183	0.6122	-0.1328	0.8630	0.0044	-0.0173	0.0893	0.0440	0.0478
0.850	-0.366	0.7563	-0.1312	0.9410	0.0374	-0.0252	0.0589	0.0323	0.0427
0.850	-0.549	0.8541	-0.1077	0.9780	0.0696	-0.0209	0.0469	0.0260	0.0337
0.850	-0.732	0.8644	-0.0886	0.9710	0.1008	-0.0009	0.0475	0.0279	-
0.850	-0.823	0.7897	-0.1074	0.9410	0.1075	0.0100	0.0561	0.0357	-
0.900	0.823	0.6354	-0.0934	0.8520	0.0490	0.0219	0.0645	0.0586 (9)	-
0.900	0.732	0.7205	-0.0646	0.8820	0.0822	0.0219	0.0504	0.0405 (9)	-
0.900	0.549	0.6295	-0.0390	0.8140	0.0699	0.0323	0.0781	0.0398 (9)	0.0417
0.900	0.366	0.4455	0.0083	0.6600	-0.0185	0.0352	0.0869	0.0511 (-10)	0.0468
0.900	0.183	0.3279	-0.0208	0.5860	-0.0656	0.0309	0.0637	0.0554 (-10)	0.0447
0.900	0.000	0.2979	-0.0485	0.5820	-0.0876	0.0014	0.0595	0.0516 (-10)	0.0434
0.900	-0.183	0.3487	-0.0964	0.6660	-0.0387	-0.0074	0.0832	0.0483 (-10)	0.0447
0.900	-0.366	0.5122	-0.1701	0.8260	0.0037	-0.0018	0.0853	0.0475 (-10)	0.0431
0.900	-0.549	0.7088	-0.1353	0.9180	0.0363	0.0039	0.0748	0.0356 (-10)	0.0378
0.900	-0.732	0.7702	0.1215	0.8040	0.0431	-0.0214	0.0864	0.0342 (-10)	-
0.900	-0.823	0.6830	0.3001	0.6180	0.0294	-0.0114	0.0981	0.0485 (-10)	-
0.950	0.823	0.4602	-	-	-	-	-	-	-
0.950	0.732	0.5443	-	-	0.0150	0.0436	-	0.0603 (-10)	-
0.950	0.549	0.6100	-0.0883	0.8350	0.0209	-0.0237	0.0602	0.0433 (-10)	0.0366
0.950	0.366	0.5012	-0.0204	0.7210	-0.0221	-0.0355	0.0741	0.0427 (-10)	0.0402
0.950	0.183	0.3623	-0.0131	0.6070	-0.0820	-0.0134	0.0623	0.0486 (-10)	0.0538
0.950	0.000	0.3509	0.0341	0.5600	-0.0432	0.0364	0.0522	-	0.0503
0.950	-0.183	0.4594	0.1029	0.5940	0.0190	0.0573	0.0564	-	0.0361
0.950	-0.366	0.5655	0.0718	0.6970	0.0659	0.0589	0.0644	-	0.0325
0.950	-0.549	0.6516	-0.0148	0.8100	0.0939	0.0390	0.0560	-	0.0359
0.950	-0.732	0.5713	-	0.8150	-	-	0.0595	-	-
0.950	-0.823	0.5476	-	-	-	-	-	-	-

87-9-19-59

TABLE IVa
TOTAL PRESSURE BOUNDARY LAYER SURVEYS IN AR310 EXIT PLANE

SURVEY 1		SURVEY 2		SURVEY 3		SURVEY 4		SURVEY 5	
y_{bl}/H	$(P - p_{ref})/Q_{ref}$	y_{bl}/H	$(P - p_{ref})/Q_{ref}$	y_{bl}/H	$(P - p_{ref})/Q_{ref}$	y_{bl}/H	$(P - p_{ref})/Q_{ref}$	y_{bl}/H	$(P - p_{ref})/Q_{ref}$
0.0035	0.1529	0.0035	0.1988	0.0035	0.1862	0.0035	0.1311	0.0035	0.1023
0.0040	0.1579	0.0040	0.2009	0.0040	0.2016	0.0040	0.1392	0.0040	0.1181
0.0044	0.1721	0.0044	0.2215	0.0044	0.2087	0.0044	0.1721	0.0044	0.1226
0.0048	0.1889	0.0048	0.2268	0.0048	0.2230	0.0048	0.1865	0.0048	0.1614
0.0053	0.2047	0.0053	0.2476	0.0053	0.2307	0.0053	0.2056	0.0053	0.1704
0.0057	0.2137	0.0057	0.2513	0.0057	0.2371	0.0057	0.2210	0.0057	0.2042
0.0062	0.2243	0.0062	0.2654	0.0101	0.2989	0.0062	0.2328	0.0062	0.2094
0.0066	0.2330	0.0066	0.2668	0.0145	0.3125	0.0066	0.2371	0.0066	0.2273
0.0070	0.2396	0.0070	0.2778	0.0189	0.3281	0.0070	0.2454	0.0070	0.2385
0.0075	0.2568	0.0075	0.2818	0.0233	0.3355	0.0075	0.2454	0.0075	0.2516
0.0079	0.2584	0.0079	0.2896	0.0343	0.3547	0.0079	0.2625	0.0119	0.3141
0.0123	0.3188	0.0123	0.3427	0.0453	0.3693	0.0123	0.3085	0.0163	0.3853
0.0167	0.3805	0.0167	0.3854	0.0563	0.3889	0.0167	0.3529	0.0207	0.4394
0.0211	0.4453	0.0211	0.4292	0.0673	0.4067	0.0211	0.4039	0.0251	0.4823
0.0255	0.4910	0.0255	0.4699	0.0782	0.4307	0.0255	0.4479	0.0360	0.6232
0.0365	0.6237	0.0365	0.5817	0.0892	0.4535	0.0365	0.5381	0.0470	0.7490
0.0475	0.7635	0.0475	0.6853	0.1002	0.4753	0.0475	0.6335	0.0580	0.8497
0.0585	0.8353	0.0585	0.7664	0.1112	0.5082	0.0585	0.7208	0.0690	0.8879
0.0695	0.8793	0.0695	0.8163	0.1332	0.5478	0.0695	0.7750	0.0800	0.9143
0.0804	0.8995	0.0804	0.8497	0.1552	0.6069	0.0804	0.8176	0.0910	0.9265
0.0914	0.9149	0.0914	0.8802	0.1771	0.6989	0.0914	0.8448	0.1020	0.9450
0.1024	0.9227	0.1024	0.8985	0.1991	0.7509	0.1024	0.8756	0.1130	0.9563
0.1134	0.9352	0.1134	0.9107	0.2431	0.8030	0.1134	0.8978	0.1349	0.9726
0.1354	0.9535	0.1354	0.9397	0.2651	0.8853	0.1354	0.9372	0.1569	0.9743
0.1574	0.9638	0.1574	0.9619	0.3090	0.9403	0.1574	0.9499	0.1789	0.9769
0.1793	0.9783	0.1793	0.9725	0.3530	0.9604	0.1793	0.9746	0.2009	0.9759
0.2013	0.9795	0.2013	0.9794	0.3969	0.9730	0.2013	0.9790	0.2229	0.9762
0.2233	0.9848	0.2233	0.9878	0.4409	0.9750	0.2233	0.9902	0.3407	0.9854
0.2673	0.9924	0.2673	0.9937	0.5508	0.9867	0.2673	0.9922	0.5604	1.0050
0.3112	0.9954	0.3112	0.9964	0.6607	0.9873	0.3112	0.9968	0.7802	1.0040
0.3552	0.9991	0.3552	1.0027	0.7705	0.9906	0.3552	0.9912	1.0000	0.9925
0.3991	1.0015	0.3991	1.0002	0.8804	0.9942	0.3991	0.9909	1.2207	0.9997
0.4431	0.9977	0.4431	1.0079	0.9903	0.9968	0.4431	0.9944		
0.5530	1.0001	0.5530	1.0058	1.3200	1.0007	0.5530	0.9942		
0.6629	0.9942	0.6629	1.0026	1.7596	0.9956	0.6629	0.9945		
0.7727	0.9889	0.7727	0.9988	2.1991	0.9928	0.7727	0.9957		
0.8826	0.9983	0.8826	1.0046	2.6387	0.9937	0.8826	1.0000		
0.9925	0.9951	0.9925	1.0056			0.9925	0.9920		

87 - 9 - 19 - 60

TABLE IVa
TOTAL PRESSURE BOUNDARY LAYER SURVEYS IN AR310 EXIT PLANE (CONTINUED)

SURVEY 6		SURVEY 7		SURVEY 8		SURVEY 9		SURVEY 10	
y_{bl}/H	$(P - P_{ref})/Q_{ref}$	y_{bl}/H	$(P - P_{ref})/Q_{ref}$	y_{bl}/H	$(P - P_{ref})/Q_{ref}$	y_{bl}/H	$(P - P_{ref})/Q_{ref}$	y_{bl}/H	$(P - P_{ref})/Q_{ref}$
0.0035	0.1028	0.0035	0.2167	0.0035	0.1733	0.0035	0.2040	0.0035	0.1856
0.0040	0.1181	0.0040	0.2291	0.0040	0.1775	0.0040	0.2094	0.0040	0.1977
0.0044	0.1200	0.0044	0.2526	0.0044	0.2027	0.0044	0.2327	0.0044	0.2100
0.0048	0.1345	0.0048	0.2628	0.0048	0.2171	0.0048	0.2390	0.0048	0.2248
0.0053	0.1667	0.0053	0.2827	0.0053	0.2291	0.0053	0.2537	0.0053	0.2400
0.0057	0.1816	0.0057	0.2864	0.0057	0.2315	0.0057	0.2541	0.0057	0.2569
0.0062	0.1885	0.0062	0.2971	0.0062	0.2432	0.0062	0.2650	0.0062	0.2631
0.0066	0.2135	0.0066	0.3111	0.0066	0.2559	0.0066	0.2717	0.0066	0.2662
0.0070	0.2232	0.0070	0.3108	0.0070	0.2548	0.0070	0.2716	0.0070	0.2757
0.0075	0.2267	0.0075	0.3107	0.0075	0.2593	0.0075	0.2800	0.0075	0.2881
0.0119	0.2794	0.0079	0.3110	0.0079	0.2671	0.0079	0.2841	0.0079	0.2902
0.0163	0.3229	0.0123	0.3415	0.0123	0.2953	0.0123	0.3137	0.0123	0.3449
0.0207	0.3733	0.0167	0.3709	0.0167	0.3064	0.0167	0.3234	0.0167	0.3874
0.0251	0.4151	0.0211	0.3732	0.0211	0.3218	0.0211	0.3368	0.0211	0.4356
0.0360	0.5326	0.0255	0.3804	0.0255	0.3206	0.0255	0.3468	0.0255	0.4867
0.0470	0.6301	0.0365	0.4052	0.0365	0.3363	0.0365	0.3684	0.0365	0.6080
0.0580	0.7045	0.0475	0.4282	0.0475	0.3478	0.0475	0.3839	0.0475	0.6956
0.0690	0.7779	0.0585	0.4517	0.0585	0.3480	0.0585	0.3885	0.0585	0.7722
0.0800	0.8123	0.0695	0.4814	0.0695	0.3821	0.0695	0.4087	0.0695	0.8286
0.0910	0.8520	0.0804	0.4985	0.0804	0.3883	0.0804	0.4240	0.0804	0.8742
0.1020	0.8817	0.0914	0.5326	0.0914	0.4058	0.0914	0.4312	0.0914	0.8889
0.1130	0.8965	0.1024	0.5505	0.1024	0.4262	0.1024	0.4405	0.1024	0.9211
0.1349	0.9223	0.1134	0.5892	0.1134	0.4450	0.1134	0.4468	0.1134	0.9247
0.1569	0.9384	0.1354	0.6604	0.1354	0.4778	0.1354	0.4616	0.1354	0.9575
0.1789	0.9621	0.1574	0.7200	0.1574	0.5306	0.1574	0.4630	0.1574	0.9761
0.2009	0.9740	0.1793	0.7838	0.1793	0.5931	0.1793	0.4610	0.1793	0.9877
0.2229	0.9860	0.2013	0.8338	0.2013	0.6373	0.2013	0.4622	0.2013	0.9894
0.2668	0.9897	0.2233	0.8794	0.2233	0.6939	0.2233	0.4638	0.2233	0.9902
0.3108	0.9942	0.2673	0.9329	0.2673	0.7788	0.2673	0.4741	0.2673	0.9919
0.3547	0.9918	0.3112	0.9603	0.3112	0.8401	0.3112	0.5102	0.3112	0.9923
0.3987	0.9963	0.3552	0.9736	0.3552	0.8816	0.3552	0.5570	0.3552	0.9913
0.4426	1.0033	0.3991	0.9820	0.3991	0.9121	0.3991	0.6177	0.3991	1.0003
0.5525	1.0025	0.4431	0.9842	0.4431	0.9233	0.4431	0.6832	0.4431	1.0032
0.6624	1.0059	0.5530	0.9950	0.5530	0.9416	0.5530	0.7696	0.5530	1.0048
0.7723	1.0067	0.6629	0.9980	0.6629	0.9614	0.6629	0.8257	0.6629	1.0101
0.8822	0.9973	0.7727	0.9942	0.7727	0.9732	0.7727	0.8560	0.7727	1.0046
0.9921	0.9972	0.8826	0.9948	0.8826	0.9818	0.8826	0.8863	0.8826	1.0009
		0.9925	0.9960	0.9925	0.9857	0.9925	0.9148	0.9925	1.0001
						1.3222	0.9477		
						1.7618	0.9455		
						2.2013	0.9141		
						2.6409	0.8949		

87-9-19-61

TABLE IVa
TOTAL PRESSURE BOUNDARY LAYER SURVEYS IN AR310 EXIT PLANE (CONCLUDED)

SURVEY 11		SURVEY 12		SURVEY 13	
y_{bl}/H	$(P - p_{ref})/Q_{ref}$	y_{bl}/H	$(P - p_{ref})/Q_{ref}$	y_{bl}/H	$(P - p_{ref})/Q_{ref}$
0.0035	0.1152	0.0035	0.1552	0.0035	0.1724
0.0040	0.1127	0.0040	0.1550	0.0040	0.1875
0.0044	0.1078	0.0044	0.1569	0.0044	0.2010
0.0048	0.1113	0.0048	0.1550	0.0048	0.2141
0.0053	0.1163	0.0053	0.1594	0.0053	0.2262
0.0057	0.1201	0.0057	0.1548	0.0057	0.2341
0.0062	0.1237	0.0062	0.1541	0.0062	0.2394
0.0066	0.1277	0.0066	0.1524	0.0066	0.2506
0.0070	0.1553	0.0070	0.1536	0.0070	0.2510
0.0075	0.1665	0.0075	0.1541	0.0075	0.2612
0.0079	0.1817	0.0079	0.1519	0.0079	0.2594
0.0083	0.1971	0.0123	0.1530	0.0123	0.2833
0.0088	0.2093	0.0167	0.1569	0.0167	0.3019
0.0132	0.2632	0.0211	0.1713	0.0211	0.3230
0.0176	0.3098	0.0255	0.1802	0.0255	0.3245
0.0220	0.3413	0.0365	0.2097	0.0365	0.3304
0.0264	0.3621	0.0475	0.2277	0.0475	0.3517
0.0308	0.3940	0.0585	0.2429	0.0585	0.3565
0.0418	0.4627	0.0694	0.2460	0.0694	0.3779
0.0527	0.5302	0.0804	0.2501	0.0804	0.3973
0.0637	0.6001	0.0914	0.2624	0.0914	0.4052
0.0747	0.6625	0.1024	0.2663	0.1024	0.4279
0.0857	0.7088	0.1134	0.2747	0.1134	0.4431
0.0967	0.7592	0.1244	0.2751	0.1354	0.4850
0.1077	0.7893	0.1464	0.2802	0.1574	0.5500
0.1187	0.8127	0.1684	0.2715	0.1793	0.5914
0.1297	0.8538	0.1903	0.2569	0.2013	0.6512
0.1407	0.8598	0.2123	0.2570	0.2233	0.7078
0.1626	0.8824	0.2343	0.2360	0.2673	0.7914
0.1846	0.9090	0.2782	0.2358	0.3112	0.8513
0.2066	0.9352	0.3222	0.2728	0.3552	0.9016
0.2286	0.9409	0.3662	0.3543	0.3991	0.9209
0.2505	0.9588	0.4101	0.4806	0.4431	0.9357
0.2725	0.9621	0.4541	0.6132	0.5530	0.9514
0.3165	0.9695	0.5640	0.7914	0.6629	0.9644
0.3604	0.9784	0.6738	0.8771	0.7727	0.9747
0.4044	0.9779	0.7837	0.9280	0.8826	0.9823
0.4484	0.9841	0.8936	0.9507	0.9925	0.9819
0.4923	0.9807	1.0035	0.9594	1.3222	0.9894
0.5363	0.9839	1.3771	0.9846	1.7618	0.9913
0.6462	0.9825	1.8167	0.9939	2.2013	0.9980
0.7560	0.9849	2.2563	0.9978	2.6409	0.9934
0.8659	0.9898	2.6958	0.9986	2.9705	0.9914
0.9758	0.9832	2.9156	0.9920		
1.0857	0.9888				
1.1956	0.9933				
1.3055	0.9927				
1.6352	0.9868				

87-9-19-62

TABLE IVb
TOTAL PRESSURE BOUNDARY LAYER SURVEYS IN AR630 EXIT PLANE

SURVEY 1		SURVEY 2		SURVEY 3		SURVEY 4		SURVEY 5	
y_{bl}/H	$(P - P_{ref})/Q_{ref}$	y_{bl}/H	$(P - P_{ref})/Q_{ref}$	y_{bl}/H	$(P - P_{ref})/Q_{ref}$	y_{bl}/H	$(P - P_{ref})/Q_{ref}$	y_{bl}/H	$(P - P_{ref})/Q_{ref}$
0.0073	0.1039	0.0073	0.1905	0.0082	0.2090	0.0073	0.2760	0.0073	0.1970
0.0082	0.1072	0.0078	0.2272	0.0091	0.2160	0.0256	0.3714	0.0078	0.1825
0.0091	0.1216	0.0082	0.2152	0.0101	0.1970	0.0165	0.3237	0.0082	0.2027
0.0101	0.1266	0.0091	0.2138	0.0110	0.2010	0.0348	0.4128	0.0091	0.1908
0.0110	0.1405	0.0101	0.2306	0.0119	0.2130	0.0439	0.4467	0.0110	0.1974
0.0119	0.1400	0.0110	0.2276	0.0165	0.2110	0.0531	0.4763	0.0128	0.2076
0.0128	0.1576	0.0119	0.2174	0.0210	0.2530	0.0622	0.5056	0.0146	0.2218
0.0137	0.1575	0.0128	0.2320	0.0256	0.3130	0.0714	0.5374	0.0165	0.1999
0.0146	0.1695	0.0146	0.2477	0.0233	0.2830	0.0805	0.5599	0.0188	0.2187
0.0165	0.1734	0.0165	0.2335	0.0279	0.3240	0.0897	0.6007	0.0210	0.2304
0.0183	0.1633	0.0183	0.2405	0.0325	0.3570	0.0988	0.6256	0.0233	0.2486
0.0201	0.1770	0.0201	0.2547	0.0371	0.3720	0.1080	0.6492	0.0256	0.2707
0.0247	0.1855	0.0220	0.2535	0.0416	0.3930	0.1171	0.6859	0.0279	0.2585
0.0293	0.1987	0.0238	0.2444	0.0462	0.4090	0.1263	0.7172	0.0302	0.3099
0.0339	0.2059	0.0256	0.2547	0.0554	0.4430	0.1354	0.7434	0.0348	0.3423
0.0384	0.2043	0.0302	0.2592	0.0645	0.4720	0.1446	0.7655	0.0393	0.3676
0.0476	0.2095	0.0348	0.2810	0.0737	0.4940	0.1537	0.7940	0.0439	0.4012
0.0567	0.2322	0.0393	0.2799	0.0828	0.5170	0.1674	0.8151	0.0485	0.4130
0.0659	0.2405	0.0439	0.2766	0.0965	0.5570	0.1812	0.8561	0.0531	0.4229
0.0750	0.2224	0.0531	0.2941	0.1102	0.5940	0.1674	0.8121	0.0622	0.4570
0.0842	0.2602	0.0622	0.3154	0.1240	0.6170	0.1949	0.8754	0.0714	0.4851
0.0933	0.2713	0.0714	0.3250	0.1423	0.6680	0.2086	0.8966	0.0805	0.5125
0.1025	0.2749	0.0805	0.3285	0.1331	0.6370	0.2223	0.9136	0.0897	0.5399
0.1162	0.3133	0.0897	0.3221	0.1514	0.6700	0.2360	0.9239	0.0988	0.5936
0.1391	0.2845	0.0988	0.3155	0.1697	0.7180	0.2498	0.9395	0.1080	0.5866
0.1619	0.3027	0.1217	0.3330	0.1834	0.7460	0.2635	0.9488	0.0988	0.5555
0.1848	0.3146	0.1446	0.3399	0.1972	0.7670	0.2772	0.9585	0.1171	0.6338
0.2077	0.3193	0.1674	0.3394	0.2109	0.7950	0.2909	0.9617	0.1354	0.6600
0.2306	0.3211	0.1903	0.3201	0.2246	0.8190	0.3047	0.9717	0.1537	0.6968
0.2534	0.3172	0.2132	0.3270	0.2383	0.8360	0.3230	0.9781	0.1720	0.7602
0.2763	0.3255	0.2360	0.3336	0.2521	0.8550	0.3413	0.9854	0.1903	0.7897
0.3220	0.3198	0.2589	0.3375	0.2658	0.8700	0.3596	0.9865	0.1720	0.7547
0.3678	0.3162	0.2818	0.3263	0.2795	0.8900	0.3779	0.9920	0.2086	0.8177
0.4135	0.3089	0.3275	0.3271	0.2978	0.9120	0.3962	0.9907	0.2269	0.8631
0.4593	0.3212	0.3733	0.3126	0.3161	0.9110	0.4145	0.9873	0.2452	0.8871
0.5508	0.2929	0.4190	0.3043	0.3344	0.9250	0.4328	0.9932	0.2635	0.9045
0.6423	0.2990	0.4648	0.2942	0.3527	0.9420	0.4511	0.9960	0.2818	0.9466
0.7338	0.3203	0.5563	0.2850	0.3710	0.9490	0.4694	0.9956	0.4511	1.0026
0.8253	0.4007	0.6478	0.3043	0.3984	0.9590	0.4876	0.9937	0.6340	0.9982
0.9167	0.5257	0.7392	0.3702	0.4259	0.9730	0.5105	0.9971	0.8170	0.9966
0.8710	0.4613	0.8307	0.4585	0.4533	0.9770	0.5563	0.9934	1.0000	0.9933
1.0082	0.6735	0.9222	0.6239	0.4899	0.9820	0.6020	0.9986	0.6020	0.9986
0.9625	0.5849	1.1510	0.9093	0.5265	0.9830	0.6478	0.9975	0.6478	0.9975
1.0997	0.8043	1.3797	0.9998	0.5631	0.9820				
1.1912	0.9014	1.6084	0.9878	0.6089	0.9860				
1.2827	0.9615	1.8371	0.9913	0.6546	0.9860				
1.3742	0.9850	2.0659	0.9928	0.7004	0.9840				
1.4657	0.9940	2.2946	0.9910	0.7461	0.9860				
1.5572	0.9797	0.6478	0.2974	0.7919	0.9860				
1.6487	0.9884	0.6706	0.3190	0.8376	0.9840				
1.7402	0.9930	0.6935	0.3193	0.8833	0.9870				
1.8317	0.9986	0.7164	0.3486	0.9291	0.9850				
1.9231	0.9959	0.7392	0.3629	0.9131	0.9850				
		0.7621	0.3960	0.8765	0.9890				
		0.7850	0.4478	0.8856	0.9870				
		0.8079	0.4508	0.8948	0.9850				
		0.8307	0.4842	0.8719	0.9860				
		0.8536	0.5191	0.8490	0.9830				
		0.8765	0.5389	0.8262	0.9850				
		0.8994	0.5758	0.8033	0.9810				
		0.9222	0.6341						
		0.9451	0.6652						
		0.9680	0.7033						
		0.9909	0.7299						
		1.0137	0.7673						
		1.0366	0.7926						
		1.0595	0.8270						
		1.0823	0.8442						
		1.1052	0.9069						
		1.1510	0.9160						
		1.1967	0.9475						
		1.2425	0.9686						
		1.2882	0.9736						
		1.3339	0.9798						
		1.3797	0.9889						
		1.4254	0.9858						
		1.4712	0.9946						
		1.5169	0.9879						
		1.5627	0.9869						

87-9-19-63

TABLE IVb
TOTAL PRESSURE BOUNDARY LAYER SURVEYS IN AR630 EXIT PLANE (CONTINUED)

SURVEY 6

y_{bl}/H	$(P - p_{ref})/Q_{ref}$
0.0073	0.2107
0.0082	0.2190
0.0091	0.2054
0.0101	0.2062
0.0110	0.2184
0.0119	0.2211
0.0128	0.2152
0.0146	0.2126
0.0165	0.2194
0.0183	0.2220
0.0201	0.2417
0.0220	0.2367
0.0238	0.2608
0.0256	0.2773
0.0302	0.3010
0.0348	0.3460
0.0393	0.3534
0.0439	0.4333
0.0485	0.4166
0.0531	0.4332
0.0439	0.3998
0.0576	0.4358
0.0668	0.4771
0.0805	0.5033
0.0988	0.5494
0.1171	0.5900
0.1354	0.6448
0.1537	0.6510
0.1720	0.6928
0.1903	0.7475
0.2086	0.7668
0.2269	0.7993
0.2452	0.8244
0.2635	0.8560
0.2818	0.8796
0.3001	0.8906
0.3184	0.9064
0.3367	0.9261
0.3550	0.9359
0.3733	0.9497
0.3916	0.9670
0.4511	0.9909
0.6340	0.9992
0.8170	0.9997
1.0000	0.9973

SURVEY 7

y_{bl}/H	$(P - p_{ref})/Q_{ref}$
0.0073	0.1618
0.0082	0.1723
0.0091	0.1799
0.0101	0.1886
0.0110	0.1858
0.0128	0.1927
0.0101	0.1639
0.0137	0.1964
0.0174	0.2262
0.0210	0.2554
0.0247	0.2725
0.0284	0.2874
0.0320	0.3042
0.0357	0.3215
0.0393	0.3353
0.0439	0.3498
0.0485	0.3648
0.0531	0.3887
0.0622	0.4330
0.0714	0.4653
0.0805	0.5080
0.0897	0.5468
0.0988	0.5732
0.1080	0.6169
0.1171	0.6394
0.1263	0.6691
0.1354	0.6936
0.1583	0.7631
0.1812	0.8187
0.2040	0.8607
0.2269	0.8966
0.2498	0.9186
0.2726	0.9411
0.2955	0.9533
0.3184	0.9714
0.3413	0.9738
0.3641	0.9788
0.3870	0.9862
0.4099	0.9846
0.4126	0.9851
0.4401	0.9874
0.4675	0.9904
0.4922	0.9896
0.5242	0.9916
0.5563	0.9959
0.5883	0.9909
0.6203	0.9946
0.6569	0.9879
0.6935	0.9906

SURVEY 8

y_{bl}/H	$(P - p_{ref})/Q_{ref}$
0.0073	0.1778
0.0256	0.2291
0.0439	0.3583
0.0348	0.3279
0.0302	0.3004
0.0485	0.3751
0.0576	0.4186
0.0531	0.3982
0.0622	0.4341
0.0714	0.4673
0.0805	0.5154
0.0759	0.4874
0.0851	0.5349
0.0897	0.5492
0.0942	0.5624
0.0988	0.5840
0.1080	0.6124
0.1171	0.6428
0.1263	0.6747
0.1354	0.7022
0.1446	0.7298
0.1537	0.7559
0.1629	0.7819
0.1720	0.8056
0.1812	0.8249
0.1903	0.8323
0.2040	0.8634
0.2177	0.8926
0.2315	0.9045
0.2452	0.9217
0.2635	0.9390
0.2818	0.9540
0.3001	0.9573
0.3367	0.9806
0.3733	0.9788
0.4099	0.9943
0.4465	0.9888
0.4831	0.9953
0.5197	0.9933
0.5563	0.9971
0.5929	0.9938
0.4099	0.9912
0.3916	0.9906
0.3733	0.9855
0.3550	0.9877
0.3367	0.9737
0.3184	0.9729
0.3001	0.9640
0.0348	0.3158
0.0325	0.3010
0.0302	0.3066
0.0279	0.2838
0.0256	0.2768
0.0233	0.2665
0.0210	0.2513
0.0188	0.2302
0.0165	0.2146
0.0142	0.1931
0.0119	0.1899
0.0096	0.1670

SURVEY 9

y_{bl}/H	$(P - p_{ref})/Q_{ref}$
0.0073	0.2149
0.0082	0.2343
0.0091	0.2424
0.0110	0.2516
0.0128	0.2634
0.0146	0.2763
0.0165	0.2835
0.0393	0.3836
0.0165	0.2787
0.0393	0.3885
0.0416	0.3954
0.0439	0.3975
0.0485	0.4208
0.0531	0.4318
0.0576	0.4453
0.0622	0.4695
0.0714	0.5048
0.0805	0.5317
0.0897	0.5681
0.0988	0.5866
0.1125	0.6310
0.1263	0.6670
0.1400	0.7104
0.1537	0.7383
0.1720	0.7749
0.1903	0.8110
0.2086	0.8431
0.2269	0.8688
0.2543	0.9012
0.2818	0.9315
0.3092	0.9457
0.3367	0.9644
0.3641	0.9754
0.3916	0.9850
0.4190	0.9864
0.4465	0.9912
0.4739	0.9898
0.5014	0.9890
0.5288	0.9952
0.5563	0.9944
0.5929	0.9918
0.6295	0.9898
0.6661	0.9940
0.7027	0.9906
0.7392	0.9894

SURVEY 10

y_{bl}/H	$(P - p_{ref})/Q_{ref}$
0.0073	0.2780
0.0078	0.2770
0.0087	0.2820
0.0101	0.2890
0.0114	0.2940
0.0128	0.3000
0.0142	0.3190
0.0156	0.3160
0.0174	0.3320
0.0192	0.3310
0.0215	0.3450
0.0238	0.3500
0.0284	0.3690
0.0329	0.3900
0.0375	0.3990
0.0421	0.4170
0.0467	0.4310
0.0512	0.4410
0.0604	0.4800
0.0695	0.5090
0.0787	0.5400
0.0878	0.5570
0.1016	0.5880
0.1153	0.6230
0.1290	0.6450
0.1491	0.6690
0.1629	0.7080
0.1812	0.7410
0.1995	0.7660
0.2177	0.8020
0.2360	0.8200
0.2543	0.8490
0.2726	0.8690
0.2955	0.8880
0.3184	0.9050
0.3413	0.9320
0.3641	0.9420
0.3916	0.9500
0.4190	0.9620
0.4465	0.9670
0.4922	0.9760
0.5380	0.9780
0.5837	0.9820
0.6295	0.9840
0.6752	0.9820
0.7667	0.9800
0.8582	0.9840
0.9497	0.9820
0.5380	0.9830
0.5563	0.9820
0.5746	0.9840
0.5929	0.9830
0.6112	0.9830
0.6295	0.9820
0.6661	0.9810
0.7027	0.9820
0.7392	0.9830

APPENDIX A

AR310 TRANSITION DUCT INSPECTION

Due to an obvious difference between the actual exit plane shape and the design shape Eq. (1-1), a detailed inspection of the AR310 duct was performed. The cross-sectional shape at 15 axial locations was defined with a Cordax 1000, 3-axis coordinate measuring machine (0.00025 cm resolution). Initial measurements indicated that the duct was very symmetrical and that upstream of $x/R = 0.88$ the duct coordinates were in close agreement with Eq. (1-1). Thus, to define the duct shape, only one quadrant of the duct is presented from $x/R = 0.88$ to $x/R = 2.00$. The results at 8 axial stations are shown in Fig. A-1 and an entire set of inspection data is listed in Table A-I. In Fig. A-1, the design shape is the solid line and the actual shape is the dashed line. At $x/R = 0.88$ the agreement between the design and actual cross-sectional shape is very good but it degrades rapidly further downstream. At the exit plane ($x/R = 2.00$) the actual duct has a more square corner and the span is 7 percent of the half-height (H) smaller than the design.

In summary, the AR310 transition duct shows significant cross-sectional shape variation from the design. In order to accurately describe the duct, Eq. (1-1) should be used for $x/R < 1.0$ and Table A-1 for $x/R > 1.0$.

PRECEDING PAGE BLANK NOT FILMED

TABLE A.I.
MEASURED CROSS SECTIONS OF AR310 TRANSITION DUCT (CONT.)

x/R = 1.28

y	z
0.0000	-7.0152
0.6215	-7.0096
1.4750	-7.0038
2.0851	-6.9972
2.5456	-6.9916
3.1892	-6.9827
3.4737	-6.9771
3.9357	-6.9670
4.2679	-6.9599
4.8877	-6.9403
5.4389	-6.9167
5.8999	-6.8931
6.4229	-6.8600
6.7071	-6.8405
7.3426	-6.7869
7.7069	-6.7508
8.0272	-6.7160
8.3434	-6.6779
8.7307	-6.6258
9.1801	-6.5570
9.6505	-6.4750
10.1788	-6.3691
10.8011	-6.2217
11.2199	-6.1064
11.6096	-5.9865
11.9825	-5.8575
12.2860	-5.7391
12.6416	-5.5837
13.0637	-5.3706
13.3749	-5.1890
13.6901	-4.9771
14.0523	-4.6901
14.3853	-4.3683
14.6421	-4.0637
14.8135	-3.8189
15.0449	-3.4072
15.2278	-2.9594
15.3429	-2.5423
15.4203	-2.1171
15.4653	-1.7333
15.4932	-1.3653
15.5141	-0.9164
15.5258	-0.5977
15.5410	-0.1750
15.5466	0.0000

x/R = 1.36

y	z
0.0003	-6.7424
0.6678	-6.7374
1.4686	-6.7330
2.2576	-6.7272
3.0592	-6.7208
3.5844	-6.7160
4.6401	-6.7010
5.2563	-6.6878
5.7638	-6.6726
6.2169	-6.6576
6.6307	-6.6393
7.0272	-6.6203
7.6446	-6.5827
8.3464	-6.5293
8.8334	-6.4844
9.0355	-6.4630
9.3904	-6.4224
9.8080	-6.3678
10.2481	-6.3020
10.6934	-6.2263
11.0109	-6.1648
11.4366	-6.0719
11.5849	-6.0373
11.9621	-5.9390
12.3751	-5.8166
12.7251	-5.6967
13.1260	-5.5385
13.3190	-5.4521
13.6716	-5.2733
14.1016	-5.0104
14.2461	-4.9083
14.4252	-4.7699
14.6345	-4.5872
14.8839	-4.3266
15.1371	-3.9903
15.2423	-3.8224
15.4183	-3.4775
15.5204	-3.2164
15.6246	-2.8491
15.6873	-2.5319
15.7566	-1.9477
15.7833	-1.5131
15.7993	-1.0792
15.8079	-0.7234
15.8158	-0.3970
15.8272	0.0000

x/R = 1.44

y	z
0.0000	-6.5062
0.7206	-6.4996
1.7099	-6.4943
2.4638	-6.4915
3.3480	-6.4859
4.2299	-6.4823
4.8796	-6.4757
5.6370	-6.4653
6.3795	-6.4516
6.8773	-6.4397
7.5019	-6.4432
8.3528	-6.3797
8.9926	-6.3419
9.7198	-6.2850
10.3348	-6.2233
10.8702	-6.1575
11.4518	-6.0711
11.8941	-5.9906
12.2123	-5.9246
12.6776	-5.8123
13.1432	-5.6777
13.5913	-5.5182
14.0035	-5.3368
14.3637	-5.1432
14.6035	-4.9911
14.8118	-4.8400
15.1399	-4.5484
15.4729	-4.1237
15.6449	-3.8197
15.7846	-3.4862
15.8905	-3.1161
15.9479	-2.8146
15.9969	-2.4023
16.0302	-1.8771
16.0467	-1.3180
16.0525	-0.9949
16.0597	-0.4722
16.0589	-0.4905
16.0696	0.0000

x/R = 1.52

y	z
0.0000	-6.2992
0.3825	-6.2959
1.2515	-6.2906
2.1689	-6.2868
3.0676	-6.2842
3.9919	-6.2812
4.6606	-6.2789
5.3424	-6.2753
5.9370	-6.2713
6.7752	-6.2626
7.4328	-6.2520
7.9906	-6.2403
8.5659	-6.2243
9.1803	-6.2022
9.8478	-6.1704
10.3528	-6.1397
10.8641	-6.1008
11.3584	-6.0551
11.8928	-5.9931
12.2065	-5.9487
12.7020	-5.8666
13.1803	-5.7701
13.6853	-5.6411
14.0223	-5.5331
14.2646	-5.4409
14.5476	-5.3152
14.8189	-5.1717
15.0995	-4.9949
15.3772	-4.7798
15.5334	-4.6284
15.6779	-4.4547
15.8669	-4.1565
16.0195	-3.8176
16.1315	-3.4356
16.1803	-3.1661
16.2126	-2.8986
16.2418	-2.5314
16.2573	-2.1575
16.2624	-1.8786
16.2654	-1.5728
16.2682	-1.1930
16.2705	-0.8026
16.2728	-0.3396
16.2768	-0.0947
16.2778	0.0000

x/R = 1.60

y	z
0.0000	-6.1295
0.8999	-6.1237
1.9677	-6.1191
2.8237	-6.1166
3.9324	-6.1151
4.7572	-6.1133
5.5796	-6.1107
6.3696	-6.1079
6.9583	-6.1054
7.6096	-6.1006
8.2725	-6.0932
8.9604	-6.0830
9.6853	-6.0673
10.4430	-6.0439
10.9228	-6.0234
11.4546	-5.9936
12.0134	-5.9538
12.5341	-5.9058
13.1486	-5.8336
13.6286	-5.7592
14.0957	-5.6614
14.5517	-5.5288
14.9489	-5.3706
15.2799	-5.1986
15.4935	-5.0637
15.6517	-4.9482
15.8011	-4.8204
15.9916	-4.5997
16.0685	-4.4803
16.1884	-4.2375
16.3195	-3.8141
16.4018	-3.2870
16.4414	-2.6596
16.4501	-2.2205
16.4488	-1.7813
16.4462	-1.4696
16.4445	-0.8329
16.4445	-0.2794
16.4508	0.1394
16.4478	0.0000

TABLE A.I.
MEASURED CROSS SECTIONS OF AR310 TRANSITION DUCT

x/R = 0.88		x/R = 0.96		x/R = 1.04		x/R = 1.12		x/R = 1.20	
y	z	y	z	y	z	y	z	y	z
0.0000	-8.9225	0.0000	-8.5049	0.0000	-8.0863	0.0000	-7.6878	0.0000	-7.3282
0.2278	-8.9202	0.1308	-8.5042	0.6165	-8.0795	0.6055	-7.6822	0.9144	-7.3203
0.6894	-8.9103	0.5799	-8.4976	0.9180	-8.0749	1.0528	-7.6764	1.6828	-7.3116
1.1768	-8.8933	1.2035	-8.4821	1.6093	-8.0589	1.7056	-7.6655	2.6726	-7.2936
1.7620	-8.8626	1.9944	-8.4483	2.4953	-8.0231	2.4615	-7.6449	3.3942	-7.2748
2.2857	-8.8235	2.8209	-8.3922	3.1605	-7.9847	3.3050	-7.6116	4.1062	-7.2484
2.7534	-8.7795	3.5123	-8.3284	3.8308	-7.9345	4.0188	-7.5720	4.7864	-7.2149
3.2189	-8.7269	3.9553	-8.2758	4.2466	-7.8941	4.6982	-7.5220	5.4933	-7.1679
3.6373	-8.6690	4.3914	-8.2166	5.0089	-7.8049	5.4318	-7.4521	6.1359	-7.1143
4.0013	-8.6121	4.8379	-8.1465	5.6845	-7.7074	6.2593	-7.3503	6.7125	-7.0554
4.3279	-8.5552	5.4046	-8.0449	6.4262	-7.5748	6.8169	-7.2677	7.3675	-6.9748
4.5926	-8.5052	5.7920	-7.9662	7.1217	-7.4265	7.5202	-7.1435	7.9449	-6.8903
5.1255	-8.3924	6.3297	-7.8423	7.5281	-7.3282	8.0841	-7.0264	8.6233	-6.7716
5.6754	-8.2593	6.6708	-7.7551	8.0142	-7.1971	8.5659	-6.9126	9.2662	-6.6378
6.0787	-8.1493	6.9898	-7.6675	8.5583	-7.0325	9.0785	-6.7762	9.7846	-6.5126
6.4793	-8.0294	7.5433	-7.5433	9.0630	-6.8605	9.4722	-6.6591	10.1359	-6.4176
6.8882	-7.8948	7.8483	-7.3975	9.4818	-6.7018	9.9868	-6.4892	10.4780	-6.3165
7.2840	-7.7528	8.3287	-7.2217	9.8862	-6.5329	10.3599	-6.3508	10.8504	-6.1951
7.6871	-7.5949	8.7445	-7.0546	10.4031	-6.2908	10.7747	-6.1806	11.1694	-6.0813
8.0744	-7.4300	9.1305	-6.8842	10.9212	-6.0155	11.1730	-5.9995	11.5484	-5.9309
8.2949	-7.3299	9.4348	-6.7399	11.2700	-5.8077	11.6096	-5.7755	11.7889	-5.8263
8.5507	-7.2075	9.6992	-6.6060	11.6528	-5.5542	11.9537	-5.5781	12.1173	-5.6706
8.8964	-7.0310	9.9751	-6.4574	11.9990	-5.2979	12.2895	-5.3624	12.3962	-5.5245
9.1509	-6.8918	10.2906	-6.2746	12.1742	-5.1559	12.6190	-5.1265	12.6583	-5.3734
9.5270	-6.6718	10.5639	-6.1051	12.4363	-4.9268	12.8839	-4.9134	12.9685	-5.1753
9.7874	-6.5082	10.8488	-5.9141	12.7196	-4.6505	13.1519	-4.6711	13.2870	-4.9436
10.2227	-6.2103	11.0152	-5.7958	12.9723	-4.3734	13.3640	-4.4582	13.5976	-4.6835
10.6502	-5.8839	11.3043	-5.5766	13.0980	-4.2217	13.5471	-4.2542	13.7610	-4.5301
10.9690	-5.6131	11.4750	-5.4379	13.2690	-4.0015	13.7013	-4.0655	13.9830	-4.2969
11.1984	-5.4026	11.7414	-5.2045	13.4526	-3.7394	13.8839	-3.8186	14.1788	-4.0630
11.3965	-5.2075	11.9416	-5.0160	13.6591	-3.4000	14.0805	-3.5116	14.3706	-3.8006
11.5352	-5.0635	12.1361	-4.8184	13.8359	-3.0546	14.2281	-3.2421	14.5918	-3.4374
11.6967	-4.8870	12.2751	-4.6680	13.9484	-2.7953	14.3716	-2.9332	14.7688	-3.0721
11.9210	-4.6205	12.5588	-4.3330	14.0566	-2.5019	14.5252	-2.5105	14.9382	-2.5954
12.0968	-4.3952	12.8346	-3.9611	14.2103	-1.9535	14.6121	-2.1933	15.0266	-2.2398
12.3355	-4.0612	13.1186	-3.5149	14.2479	-1.7757	14.6985	-1.7744	15.0901	-1.8893
12.5062	-3.7970	13.3248	-3.1267	14.2855	-1.5629	14.7460	-1.4359	15.1501	-1.3599
12.6840	-3.4907	13.4579	-2.8291	14.3294	-1.2311	14.7861	-0.9893	15.1765	-0.9507
12.7805	-3.3081	13.5989	-2.4521	14.3535	-0.9804	14.8062	-0.6474	15.1994	-0.4666
12.8925	-3.0759	13.7114	-2.0785	14.3703	-0.7501	14.8222	-0.3424	15.2187	0.0000
13.0302	-2.7518	13.7879	-1.7501	14.4008	-0.2781	14.8402	0.0000		
13.1656	-2.3708	13.8206	-1.5776	14.4201	-0.0627				
13.2504	-2.0815	13.8781	-1.1869	14.4170	-0.0003				
13.3436	-1.6850	13.9144	-0.8336						
13.4033	-1.3386	13.9451	-0.4415						
13.4602	-0.8799	13.9591	-0.2319						
13.4940	-0.4872	13.9736	0.0000						
13.5164	-0.1737								
13.5247	0.0000								

DIMENSIONS IN cm

87-9-19-70

TABLE A.I.
MEASURED CROSS SECTIONS OF AR310 TRANSITION DUCT (CONCLUDED)

x/R = 1.68		x/R = 1.76		x/R = 1.84		x/R = 1.92		x/R = 2.00	
y	z	y	z	y	z	y	z	y	z
0.0000	-5.9936	0.0000	-5.8936	0.0000	-5.8273	0.0000	-5.7884	0.0000	-5.7760
0.9710	-5.9888	1.1003	-5.8885	0.6388	-5.8242	0.9947	-5.7859	0.5494	-5.7760
2.1847	-5.9853	1.8207	-5.8872	1.6982	-5.8227	1.9715	-5.7856	1.3175	-5.7762
3.1656	-5.9840	2.7874	-5.8852	2.8037	-5.8209	2.9167	-5.7849	2.1951	-5.7760
4.0183	-5.9830	3.6670	-5.8847	3.7889	-5.8194	3.9652	-5.7833	3.1681	-5.7760
4.7394	-5.9802	4.4409	-5.8829	5.1829	-5.8184	5.0091	-5.7821	4.2753	-5.7760
5.6385	-5.9784	5.1587	-5.8816	6.3701	-5.8174	5.8837	-5.7805	5.2972	-5.7760
6.6921	-5.9764	5.8715	-5.8809	7.2903	-5.8148	6.7059	-5.7795	6.0434	-5.7752
7.7203	-5.9741	6.6558	-5.8798	8.2603	-5.8133	7.8199	-5.7772	6.7986	-5.7752
8.7114	-5.9690	7.2517	-5.8786	9.0279	-5.8136	9.1443	-5.7770	7.4384	-5.7752
9.6733	-5.9619	7.8897	-5.8781	9.8003	-5.8123	10.5207	-5.7762	8.3533	-5.7757
10.3254	-5.9540	8.6114	-5.8773	10.6832	-5.8130	11.7272	-5.7770	9.0150	-5.7749
11.0599	-5.9406	9.3711	-5.8748	11.7079	-5.8120	12.4356	-5.7793	9.7439	-5.7757
11.8321	-5.9164	10.0239	-5.8727	12.5194	-5.8105	12.9291	-5.7780	10.6007	-5.7752
12.3944	-5.8920	10.4795	-5.8720	13.0741	-5.8075	13.3942	-5.7780	11.3911	-5.7749
12.8537	-5.8679	11.1514	-5.8689	13.5275	-5.8052	14.0244	-5.7765	12.0945	-5.7749
13.2542	-5.8423	11.6197	-5.8638	14.1813	-5.7960	14.5354	-5.7762	12.7160	-5.7752
13.6873	-5.8057	12.0985	-5.8567	14.6710	-5.7772	14.7759	-5.7744	13.5458	-5.7747
14.1074	-5.7556	12.6215	-5.8468	14.8689	-5.7661	14.9936	-5.7719	14.3378	-5.7749
14.6502	-5.6548	13.0871	-5.8374	15.1869	-5.7399	15.3774	-5.7668	14.8521	-5.7747
15.1427	-5.5075	13.5585	-5.8245	15.5390	-5.6967	15.6614	-5.7577	15.3726	-5.7752
15.4955	-5.3589	13.8234	-5.8138	15.7615	-5.6589	15.8913	-5.7445	15.8885	-5.7744
15.8069	-5.1859	14.1689	-5.7942	15.8808	-5.6347	16.2420	-5.7180	16.2032	-5.7691
15.9990	-5.0518	14.3914	-5.7762	16.0856	-5.5875	16.4937	-5.7008	16.5169	-5.7655
16.1041	-4.9619	14.6703	-5.7455	16.2936	-5.5309	16.6456	-5.6934	16.7762	-5.6794
16.3256	-4.6586	14.9964	-5.6942	16.4069	-5.4978	16.6842	5.6766	16.7792	-5.6627
16.4498	-4.3292	15.3388	-5.6180	16.4917	-5.4785	16.7289	-5.6258	16.7838	-5.5944
16.5296	-3.8804	15.5796	-5.5479	16.6558	-5.1846	16.7480	-5.5039	16.7945	-5.2659
16.5707	-3.3348	15.9288	-5.4140	16.7132	-4.8633	16.7587	-5.3820	16.7912	-4.7447
16.5847	-2.9301	16.2070	-5.2723	16.7434	-4.4491	16.7683	-5.1765	16.7912	-4.1671
16.5898	-2.6573	16.3774	-5.1338	16.7485	-4.1011	16.7764	-4.8933	16.7919	-3.6464
16.5923	-2.2913	16.5037	-4.9263	16.7488	-3.7887	16.7810	-4.5750	16.7914	-2.9835
16.5882	-1.7930	16.5809	-4.7181	16.7495	-3.2700	16.7805	-4.2827	16.7912	-2.2870
16.5844	-1.4526	16.6233	-4.5194	16.7498	-2.9263	16.7782	-3.8382	16.7914	-1.7046
16.5816	-0.9802	16.6632	-4.1313	16.7472	-2.3828	16.7772	-3.5425	16.7919	-1.1438
16.5799	-0.6462	16.6779	-3.7625	16.7437	-1.9921	16.7764	-3.1532	16.7914	-0.6187
16.5796	-0.2454	16.6832	-3.4313	16.7409	-1.6759	16.7757	-2.7529	16.7912	-0.2830
16.5814	0.0000	16.6893	-2.9014	16.7383	-1.2055	16.7734	-2.3818	16.7912	-0.0597
		16.6896	-2.3467	16.7378	-0.7953	16.7709	-1.9964	16.7912	0.0000
		16.6840	-1.8164	16.7378	-0.3399	16.7693	-1.7137		
		16.6799	-1.4544	16.7373	-0.0201	16.7683	-1.3076		
		16.6774	-0.9787	16.7376	0.0000	16.7673	-1.0691		
		16.6766	-0.6340			16.7678	-0.5029		
		16.6766	-0.4168			16.7678	0.0000		
		16.6769	0.0000						

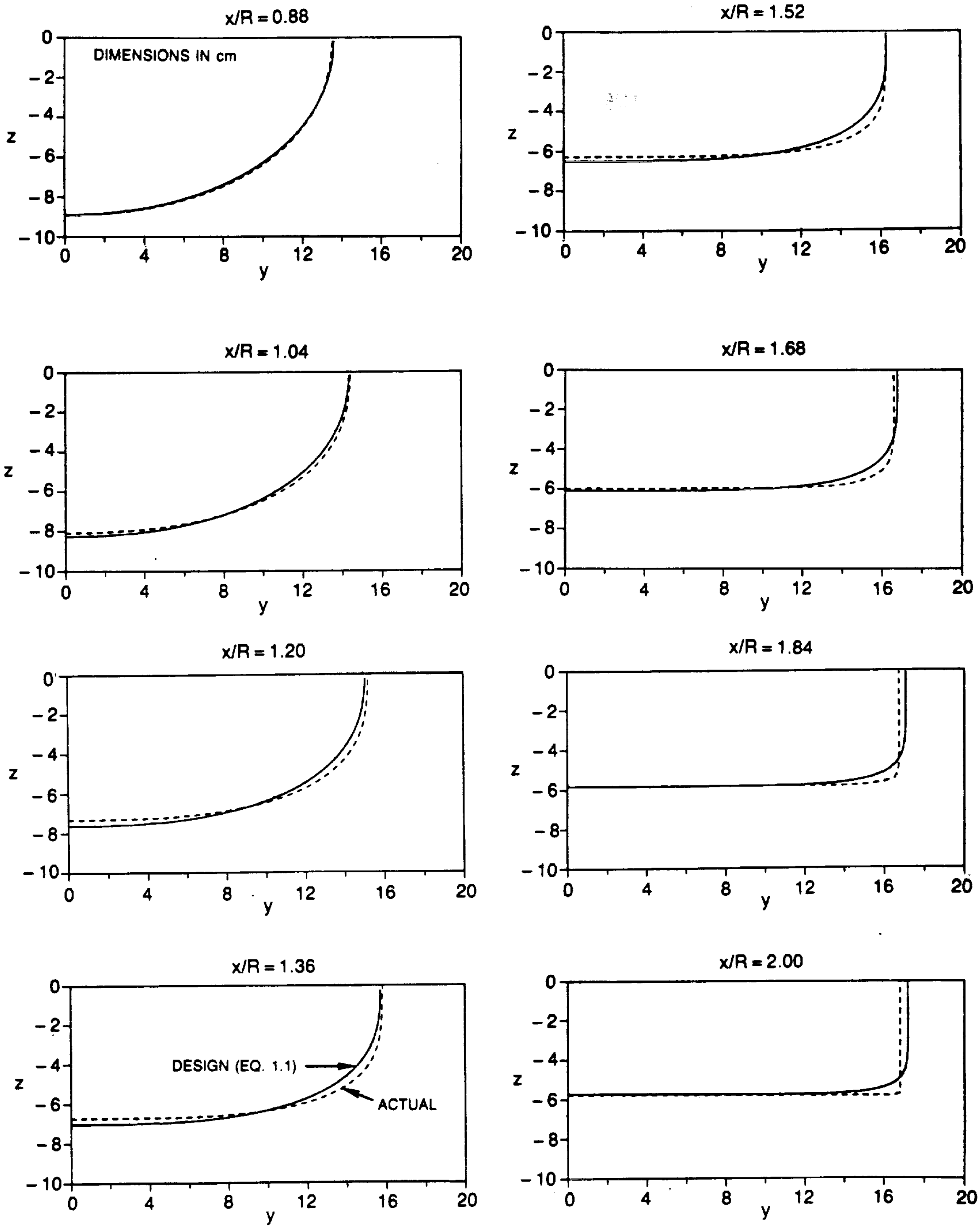

Figure A.1. — Comparison of AR310 Design Cross Section to Actual Cross Section

APPENDIX B

ERROR ANALYSIS

B.1 LV Measurements

A detailed error analysis was performed for the LV measurements using the method described by Patrick (Ref. 22). This uncertainty analysis includes the consideration of fixed (bias) and precision (random) errors and the methods for calculating the propagation of measurement errors through the system. Errors in the LV measurement system have been categorized as: (1) data processing errors, (2) laser beam geometrical errors, (3) processor errors, and (4) errors associated with seeding. Data processing errors arise from averaging a finite number of data samples per data point. Processor errors are the clock synchronization error, the quantizing error, the threshold limit error, the pedestal removal filter error, and the electronic noise induced errors. Laser beam geometrical errors include positioning uncertainty of the probe volume, angular sensitivity of the probe volume, fringe spacing uncertainty, and beam orientation errors, as well as limitations imposed by a finite-sized probe volume. Seeding errors include flow distortion caused by seed injection, errors associated with the arrival rate of seed passing through the probe volume (individual realization bias), and particle lag errors in accelerating (or decelerating) flowfields.

Table B-1 presents an itemized list of the estimated uncertainties for the mean velocity components and RMS fluctuating components. The values listed for the mean components are relative to the inlet reference velocity, U_{ref}. The values for the RMS fluctuating components are relative to 0.20 U_{ref} which approximates the maximum measured turbulence kinetic energy value.

The three categories of bias errors (processor, beam geometry, and seeding) are listed in the upper portion of the table in boxed areas with the appropriate errors itemized in each box. The root of the squared sum (since the errors are generally independent) of each itemized list is given below each box. Below the total seeding bias is the total bias (root of the squared sum of the total processor, beam geometry, and seeding bias errors). Below this is the precision error. The total bias and precision errors are combined to give the total uncertainty in the LV measurements by

$$\text{Total Uncertainty} = \text{Total Bias} + 2 \times \text{Precision Error}$$

As shown at the bottom of the table, the uncertainty in the axial mean component is about two percent of U_{ref} and the uncertainty in the mean cross-flow components is about one percent. For the RMS fluctuating components, the uncertainty ranges from two to four percent of 0.20 U_{ref} with the axial component being the most uncertain. All these errors represent worst case situations and thus, in general, most measurements are of better accuracy.

Many of the errors listed as zero in the table are inappropriate (and thus don't exist) because of the type of processor (item 5 of processsor bias), optical setup (item 6 of processor bias and item 7 of beam geometry bias), processor settings (item 2 and 7 of processor bias), Bragg shifting (item 5 and 6 of beam geometry bias), or the seeding technique (item 1 of seeding bias). Item 1 of processor bias, particle acceleration bias, is assumed to be zero since there are no large accelerations expected in a constant area, subsonic duct flow. Item 1 of beam geometry bias, finite probe volume bias, is zero since the measured velocity profiles showed no shaped peaked profiles. Item 2 of seeding bias, particle lag bias, is assumed zero for the turbulence measurements, since small seeding particles were used. However, this type of error may contaminate the data but it is extremely difficult to estimate (Ref. 22). Also note that items 3 and 4 of seeding bias are assumed to offset each other and thus are not independent errors (see Ref. 22).

B.2 Total Pressure Measurements

The accuracy of the total pressure measurements is dependent on several factors including the accuracy of the pressure transducers, the angular sensitivity of the pitot probes, and the effect of turbulence on the pitot reading. Each of these factors will be discussed below.

Pressure transducers were calibrated to an accuracy of ±0.04 Q_{ref} at the beginning of each test day. Transducer output voltages were zeroed prior to each traverse to compensate for thermal drift. Zeroes were also checked after each traverse to ensure that drift during the traverse did not exceed ±0.002 Q_{ref}, otherwise the data was retaken.

Two types of pitot probes were used in this study: an aspirated kielhead for the overall total pressure distribution at the duct inlet and exit planes and a flattened hypodermic impact tube for boundary layer surveys at the inlet and exit planes. Patrick (Ref. 26) has calibrated the angular sensitivity of these types of probes over a range of dynamic head. For the aspirated kielhead, the accuracy was found to be within 1% Q over a range of ±30 deg angle of incidence. The boundary layer probes were accurate within 1% over ± 7 deg angle of incidence. The maximum flow angle relative to the axial direction (the direction in which pitot probes were oriented) was measured (from LV data) to be 10 deg in the corners of the AR310 duct and 8.5 deg along the semi-major axis between the vortex pair in the AR630 duct. For the kielhead probe these flow angles are well within the 1% Q angular sensitivity range. For the boundary layer probe, these flow angles are outside the 1% Q angular sensitivity range and could cause errors in boundary layer surveys 12 for the AR310 duct and 1 and 2 for the AR630 duct to be as large as 2% Q.

The effect of turbulence on pitot measurements is generally separated into two parts. First, pitot probes respond to static pressure plus the square of the velocity. Thus, Reynolds decomposition and time averaging yields

$$\left(\frac{P - P_{ref}}{Q_{ref}}\right)_{measured} = \frac{P - P_{ref}}{Q_{ref}} \frac{U_{TOT}^2}{U_{ref}^2} + \frac{q}{U_{ref}^2} \qquad \text{(B-1)}$$

Where $q = (\overline{u^2} + \overline{v^2} + \overline{w^2})/2$. Thus, the normalized total pressure will sense a pressure which is high by an amount equal to the measured normalized turbulent kinetic energy. As shown in Figs. 4-14 and 4-28 (also see Table III) the highest turbulence levels occur in the corners of the AR310 duct (maximum $q = 0.018\ U_{ref}^2$) and along the semi-major axis between the vortex pair for the AR630 duct (maximum $q = 0.009\ U_{ref}^2$). Therefore, the suspect data are the same boundary layers that are suspect due to probe angular sensitivity. Also, the kielhead probe measurements are suspect in these regions, reading high by possible 2 to 4 percent of U_{ref}^2.

The second effect of turbulence depends on the scale of turbulence. The instantaneous velocity fluctuations result in instantaneous angle of incidence fluctuations, thus a time average pitot measurement will be low if the angle fluctuations exceed the acceptance angle of the probe. To approximate the value of the error, integral length scale information of the turbulence is necessary. Since this data does not exist for the current experiment, the error cannot be estimated. Note that this error counteracts the turbulence kinetic energy error.

In summary, the accuracy of the total pressure measurements varied throughout the flowfield. Except in the AR310 corner and along the semi-major axis between the vortex pair for the AR630 duct, the kielhead and boundary layer probe measurement accuracy is reasonably estimated to be between 1-2% of Q_{ref}. For the measurements in the high turbulence, high cross-flow regions the accuracy cannot be estimated.

TABLE B-I
ESTIMATED BIAS ERRORS, PRECISION ERRORS, AND UNCERTAINTIES OF LV MEASUREMENTS

PROCESSOR BIAS ERRORS	U	V	W	$\sqrt{\overline{u^2}}$	$\sqrt{\overline{v^2}}$	$\sqrt{\overline{w^2}}$
1. PARTICLE ACCELERATION BIAS (PAB)	0	0	0	0	0	0
2. COMPARATOR TOLERANCE BIAS (CTB)	0	0	0	0	0	0
3. CLOCK SYNCHRONIZATION ERROR (CSB)	+0.0004 −0	0.01%	0.01%	+0.0003 −0	+0.002 −0	+0.002 −0
4. QUANTIZING ERROR (QB)	0.01%	0.01%	0.01%	0.01%	0.01%	0.01%
5. THRESHOLD LIMIT ERROR (TLB)	0	0	0	0	0	0
6. ELECTRONIC NOISE INDUCED ERROR (ENB)	0	0	0	0	0	0
7. PEDESTAL FILTER REMOVAL ERROR (PFB)	0	0	0	0	0	0
PROCESSOR BIAS (PB)	+0.0004 −0	0.01%	0.01%	+0.0003 −0	+0.0002 −0	+0.0002 −0
BEAM GEOMETRY BIAS ERRORS						
1. FINITE PROBE VOLUME BIAS (PVB)	0	0	0	0	0	0
2. BEAM LOCATION BIAS (BLB)	±0.0142	±0.0035	±0.0028	±0.0166	±0.0074	±0.0062
3. BEAM ORIENTATION BIAS (BOB)	±0.0012	±0.0049	±0.0052	±0.0081	±0.0065	±0.0076
4. FRINGE SPACING UNCERTAINTY (FSB)	±0.0041	±0.0005	±0.0005	±0.0030	±0.0022	±0.0018
5. NEGATIVE VELOCITY BIAS (NVB)	0	0	0	0	0	0
6. INCOMPLETE SIGNAL BIAS (ISB)	0	0	0	0	0	0
7. FREQUENCY BROADENING BIAS (FBB)	0	0	0	0	0	0
BEAM GEOMETRY BIAS (BGB)	±0.00148	±0.0060	±0.0059	±0.0187	±0.0101	±0.0100
SEEDING BIAS ERRORS						
1. FLOW DISTORTION BIAS (FDB)	0	0	0	0	0	0
2. PARTICLE LAG BIAS (PLB)	0	±0.0009	±0.0009	0	0	0
3. INDIVIDUAL REALIZATION BIAS (IRB)	+0.004 −0	+0.004 −0	+0.004 −0	+0 −0.005	+0 −0.003	+0 −0.002
4. BRAGG BIAS (BB)	+0 −0.004	+0 −0.004	+0 −0.004	0	0	0
SEEDING BIAS (SB)	0	±0.0009	±0.0009	+0 −0.005	+0 −0.003	+0 −0.002
TOTAL BIAS	±0.0148	±0.0061	±0.0060	+0.0187 −0.0194	+0.0101 −0.0105	+0.0100 −0.0102
PRECISION ERROR	±0.0033	±0.0024	±0.0019	±0.0115	±0.0084	±0.0068
TOTAL UNCERTAINTY	±0.021	±0.011	±0.010	±0.042	±0.027	±0.024

87-9-19-68